THE SURFACE PRESSURE RESPONSE OF A NACA 0015 AIRFOIL IMMERSED IN GRID TURBULENCE

Final report to NASA Langley under grant NAG 1-1942

Volume 1: Characteristics of the turbulence.

Semere Bereketab, Hongwei Wang, Patrick Mish and William J. Devenport
Department of Aerospace and Ocean Engineering,
215 Randolph Hall, Virginia Tech, Blacksburg VA 24061.

November 2000

ABSTRACT

Two grids have been developed for the Virginia Tech 6' x 6' Stability wind tunnel for the purpose of generating homogeneous isotropic turbulent flows for the study of unsteady airfoil response. The first, a square bi-planar grid with a 12" mesh size and an open area ratio of 69.4%, was mounted in the wind tunnel contraction. The second grid, a metal weave with a 1.2" mesh size and an open area ratio of 68.2% was mounted in the tunnel test section. Detailed statistical and spectral measurements of the turbulence generated by the two grids are presented for wind tunnel free stream speeds of 10, 20, 30 and 40m/s. These measurements show the flows to be closely homogeneous and isotropic. Both grids produce flows with a turbulence intensity of about 4% at the location planned for the airfoil leading edge. Turbulence produced by the large grid has an integral scale of some 3.2 inches here. Turbulence produced by the small grid is an order of magnitude smaller. For wavenumbers below the upper limit of the inertial subrange, the spectra and correlations measured with both grids at all speeds can be represented using the von Karman interpolation formula with a single velocity and length scale. The spectra maybe accurately represented over the entire wavenumber range by a modification of the von Karman interpolation formula that includes the effects of dissipation. These models are most accurate at the higher speeds (30 and 40m/s).

TABLE OF CONTENTS

1. INTRODUCTION

The prediction of the broadband noise and vibration produced by a lifting surface passing through a turbulent flow is one of the classic problems of aeroacoustics. When the turbulent fluctuations are weak and their effects primarily inviscid this problem can be linearized (e.g. Amiet, 1975). In this case, the unsteady surface pressure field on the lifting surface (and thus the noise and vibration) can be expressed in terms of the velocity space time correlation of the undisturbed turbulent flow and the response function of the lifting surface – an expression of the linearized relationship between the turbulent correlations and the space-time correlation of the pressure field that they produce on the blade.

In the 1970's a number of authors, for example Adamcyzk (1974) and Amiet (1976), formulated analytic solutions to the response function for an airfoil using the linearized Euler equation. These formulations provided closed-form expressions for the foil response to arbitrary skewed sinusoidal gusts interacting with the blade in compressible flow (the turbulence spectrum being represented as a linear sum of such gusts). However, they were based upon very simple models of the blade, typically a two-dimensional flat plate at zero angle of attack. Such models were validated against measurements such as those made by Paterson and Amiet (1976), which revealed the form of the surface-pressure cross spectrum at a few selected points on an airfoil surface. In recent years more sophisticated, computational, models for the response function have been under development. These methods (still using Euler's equation, most often in the form of rapid distortion theory) include the effects of airfoil thickness and angle of attack (e.g. Attassi et al, 1989, 1993a, 1993b, 1997) and the linearized evolution of the turbulence as it convects through the airfoil flow field. The purpose of this study is to provide the experimental data needed to validate this new generation of models. Our goals are;

1. To measure the full four-dimensional form of the surface pressure cross-spectrum experienced on a standard airfoil immersed in homogeneous turbulence.

2. To relate this to the spectrum of the undisturbed turbulence and the behavior of the turbulence as it encounters the airfoil.
3. To highlight effects on this spectrum that are not easily modeled, such as those due to distortion and convection of the turbulence, of angle of attack, and of finite thickness and stall.

With these goals in mind, two approximately homogeneous isotropic turbulent flows have been produced in the test section of a large wind tunnel. The turbulent flows have been characterized through single and two-point velocity and turbulence. Their lengthscales have been characterized, and their spectra compared with standard forms. A 2-foot chord NACA 0015 airfoil model, instrumented with 96 subsurface pressure transducers has been introduced into both these flows and detailed measurements of the surface pressure cross-spectrum have been made, as well has measurements of the correlation of the instantaneous surface pressure field and the near-surface velocity fluctuations. These measurements have been made as a function of angle of attack up to, and beyond stall.

This report is divided into two volumes. In this first volume we describe the velocity measurements used to characterize the two undisturbed turbulent flow fields, as well as related apparatus, instrumentation and hardware. The airfoil model, its instrumentation, and the surface pressure results are presented and discussed in the second volume (Mish *et al.*, 2001).

2. APPARATUS AND INSTRUMENTATION

2.1 Wind Tunnel

All measurements were performed in the Virginia Tech Stability Wind Tunnel. The tunnel is a continuous, closed jet, single return, subsonic wind tunnel with a 6'x6' test section 24 feet in length. The general design layout is in Figure 1. The tunnel is powered by a 600hp DC motor driving a 14 foot propeller providing to a maximum speed of about 60m/s. Tunnel speed is regulated by a custom designed Emerson VIP ES-6600 SCR Drive. Turbulence levels in the test section are extremely low, on the order of .05% or less, and flow in the empty test section is closely uniform (see Choi and Simpson, 1987). Although not originally designed as a low turbulence facility, the addition by the NACA of seven anti-turbulence screens, coupled with the other flow smoothing features of the tunnel, resulted in very low turbulence levels. Acoustic noise levels in the empty wind tunnel are surprisingly low (see Larssen and Devenport 1999) and appear dominated by broadband noise from turbulence ingested into the drive propeller. The characteristics of this noise, and its impact on the present study are discussed in detail in more detail in volume 2 of this report.

2.2 Turbulence generating grids

Two grids were used to generate two approximately homogeneous turbulent flows of distinctly different characteristics. The first, or 'large' grid, is illustrated schematically in figures 2 and 3. The purpose of this grid was to generate turbulence scales large enough to be comparable to the airfoil thickness and chord. This grid was mounted in the wind tunnel contraction 103.5" upstream of the test section entrance, at a location where the cross-sectional area was 32% greater than that of the test section. This location was chosen for several reasons. First, it is well known that grid turbulence tends to be anisotropic because the blockage of the grid causes the flow to decelerate after it passes through the grid cells. This can be corrected by placing a contraction of about 30% downstream of the grid (see Comte-Bellot and Corrsin, 1966). Second, this location gave a longer development length for the turbulence (and thus a greater integral scale). Third, placing the grid in the contraction reduced the flow velocity over it, and thus the drag and

noise it produced. Fourth, initial tests with a grid located at the test-section entrance showed this to produce a relatively inhomogeneous, anisotropic and noisy flow unsuitable for present purposes.

The large grid consists of seven 7' long horizontal rectangular cross-section steel bars, each 2" in width, 1" in depth and placed 12" centers, and seven similar vertical bars. Together these form a square bi-planar grid with a 12" cell size and an open area ratio of 69.4%. To reduce grid generated noise foam wedges were glued to the downstream-facing sides of the steel bars. In cross-section the wedges, shown in figure 3, were 4" in length, 2" wide at the base (glued to the bars) tapering to 0.4" wide at the tip. Wedges were not placed on overlapping sections of the bars (figure 3). A photograph of the assembled grid (as seen from downstream) is shown in figure 4.

The second, or 'small' grid is shown schematically in figures 2 and 5. The purpose of this grid was to generate turbulence scales small enough to be comparable with the leading edge radius of the airfoil. Such small scales can only be generated with a very short development length and thus this grid was cited in the wind tunnel test section 107" downstream of its entrance, at a location only 19" upstream of the ultimate position of the airfoil leading edge. This grid consisted of a metal weave fabricated from of steel bar 0.2" in diameter woven to form a mesh with cells 1.15" square and an open area ratio of 68.2%. The weave was welded to a 6' x 6' frame bolted to the inside of the wind tunnel walls. The frame, constructed from angle iron, projected some 1.7" inward from the tunnel sidewalls, producing a small additional blockage to the flow in this region. Figure 6 shows a complete view of the grid outside of the wind tunnel. One imperfection in this grid, not visible, in the photograph is that its center is bowed outward (in the downstream direction when mounted in the test section) by about 0.4".

2.3 Hot-wire Anemometry

To document the characteristics of the two grid-generated turbulent flows velocity measurements were made using hot-wire probes. These measurements were all made with the wind tunnel test section empty, except for the grid and traverse gear, at the streamwise location planned for the airfoil leading edge.

Three-component single and two-point velocity measurements were made using two miniature Kovaznay-type four-sensor probes manufactured by Auspex Corporation (type AVOP-4-100), as shown in figure 7. The tip of each probe consists of eight stainless steel tapered prongs (75μm in diameter at their tips) that hold the sensor wires some 40 mm upstream of the main part of the probe. The sensor wires are made of etched tungsten wire of 5 μm diameter and approximately 0.8 mm in length with length to diameter ratio of 160. The wires are arranged in 2 orthogonal X-wire arrays and are inclined 45° to the probe axis. The total measurement volume is approximately 0.5 mm^3.

Each of the sensor wires of both probes was operated a Dantec 56C17 bridge and Dantec 56C01 constant temperature anemometer unit. The bridges were optimized to give a frequency response greater than 25 kHz. Output voltages from the anemometer bridges were amplified by a x10 buck-and-gain amplifiers with calibrated RC-filters to limit their frequency response to 50 kHz. The amplified signal was then recorded by a Hewlett Packard (HP) data acquisition system. The HP system also sampled output voltages from a pressure transducer reading reference dynamic pressure and a digital thermometer reading flow temperature.

Probes were calibrated for velocity before and after each measurement inside the wind tunnel by placing them in the uniform jet of a TSI calibrator and fitting the measured relationship between sensor voltage and cooling velocity to King's law. Probes were calibrated for angle directly by pitching and yawing them in the jet. With a total of about 300 angle combinations a look-up table relating the measured cooling velocities to the actual velocity components could be established covering the full acceptance cone of the probe. Angle calibrations were performed for both probes at flow velocities of 20 and 40m/s, although the variation in calibration with flow speed was found to be small. For full details of the angle calibration process and typical calibrations see Wittmer *et al.* (1998).

Since measurement of two-point correlations and spectra was part of this experiment, it was necessary to measure and compare the frequency response of each of the sensors both probes. Figure 8 shows is a schematic flow chart of the hot-wire frequency calibration system. In order to inspect the frequency response of each probe, a pulsed YAG laser was used. Each sensor, placed in a flow having the same velocity as

that for the experiment, was subjected to nano-second laser pulses at a rate of about 10Hz. The signal output from the anemometers, revealing the impulse response of the system, was recorded using a Rapid Systems R2000 8-bit 20M sample/sec A/D converter system. The impulse response signals were phase aligned using the trigger signal from the laser and recorded over many realizations to obtain an average of the behavior. The data was then Fourier transformed to obtain the characteristic phase and frequency response of the sensors. It was found that the form and shape of the optimized frequency response of the sensors depends on the length of the probe cables. By adjusting the length the frequency response of the each sensor was obtained. Figure 9 shows typical amplitude and phase response for each of the four sensors for the moving and fixed probe at two speeds. The result shows flat amplitude and matched phase-response characteristics to beyond 10kHz, sufficient for the present work.

Single-component turbulence measurements were also made using a TSI 1210-T1.5 hot-wire probe. This probe was operated and calibrated in much the same way as the four sensor probes, with the exception that no angle calibration was performed or needed.

2.4 Probe holder and traverse

The 2-axis wind tunnel traverse shown in figure 10 was used to position both 4-sensor and single sensor probes in the test section. The traverse, which is capable of positioning a probe to within about 0.025mm (see Zsoldos, 1992), is mounted in the test section. Probes were supported on a tapered mount which placed the measurement volume between 16" and 24" upstream of the traverse.

For the two-point measurements one of the probes was positioned using the traverse (the 'moving probe') while the second 'fixed' probe was held in a static support. The support, shown in figure 11, consisted of a two-section tapered airfoil-section strut, braced against vibration using an arrangement of steel wires and turnbuckles. The strut held the probe at a location about 4" above the test section centerline in the 10"-long holder shown in figures 12 and 13. Both probes were set at the same streamwise location for all two-point measurements, while the wind tunnel traverse was used to vary the probe separation in the crossflow plane.

3. RESULTS AND DISCUSSION

3.1 Coordinate system, measurement conditions.

All measurements were performed at the same station, illustrated in figure 2, located 126 inches downstream of the test section entrance. This position was chosen as it corresponds to the location where the airfoil leading edge was placed during the subsequent pressure measurements. With the small grid installed this position was 19 inches, or 16.1 mesh sizes, downstream of the grid. With the large grid installed this position was 229.5 inches, or 19.1 mesh sizes, downstream of that grid.

Figure 14 also shows the coordinate system used in presenting measurements. Coordinate x denotes distance measured downstream from the measurement plane, y vertically upward from the tunnel centerline, and coordinate z horizontally from the tunnel centerline so as to complete a right handed system. Mean and fluctuating velocity components (U,V,W) and (u,v,w) and also defined in the directions of x, y and z. Most velocity measurements are normalized on the free stream velocity U_∞ sensed using a Pitot static probe located just downstream of the wind tunnel entrance. Measurements were made for nominal free-stream velocities of 10, 20, 30 and 40 m/s, corresponding to the actual Reynolds numbers listed in the table below. This table includes Reynolds number based on the chord of the NACA 0015 airfoil used in the subsequent surface pressure measurements.

Nominal Flow Speed (m/s)	Small Grid Re	Large Grid Re	Equivalent airfoil chord Re
10	20207	217376	327742
20	39371	416505	655484
30	63370	632982	983226
40	79926	798893	1310968

***Table 1**. Flow speeds and Reynolds numbers.*

The 4-sensor single and two point measurements were all recorded at a sampling rate of 51.2kHz in 100 records of 4096 points. The uncertainties in these measurements were calculated using the method of Kline and McClintock (1953) for confidence limits of 95% and are listed in table 2. The uncertainties vary with flow speed and grid size because they are strongly dependent upon the relative size of the integral timescale and the fixed sampling period.

	Large grid				Small Grid			
Nominal flow speed (m/s)	10	20	30	40	10	20	30	40
Mean velocity (%Uinf)	2%	1%	1%	1%	2%	1%	1%	1%
u^2/Uinf^2	9%	6%	5%	4%	5%	3%	2%	2%
v^2/Uinf^2 and w^2/Uinf^2	12%	9%	9%	8%	9%	7%	7%	7%
Correlation coefficient	0.09	0.06	0.05	0.04	0.03	0.02	0.02	0.02
Spectral level	16%	14%	14%	13%	14%	13%	13%	13%

***Table 2**. Uncertainties in measurements made with the four-sensor probes*

The single hot wire measurements were only made with the large grid. All measurements were inferred from sequences of 100 point records, each 4096 points in length, recorded at a sampling rate of 25.6kHz. These measurements therefore provided some additional spectral information at the lowest frequencies. Uncertainties in these measurements are listed in table 3.

	Large grid			
Nominal flow speed (m/s)	10	20	30	40
Mean velocity (%Uinf)	2%	1%	1%	1%
u^2/Uinf^2	7%	5%	4%	3%
Correlation coefficient	0.06	0.04	0.03	0.03
Spectral level	14%	12%	12%	12%

***Table 3**. Uncertainties in measurements made with the single-sensor probe*

3.2 Mean flow and turbulence fields

Three-component velocity and turbulence measurements were made with the 4-sensor probes over a 24"x24" cross section centered on the tunnel centerline in order to reveal the form of the grid generated flows. Measurements are plotted in figures 14 through 21 in terms of contours of mean streamwise velocity and of the three Reynolds normal stresses, and in terms of mean cross-flow velocity vectors.

The mean streamwise velocity contours and turbulence stress contours measured with the large grid appear consistent with a uniform mean flow and homogeneous turbulent field (figures 14 to 17). This is not to say that there are no variations in the plotted quantities but that what variations can be seen appear random and consistent with the uncertainty estimates above (even to the extent that the variations decrease with increase in flow speed). Non-random variations are visible in the mean cross-flow velocity vectors (parts (b) of these figures). At all speeds these show a general convergence of the streamlines on the tunnel axis. The implied angles are small (one

degree at maximum) and appear consistent with the convergence of the flow in the empty test section measured by Choi and Simpson (1987). They suggest that this partly caused by the upstream influence of the traverse gear (figure 10) and by the slight acceleration of the flow in the test section as a result of boundary layer growth on the side walls. However, this latter effect should be very small, accounting for flow angles of less than 0.1^{o}, and thus we believe this non-uniformity is produced by the traverse.

Cross-sectional average turbulence intensities with the large grid (figure 22a) are between 3% and 4% at all speeds and in all components. Turbulence levels appear slightly lower at 20m/s than at other speeds. The isotropy of the turbulence components appears best at 30m/s where the difference between the smallest and largest components is less than 5% of the measured intensity.

Figures 18 to 21 show that the flow with the small grid is slightly less homogeneous. While the measurements show the same type of random variations associated with uncertainty, a comparison of the results from all speeds show some small but consistent variations over the cross-section. Mean streamwise velocity (figures 18a to 21a) is, in most cases, slightly larger at the top and bottom of the measured region than at its mid height. The contours of $\overline{v^2}$ (18d to 21d) show on-the-whole larger levels near the tunnel centerline than elsewhere, while those of $\overline{w^2}$ (18e to 21e) show the reverse trend. Curiously the mean crossflow vectors (18b through 21b) are more homogeneous than with the large grid and show no mean convergence of the flow field. We believe these effects may be a consequence of the slight bow in this grid (about 0.4" at the grid center in the downstream direction) discussed above, and the blockage produced by the grid frame. The bowing of the grid would tend to produce non-uniformity in the stress fields and a slight turning of the flow away from the tunnel centerline that could counteract the convergence associated with traverse interference.

Cross-sectional averaged turbulence intensities with the small grid (figure 22b) are similar to those produced by the large grid, being between 3.5% and 5% at all speeds. Unlike the large grid, the small grid produces a consistent increase in turbulence level with flow speed. The isotropy of the turbulence intensities is fairly poor at 10m/s but improves markedly with speed, the difference between the smallest and largest components at 30m/s being less than 1 part in 20.

3.3 Time Spectra.

Time spectra were measured near the tunnel centerline using the two four sensor hot wire probes and the single hot-wire probe. Results for both grids are shown in figures 23 through 30. The data are plotted as streamwise wavenumber spectra assuming Taylor's hypothesis, i.e.

$$E_{uu}(k_x) = \frac{G_{uu}(f)U_\infty}{2\pi}$$

where E_{uu} is the one-dimensional wavenumber spectrum of the u velocity component, in meters^3/second^2, G_{uu} is the time spectrum, in meters^2/second, f is frequency in Hz, and k_x is streamwise wavenumber calculated as $2\pi f/U_\infty$, with similar expressions for v and w. Note that we have plotted $E_{uu}(k_x)$ (the longitudinal spectrum) separately from $E_{vv}(k_x)$ and $E_{ww}(k_x)$ (the lateral spectra). In truly homogeneous isotropic turbulence $E_{vv}(k_x)$ and $E_{ww}(k_x)$ would be identical.

The spectra are plotted normalized on the characteristic wavenumber k_e, related to the longitudinal integral scale of the turbulence L as,

$$k_e = \sqrt{\pi}\,\frac{\Gamma(\frac{5}{6})}{\Gamma(\frac{1}{3})}\,\frac{1}{L}$$

(see Hinze, 1975, p. 248), where $\Gamma()$ refers to the gamma function. The integral scale can be inferred from the low-frequency limit of the measured longitudinal spectrum, from the low-frequency limits of the lateral spectra, or by integrating any of the 6 spatial correlation functions measured for each flow condition (see below). With truly homogeneous isotropic turbulence, and in the absence of experimental uncertainty, all these methods would produce the same result. In reality, of course, they do not so we instead have chosen a single integral scale for each flow condition that best represents all the experimental data for that case. These integral scales are listed in table 4. Corresponding 'isotropic' velocity scales u' (determined from the mean (over component) of the square of the cross-sectional averaged turbulence intensities of figure 22) are also listed.

	Large grid				Small Grid			
	10m/s	20m/s	30m/s	40m/s	10m/s	20m/s	30m/s	40m/s
u'/U_∞ (%)	3.77%	3.56%	3.93%	3.80%	3.99%	4.11%	4.35%	4.67%
L (in.)	3.18	3.17	3.22	3.29	0.322	0.323	0.309	0.304
L/c	0.132	0.132	0.134	0.137	0.0134	0.0135	0.0129	0.0127
L/r_c	5.34	5.33	5.41	5.52	0.541	0.543	0.519	0.512

Table 4. Longitudinal integral scales (L) and velocity scales (u') that best describe the 8 grid turbulence flows. Integral scale also shown normalized on the chord (c) and leading edge radius (r_c) of the airfoil used in part 2 of this study (Mish et al., 2001).

The spectra are compared with curves representing the von Karman interpolation formula for homogeneous turbulence. The equations describing these curves are, for the longitudinal spectrum,

$$E_{uu}(k_x) = \frac{2}{\sqrt{\pi}} \frac{\Gamma(\frac{5}{6})}{\Gamma(\frac{1}{3})} \frac{u'^2}{k_e} \left[1 + \left(\frac{k_x}{k_e} \right)^2 \right]^{-\frac{5}{6}}$$

(Hinze, 1975, pp.247) and for the lateral spectrum,

$$E_{vv}(k_x) = E_{ww}(k_x) = \frac{1}{\sqrt{\pi}} \frac{\Gamma(\frac{5}{6})}{\Gamma(\frac{1}{3})} \frac{u'^2}{k_e} \left[1 + \frac{8}{3} \left(\frac{k_x}{k_e} \right)^2 \right] \left[1 + \left(\frac{k_x}{k_e} \right)^2 \right]^{-\frac{11}{16}}$$

(Amiet, 1975) The three-dimensional energy spectrum function from which these are inferred is

$$E(k) = \frac{55}{9\sqrt{\pi}} \frac{\Gamma(\frac{5}{6})}{\Gamma(\frac{1}{3})} \frac{u'^2}{k_e} \left(\frac{k}{k_e} \right)^4 \left[1 + \left(\frac{k}{k_e} \right)^2 \right]^{-\frac{17}{6}}$$

(Hinze, 1975, pp.247), where k is the magnitude of the wavenumber vector, and k_e was obtained from the integral scale estimates in table 4. Note that the von Karman formula can only provide a reasonable representation of the homogeneous turbulence spectrum at wavenumbers below the upper limit of the inertial subrange.

The formula can be extended to cover the entire wavenumber range by combining it with the high-wavenumber interpolation formula of Panchev and Kesich (Hinze, 1975, pp. 241),

$$E(k) = (\varepsilon \nu^5)^{\frac{1}{4}} \left[\left(\frac{2}{3\alpha^2} \right)^{\frac{1}{3}} \left(\frac{k}{k_d} \right)^{-\frac{5}{3}} + \frac{1}{\alpha} \left(\frac{k}{k_d} \right)^{-1} \right] \exp\left[-\frac{3}{2} \left(\frac{2}{3\alpha^2} \right)^{\frac{1}{3}} \left(\frac{k}{k_d} \right)^{\frac{4}{3}} - \frac{1}{\alpha} \left(\frac{k}{k_d} \right)^2 \right]$$

where $k_d = (\varepsilon/\nu^3)^{0.25}$, the inverse of the Kolmogorov length scale, and α is a dimensionless constant. Here ε represents the dissipation rate of turbulence kinetic energy. Since both these expressions apply in the inertial subrange, the constant α can be determined by the matching, and the expressions can be combined into a single formula,

$$E(k) = \frac{55}{9\sqrt{\pi}} \frac{\Gamma(\frac{5}{6})}{\Gamma(\frac{1}{3})} \frac{u'^2}{k_e} \left(\frac{k}{k_e}\right)^4 \left[1+\left(\frac{k}{k_e}\right)^2\right]^{\frac{17}{6}} \left[1+\frac{1}{\alpha}\left(\frac{k}{k_d}\right)^{\frac{2}{3}}\left(\frac{2}{3\alpha^2}\right)^{-\frac{1}{3}}\right]$$
$$\times \exp\left[-\frac{3}{2}\left(\frac{2}{3\alpha^2}\right)^{\frac{1}{3}}\left(\frac{k}{k_d}\right)^{\frac{4}{3}} - \frac{1}{\alpha}\left(\frac{k}{k_d}\right)^2\right]$$

where α is determined as

$$\alpha = \sqrt{\frac{18\sqrt{\pi}\Gamma(\frac{1}{3})}{165\Gamma(\frac{5}{6})}} \frac{\varepsilon}{k_e u'^3} = 0.6774... \frac{\varepsilon}{k_e u'^3}$$

Note that it is necessary to use numerical integration to determine the one-dimensional spectral forms implied by this formula. It is also necessary to determine α and k_d, which requires knowledge of the dissipation. Rather more convenient expressions are obtained when these parameters are expressed in terms of the Taylor microscale λ and its Reynolds number R_λ. These are defined as

$$\lambda \equiv \frac{u'}{\sqrt{\overline{\left(\partial u/\partial x\right)^2}}} = \sqrt{\frac{15\nu u'^2}{\varepsilon}}$$

and

$$R_\lambda = \frac{\lambda u'}{\nu}$$

and provide the following expressions for α and k_d

$$\alpha = 15\sqrt{\frac{18\sqrt{\pi}\Gamma(\frac{1}{3})}{165\Gamma(\frac{5}{6})}} \frac{1}{R_\lambda k_e \lambda} = 10.1613... \frac{1}{R_\lambda k_e \lambda}$$

$$\frac{k_d}{k_e} = \frac{15^{\frac{1}{4}} R_\lambda^{\frac{1}{2}}}{k_e \lambda}$$

The values of the Taylor microscale for the 8 flows was determined by comparing the curves implied by this modified von Karman interpolation formula with the measured spectra. To provide a check, the microscales were also estimated by integrating the second moment of the spectra. Specifically, the microscale can be expressed in terms of the time derivative of velocity using Taylor's hypothesis.

$$\lambda \equiv \frac{u'}{\sqrt{\overline{\left(\partial u/\partial x\right)^2}}} = \frac{u'U_\infty}{\sqrt{\overline{\left(\partial u/\partial t\right)^2}}}$$

From the Fourier transform relationship between the time spectrum and the time delay correlation we can calculate

$$\overline{\left(\partial u/\partial t\right)^2} = 4\pi^2 \int_0^\infty f^2 G_{uu}(f)df$$

Accurate determination of this integral requires very good resolution of the high-frequency end of the spectrum. This is a function of the size of the probe (0.8mm, 0.03in.) and the sampling rate of the signals compared to the microscales of the turbulence. Because of these limitations reliable estimates could only be obtained by this means in the lower speed (10 and 20m/s) flows.

3.3.1 Large grid

All velocity spectra measured with the large grid (figures 23 to 26) show a region of nearly constant negative slope that we identify as the inertial subrange. As one would expect, the size of this region increases with flow speed, extending over about two decades of wavenumber at the highest speeds. The agreement between the measured spectra and the modified von Karman model appears surprisingly good at all speeds. The largest discrepancies appear in the inertial subrange itself and diminish with increase in flow speed. The reason for this is that the -5/3 slope of the inertial subrange implicit in the von Karman and Panchev and Kesich models is only actually achieved in the limit of infinite Reynolds number. Mydlarski and Warhaft (1996) show (as do the present data) that the slope of the inertial subrange at practically achievable Reynolds numbers is slightly less, the difference decreasing with increase in Reynolds number. Their streamwise velocity spectra show slopes that vary from -1.4 to -1.58 as the Taylor

Reynolds of the turbulence is increased from 99 and 448. The present large-grid spectra show slopes decreasing from -1.37 to -1.54 as the free-stream speed is increased from 10 to 40m/s, corresponding to a change in Taylor Reynolds number (see below) from 172 to 405.

Figures 23 to 26 show that the relatively high-sampling rate and short record length used with the four-sensor probes captures the high-frequency roll off of the spectra fairly well at all speeds (with the exception of some spikes related to electrical noise). However at low frequencies the spectra appear clipped. Conversely, the slower sampling rate and longer records used with the single hot-wire measurements, clip the high-frequency end of the spectra but (at speeds above 10m/s) clearly show the low-frequency asymptote.

Estimates of Taylor and Kolmogorov microscales and the Taylor Reynolds numbers obtained by fitting the modified interpolation formula to the measured spectra, are listed in table 5 and compared in figure 31. If we assume that the normalized decay of turbulence kinetic energy with distance downstream of the grid was the same at all Reynolds numbers then the Taylor microscale should vary as the inverse square root of the flow velocity. Curves illustrating this expected trend included in figure 31 and do appear consistent with the results. A further check is provided by the integration of the second moment of the velocity spectra at 10 and 20m/s. The estimates obtained by this method appear a little low (perhaps because of uncertainty in the integration process) but otherwise consistent.

	Determined by comparison with interpolation formula			Determined by integration of spectra		
Nominal U_∞ (m/s)	λ(in.)	R_λ	η (in.)	λ (in.)	R_λ	η (in.)
10	0.39	172	0.0152	0.34	150	0.0142
20	0.29	256	0.0091	0.22	214	0.0077
30	0.25	337	0.0069	-	-	-
40	0.22	405	0.0056	-	-	-

Table 5. *Estimates of Taylor and Kolmogorov microscales (λ and η) and Taylor Reynolds numbers (R_λ). Large grid.*

3.3.2 Small grid

The velocity spectra measured with the small grid (figures 27 to 30) reflect the lower Reynolds number of the turbulence produced by this smaller mesh. At 10m/s the

spectra barely show any constant-slope inertial subrange at all. As the speed increases, however, a significant subrange does develop and some increase in the magnitude of the inertial-subrange slope with Reynolds number is apparent here, just as with the large grid. With the exception of this change in subrange slope, the modified von Karman interpolation formula provides a surprisingly good model of the data over the entire measured wavenumber range. Estimates of Taylor and Kolmogorov microscales and the Taylor Reynolds numbers obtained in fitting this formula to the data, are listed in table 6 and plotted in figure 32. Again these results appear consistent with the expected approximately square root variations with flow velocity. Checks provided by the integration of the second moment of the velocity spectra at 10 and 20m/s again appear a little low, but we do not believe this difference is significant given the probable uncertainty in these values.

	Determined by comparison with interpolation formula			Determined by integration of spectra		
Nominal U_∞ (m/s)	λ(in.)	R_λ	η (in.)	λ (in.)	R_λ	η (in.)
10	0.110	77	0.0063	0.091	64	0.0058
20	0.082	115	0.0039	0.065	91	0.0034
30	0.069	144	0.0029	-	-	-
40	0.061	167	0.0024	-	-	-

Table 6. *Estimates of Taylor and Kolmogorov microscales (λ and η) and Taylor Reynolds numbers (R_λ). Small grid.*

3.4 Space and Time Correlation Functions

Space and time correlation functions measured with the two grids are presented in figures 33 through 40. We define the correlation function defined as, for example,

$$R_{vv}(z) = \frac{\overline{u(0,0,0)u(0,0,z)}}{\overline{u(0,0,0)^2}}$$

with similar expressions for the v and w velocity components and for separations in the y and x directions. Correlations in the y and z directions were determined from the two-point four-sensor-probe measurements by averaging over all 100 4096-point records measured for each probe separation (a total averaging time of over two minutes). Correlations in the x direction were obtained using Taylor's hypothesis by inverse Fourier transforming the velocity spectra measured with the four-sensor probes (for the small grid) and with the single hot-wire probe (for the large grid). Correlations in the x

direction could not be inferred from the four-sensor probe measurements made with the large grid since (as evidenced in the velocity spectra) the measured record lengths were too short compared to the integral timescale of the flow. The origin for the two point measurements in the above equation was 4" above the tunnel centerline for the four-sensor measurements, and at the tunnel centerline for the single hot-wire results.

In a truly isotropic turbulent flow all the longitudinal correlations $R_{uu}(x)$, $R_{vv}(y)$ and $R_{ww}(z)$ would be identical, and so we have plotted them together and compared them with the longitudinal correlation function implied by the von Karman interpolation formula and the integral scales given in table 4,

$$f(x) = \frac{2^{2/3}}{\Gamma(\frac{1}{3})}(k_e x)^{1/3} K_{1/3}(k_e x)$$

(see Hinze, 1975, pp. 247). Likewise the lateral correlations $R_{uu}(y)$, $R_{uu}(z)$, $R_{vv}(x)$, $R_{vv}(z)$, $R_{ww}(x)$ and $R_{ww}(y)$ would be the same, so they are plotted together and compared with the von Karman lateral correlation function,

$$g(x) = \frac{2^{2/3}}{\Gamma(\frac{1}{3})}(k_e x)^{1/3}\left[K_{1/3}(k_e x) - \frac{k_e x}{2} K_{-2/3}(k_e x) \right]$$

where $K()$ represents the modified Bessel function.

In most cases the measurements show the flow to be consistent with the expectations of isotropy, and the von Karman forms to within the uncertainty estimates given in tables 2 and 3. The agreement is not perfect, however. With the large grid, the longitudinal correlation $R_{ww}(z)$ decays a little more slowly than that of the other components at all speeds. At all speeds the small grid produces turbulence in which the longitudinal correlation of w component fluctuations $R_{ww}(z)$ decays a little more rapidly than that of the other components. At the highest speeds this grid also produces turbulence in which the lateral correlation $R_{ww}(y)$ decays a little too fast, and the correlation $R_{uu}(z)$ a little too slowly to be exactly consistent with isotropy.

For completeness, figures 41 through 47 show two-dimensional cuts through the correlation functions measured with the small grid. The cuts, defined as

$$R_{uu}(x,z) = \frac{\overline{u(0,0,0)u(x,0,z)}}{\overline{u(0,0,0)^2}}$$

$$R_{uu}(x,y) = \frac{\overline{u(0,0,0)u(0,y,z)}}{\overline{u(0,0,0)^2}}$$

with similar expressions for v and w component fluctuations were plotted by inverse Fourier transforming the two-point cross spectra measured with the four sensor probes, and by using Taylor's hypothesis to relate the resulting time-delay correlations to x-wise correlations. This calculation could not be performed for the large-grid data as in this case the measured record lengths were too short compared to the integral timescale of the flow for the time-delay correlation to be reliably determined.

4. CONCLUSIONS

Two grids have been developed for the Virginia Tech 6' x 6' Stability wind tunnel for the purpose of generating homogeneous isotropic turbulent flows for the study of unsteady airfoil response. The first, a square bi-planar grid with a 12" mesh size and an open area ratio of 69.4%, was mounted in the wind tunnel contraction 19.1 mesh sizes upstream of the location planned for the airfoil leading edge, at a point where the cross-sectional area was 32% larger than that of the test section. Acoustic foam wedges attached to the downstream side of the grid were used to minimize grid generated noise. The second grid, a metal weave with a 1.2" mesh size and an open area ratio of 68.2% was mounted in the tunnel test section at a position 16.1 mesh sizes upstream of the planned leading edge location.

Measurements of the turbulence generated by the two grids were made at the planned leading edge location for wind tunnel free stream speeds of 10, 20, 30 and 40m/s. Cross-sectional 3-component turbulence measurements were made to examine the homogeneity and isotropy of the turbulence over a 2-foot square region at the test section center. Single and three-component velocity spectra were also measured near the tunnel centerline. Two-point three component measurements were also made of the space and time correlations of the turbulence in this region. These measurements have been analyzed in detail and the following conclusions are drawn.

1. Turbulence intensities produced by the large grid are between 3% and 4% at all speeds and in all components. The isotropy of the turbulence components appears best at 30m/s where the difference between the smallest and largest components is less than 5% of the measured intensity. The turbulence stress field is closely homogeneous at all flow speeds.

2. Turbulence intensities produced by the small grid are between 3.5% and 5% at all speeds and in all components. The isotropy of the turbulence improves markedly with speed, the difference between the smallest and largest components at 30m/s being less than 1 part in 20. The turbulence stress field shows some slight inhomogeneities at all flow speeds, attributed to a slight bow in this grid (about 0.4" at the grid center in the downstream direction), and the blockage produced by the frame used to support it.

3. Time spectra and spatial correlations were used to determine the integral scales of the turbulence. In all cases the large grid produced integral scales of about 3.2" and the small grid scales of about 0.32". These correspond to about 13% and 0.13% of the airfoil to be used in these flows, and about 500% and 50% of its leading edge radius, respectively.

4. Time spectra measured with the large grid show the turbulence to be of fairly high Reynolds number. Taylor Reynolds numbers vary from 172 at 10m/s to about 405 at 40m/s. At all speeds the spectra show inertial subranges that increase in slope and in extent with increase in Reynolds number. The slight increase in the slope of the inertial subrange is consistent with the findings of earlier homogeneous turbulence studies.

5. The spectra reveal the small grid turbulence to be of significantly lower Reynolds number (Taylor Reynolds numbers from 77 to about 167), and a clear inertial subrange is only apparent at the higher speeds.

6. Space and time correlations measured with both grids at all speeds show only minor deviations from the symmetries expected of truly isotropic homogeneous turbulence.

7. For wavenumbers below the upper limit of the inertial subrange, the spectra and correlations measured with both grids at all speeds can be represented using the von-Karman interpolation formula with the single velocity and length scales listed in table 4.

8. The spectra maybe accurately represented over the entire wavenumber range by a modification of the von Karman interpolation formula that includes the effects of dissipation, specified using the Taylor Reynolds number and microscale estimates listed on the left hand sides of tables 5 and 6.

9. The above models are most accurate at the higher speeds (30 and 40m/s) where the turbulent flows most closely isotropic, their spectra contain the longest inertial subranges, and the inertial subrange slope is closes to -5/3.

ACKNOWLEDGEMENTS

The authors would like to acknowledge the support of NASA Langley, particularly Casey Burley and Tom Brooks, for their support of this work through grant NAG 1-1942.

REFERENCES

Adamczyk, John J., *Passage of a Swept Airfoil through an Oblique Gust*, J. Aircraft, May 1974

Amiet R K, 1975, *Acoustic radiation from an airfoil in a turbulent stream*, Journal of Sound and Vibration, vol. 41, pp. 407-420.

Amiet, Roy K., *High Frequency Thin-Airfoil Theory for Subsonic Flow*, AIAA Journal, Vol. 14 No. 8, August 1976

Atassi H M, Dusey M and Davis C, 1993a, *Acoustic radiation from a thin airfoil in non-uniform subsonic flows*, AIAA Journal, vol. 31, pp. 12-19.

Atassi H M, Fang J and Patrick S, *Direct calculation of sound radiated from bodies in non-uniform flow*s, Journal of Fluids Engineering, vol. 115, pp. 573-579, December 1993b.

Atassi H M and Grzedzinski J, *Unsteady disturbances of streaming motions around bodies*, Journal of Fluid Mechanics, vol. 209, pp. 385-403, 1989.

Attassi H, *Aeroacoustics of non-uniform flows*, AIAA 97-0378

Choi K and Simpson R L, 1987, *Some Mean-Velocity, Turbulence and Unsteadiness Characteristics of the VPI&SU Stability Wind Tunnel*, Report VPI-AOE-161, VPI&SU, Blacksburg VA.

Comte-Bellot G and Corrsin S, 1966, *The use of a contraction to improve the isotropy of grid-generated turbulence,* Journal of Fluid Mechanics, vol. 25, pt. 4, pp. 657-682.

Hinze J O, 1975, *Turbulence*, McGraw Hill, New York.

Kline S J and McClintock F A, 1953, *Describing Uncertainties in Single Sample Experiments*, Mechanical Engineering (ASME), vol. 75, pp.3.

Larssen J V and Devenport W J, *Acoustic Properties Of The Virginia Tech Stability Wind Tunnel*, Department of Aerospace and Ocean Engineering, Virginia Tech, Blacksburg, Virginia 24061, Report VPI-AOE-263. Avail: http://www.aoe.vt.edu/aoe/physical/vpi-aoe-263.pdf

Mish P, Wang H and Devenport W J, 2001, *The Surface Pressure Response of a NACA 0015 Airfoil Immersed In Grid Turbulence: Volume 2: Airfoil measurements,* Final report to NASA Langley under grant NAG 1-1942. *In preparation.*

Mydlarski L and Warhaft Z, 1996, *On the onset of high-Reynolds-number grid-generated wind tunnel turbulence*, Journal of Fluid Mechanics, vol. 320, pp. 331-368.

Paterson, Robert W. and Amiet, Roy K., *Acoustic Radiation and Surface Pressure Characteristics of an Airfoil Due to Incident Turbulence*, 3rd AIAA Aero-Acoustics Conference, July 20-23, 1976

Wittmer K. S., Devenport W. J. and Zsoldos J. S., 1998, *A four-sensor hot-wire probe system for three-component velocity measurement*, Experiments in Fluids, vol. 24, pp. 416.

Zsoldos J S, 1992, *An experimental investigation of interacting wing-tip vortex pairs*, MS Thesis, AOE Department, Virginia Tech.

FIGURES

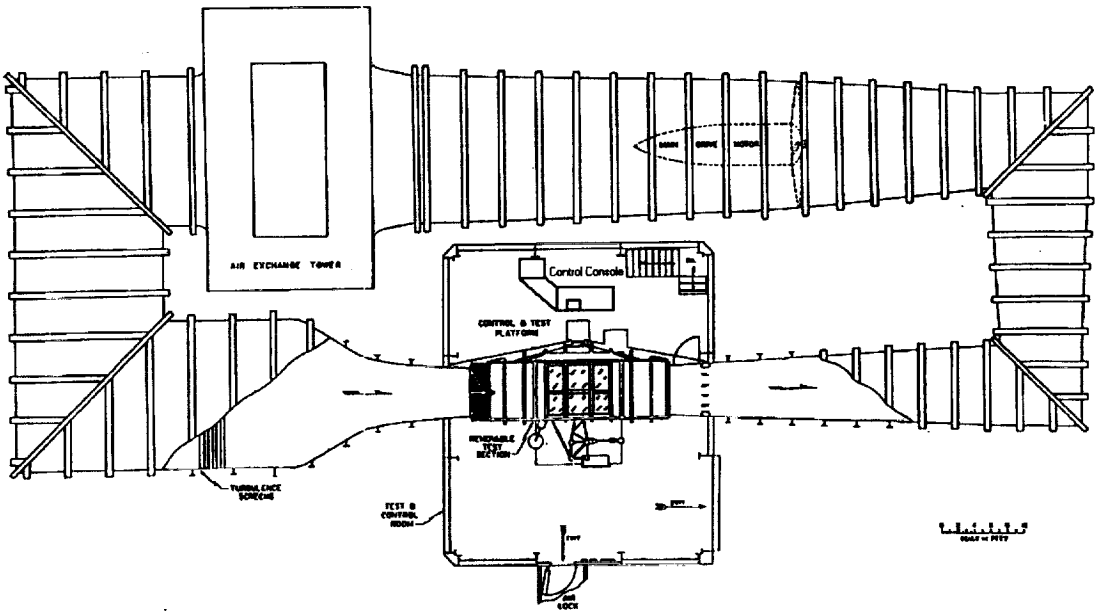

Figure 1. Layout of the Virginia Tech Stability Wind Tunnel.

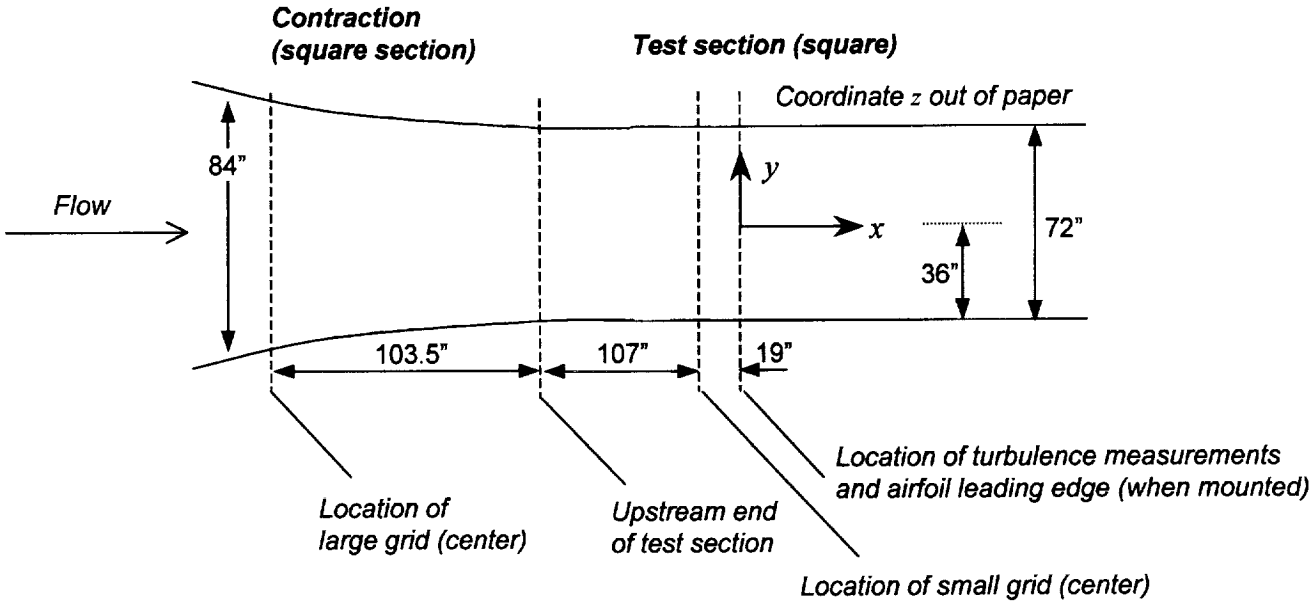

Figure 2. Side-view schematic of the Stability Wind Tunnel contraction and test section showing the mounting location of the two turbulence grids and the coordinate system.

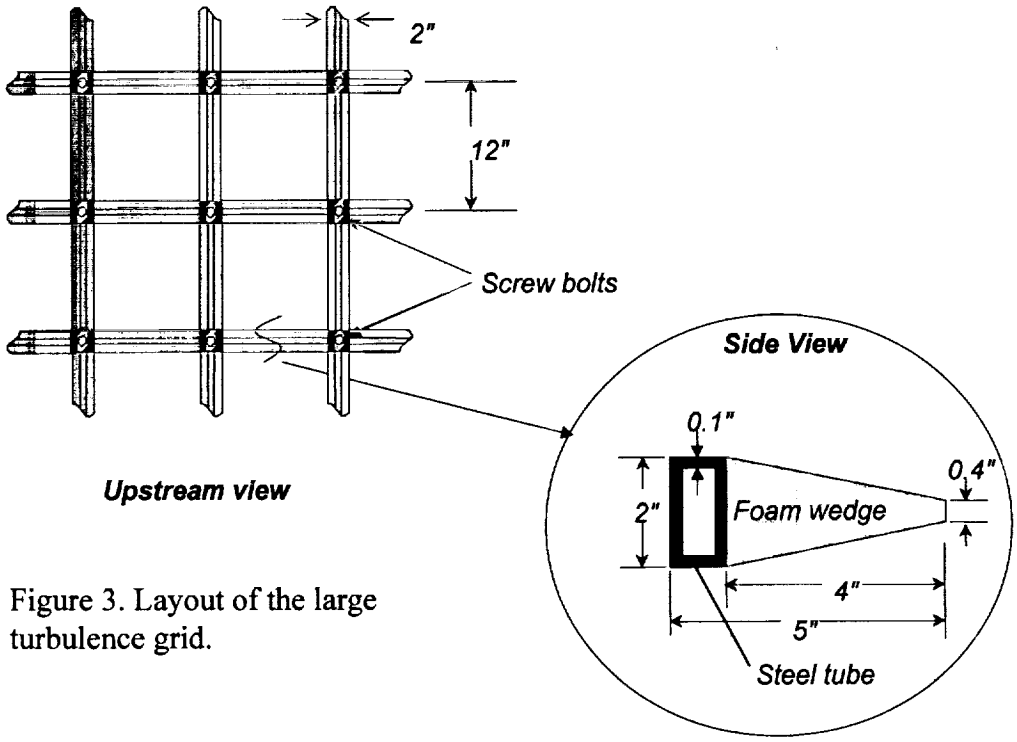

Figure 3. Layout of the large turbulence grid.

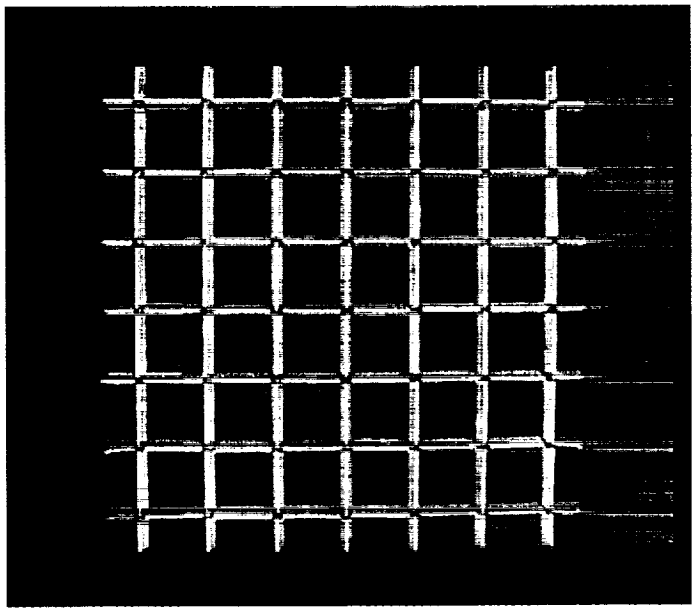

Figure 4. View of the large grid from downstream

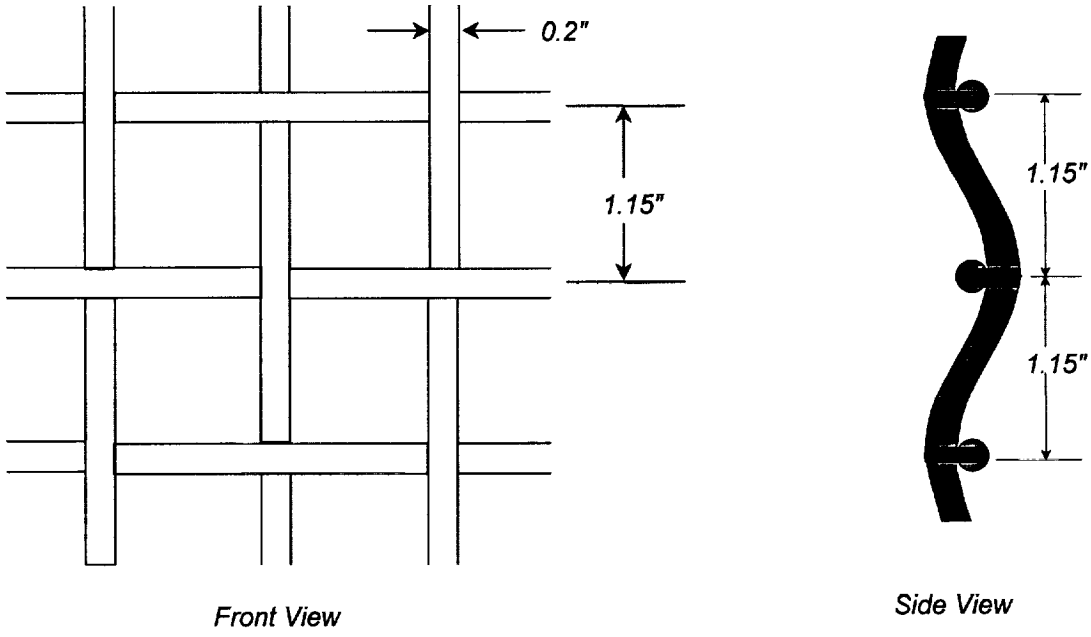

Figure 5. Detailed view of the weave of the small grid.

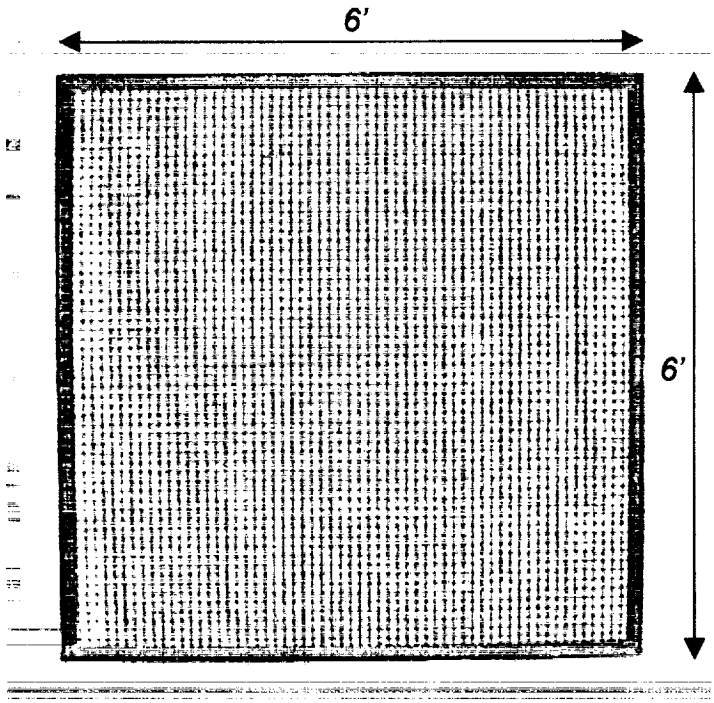

Figure 6. View of the small grid.

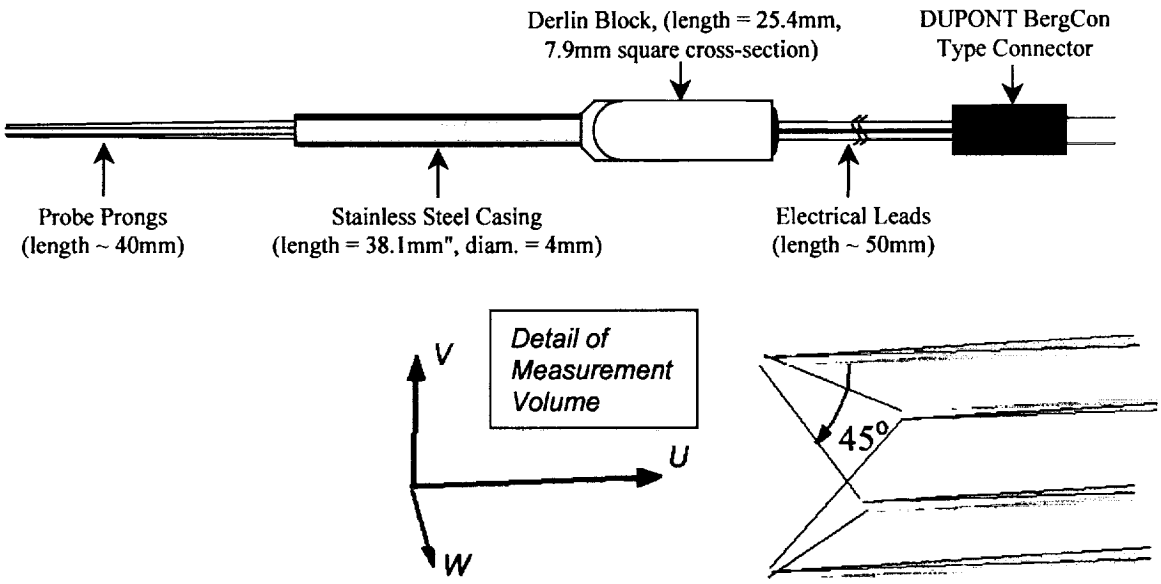

Figure 7. Auspex corporation AVOP-4-100 4-sensor 3-component hot-wire probe.

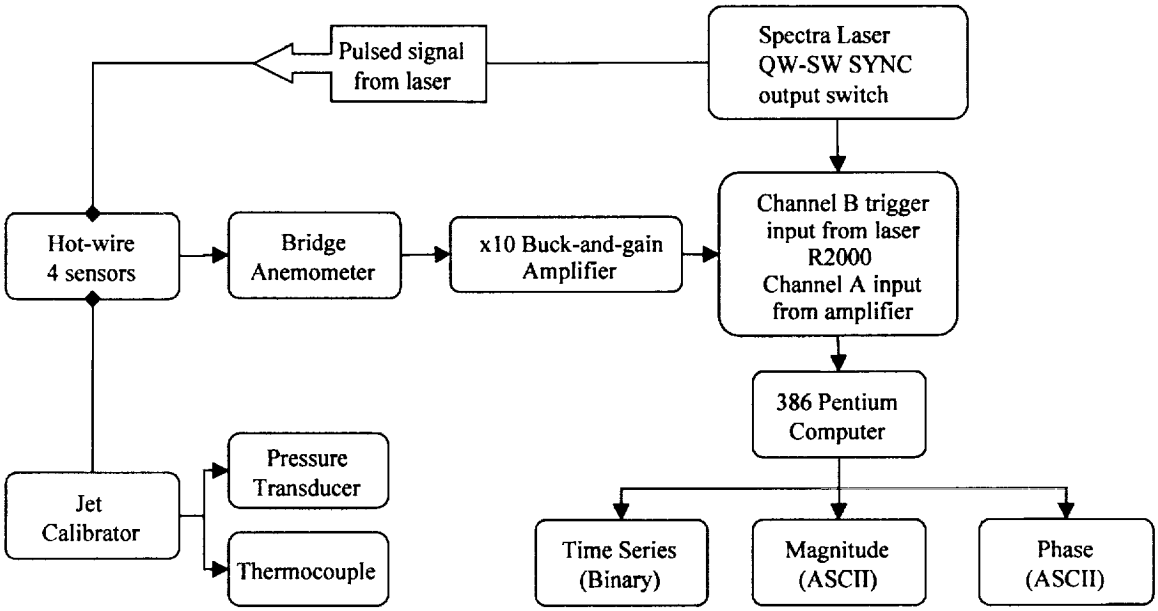

Figure 8. Schematic flow chart for the hot-wire frequency calibration

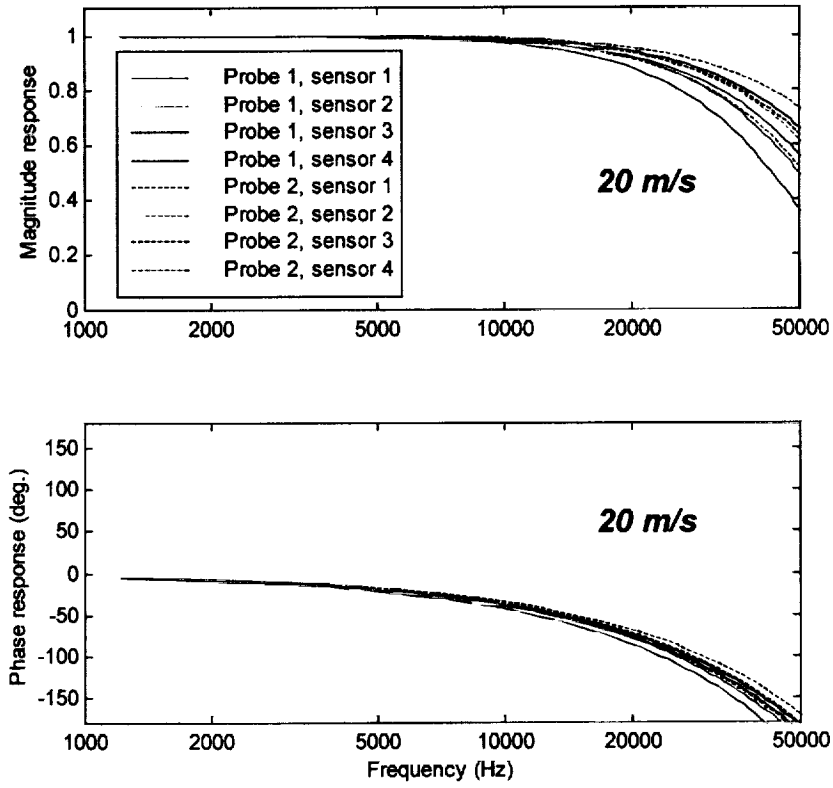

Figure 9. Magnitude and phase calibrations for the two hot wire probes at 20 and 40m/s.

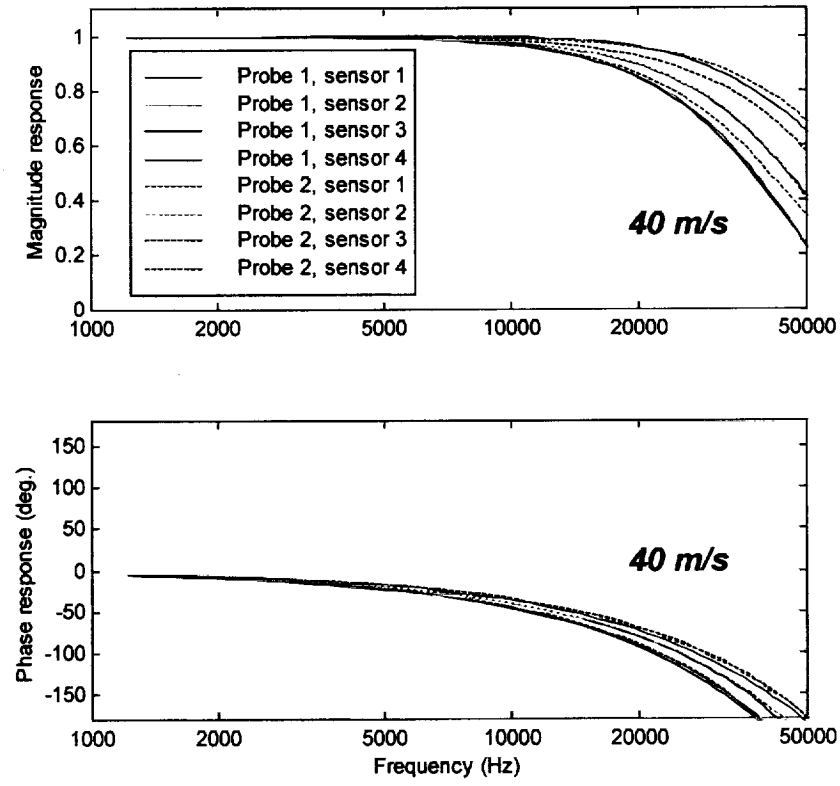

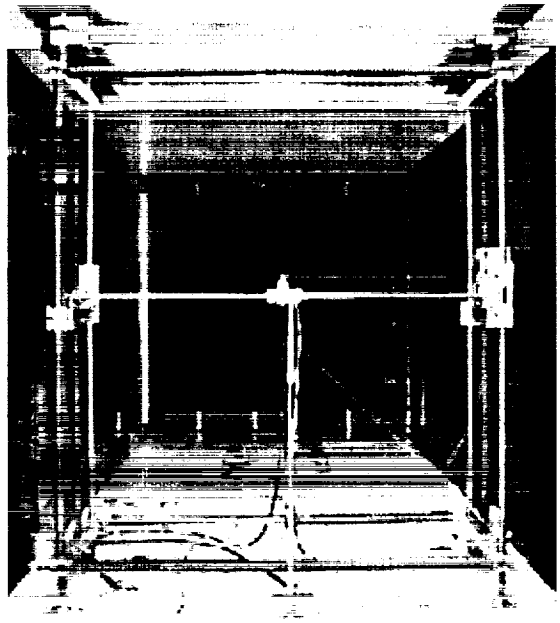

Figure 10. Wind-tunnel traverse viewed from upstream

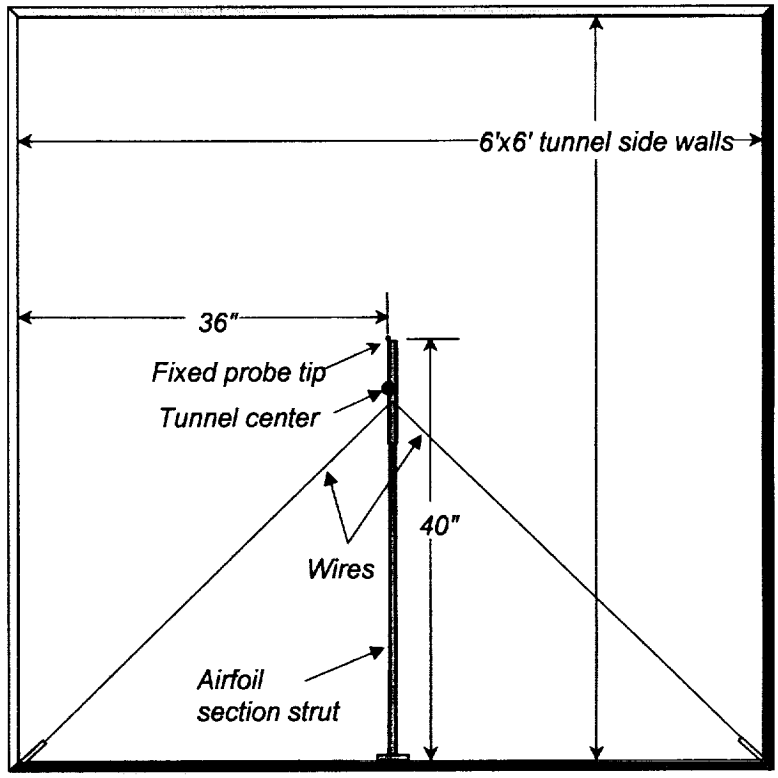

Figure 11. Schematic of the strut supporting the fixed probe for two-point velocity measurements.

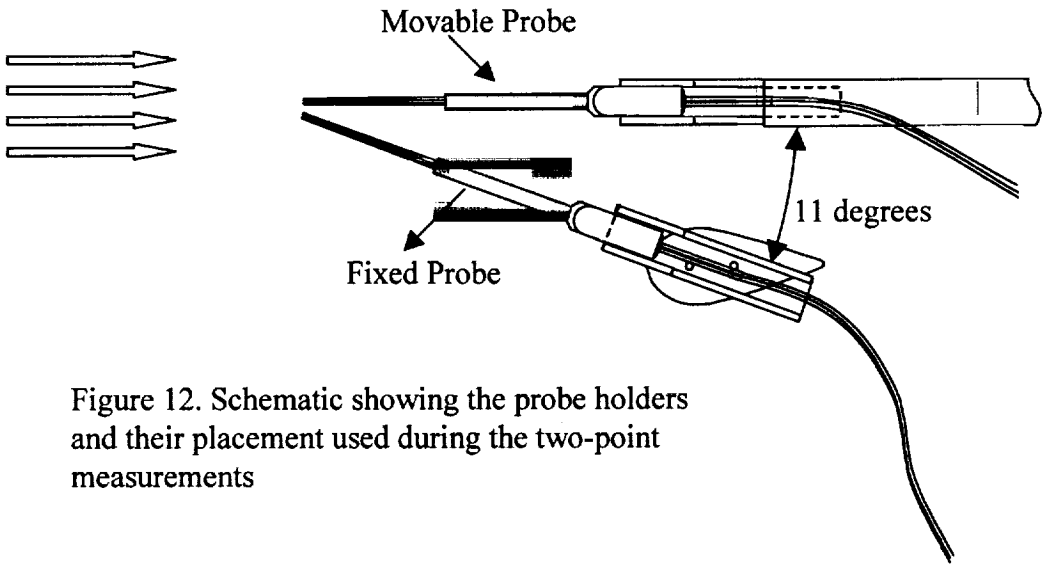

Figure 12. Schematic showing the probe holders and their placement used during the two-point measurements

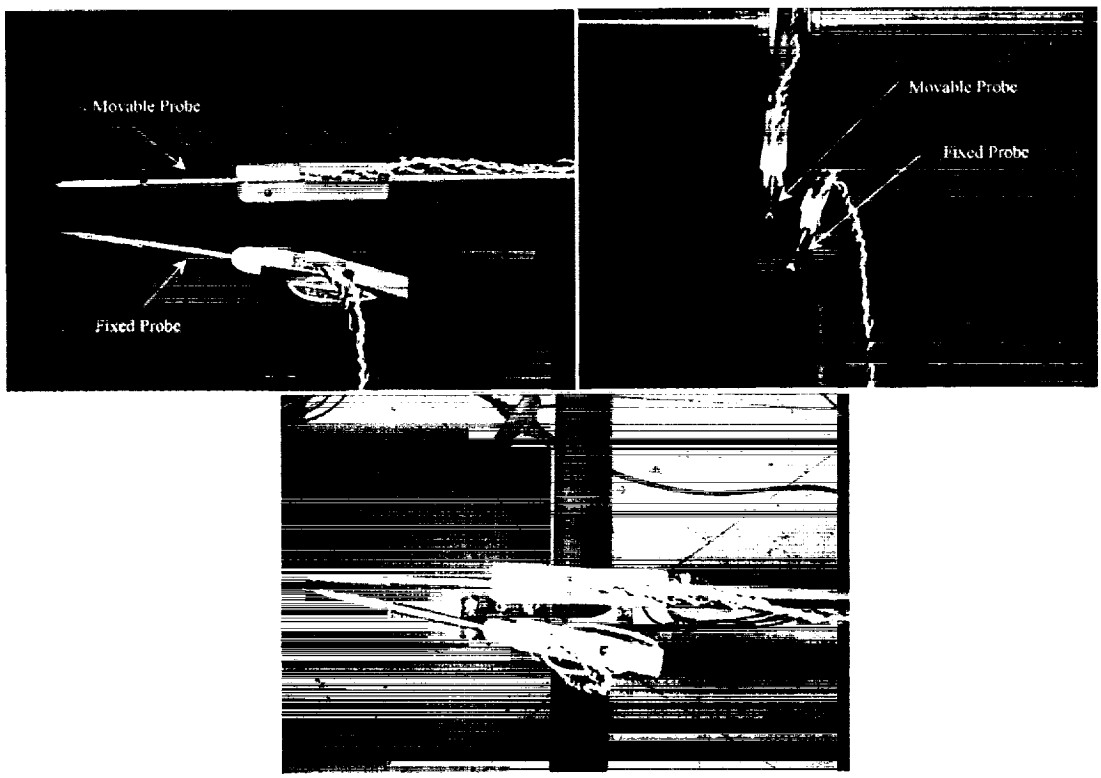

Figure 13. Photographs of the probes and holders used for the two-point measurements

(a) U/U_∞

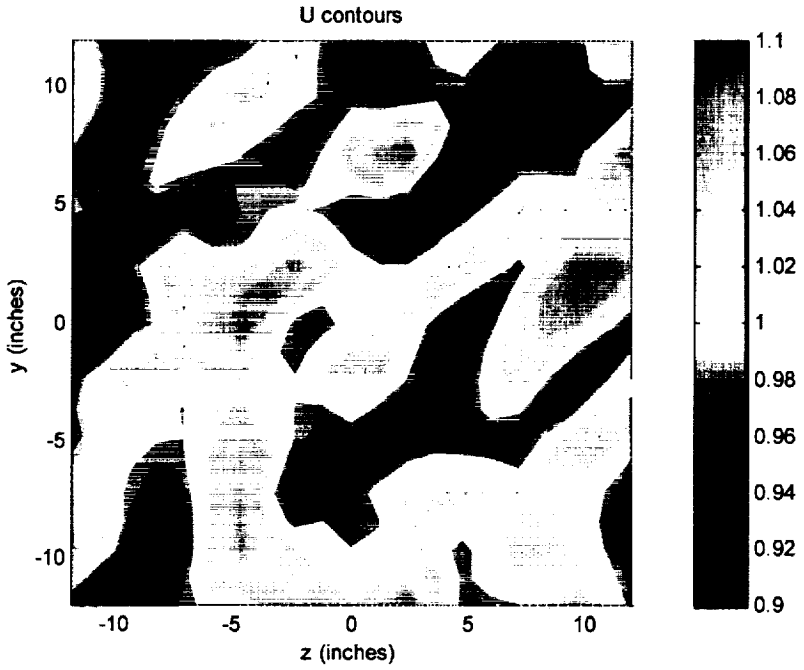

(b) Mean crossflow velocity vectors.

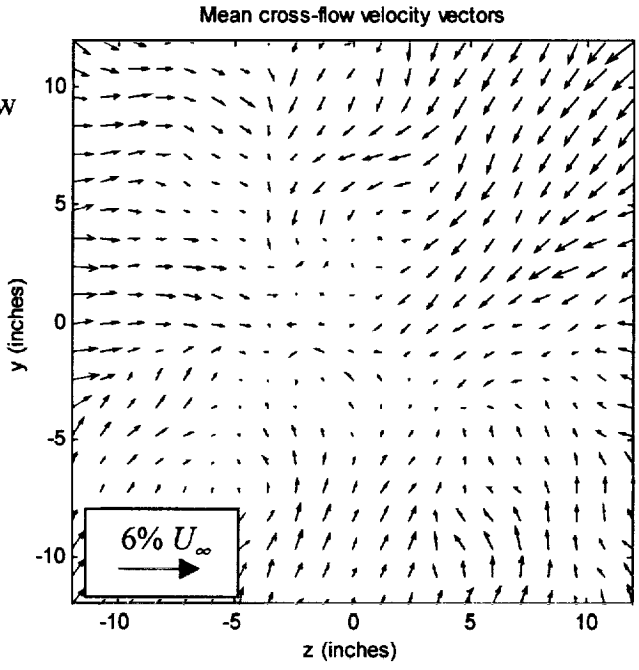

Figure 14. Flowfield downstream of the large grid at 10m/s.

(c) Contours of *u*-component turbulence normal stress normalized on U_∞^2

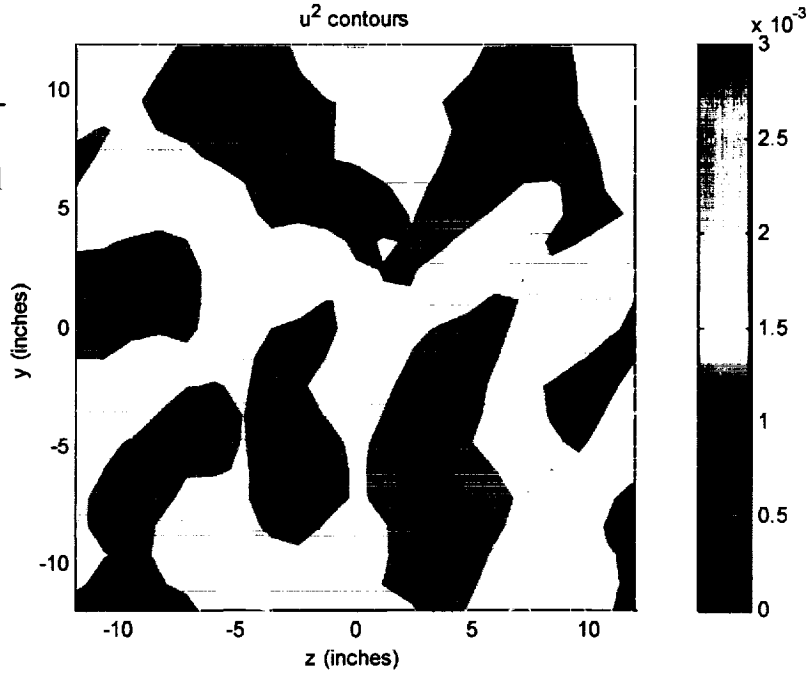

(d) Contours of *v*-component turbulence normal stress normalized on U_∞^2

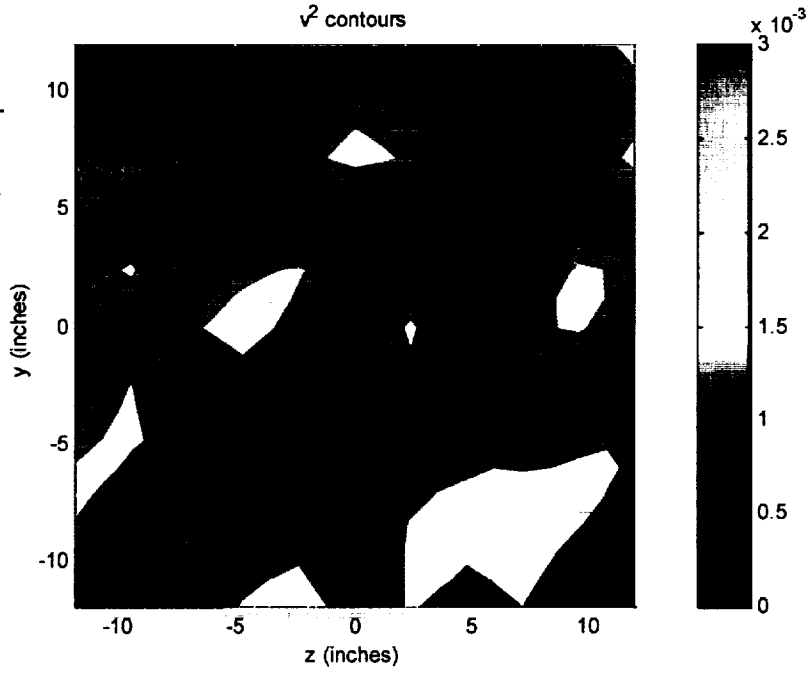

Figure 14. Flowfield downstream of the large grid at 10m/s.

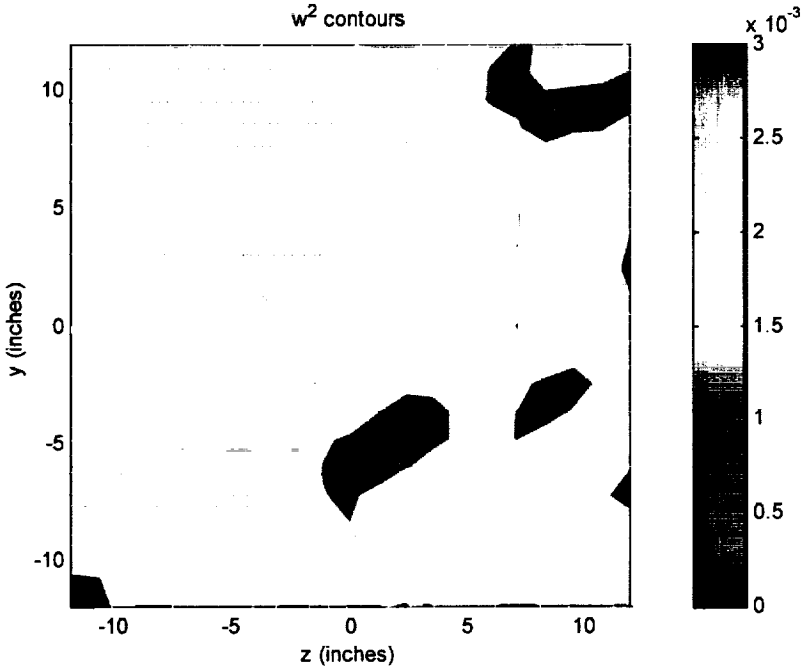

(e) Contours of w-component turbulence normal stress normalized on U_∞^2

Figure 14. Flowfield downstream of the large grid at 10m/s.

(a) U/U_∞

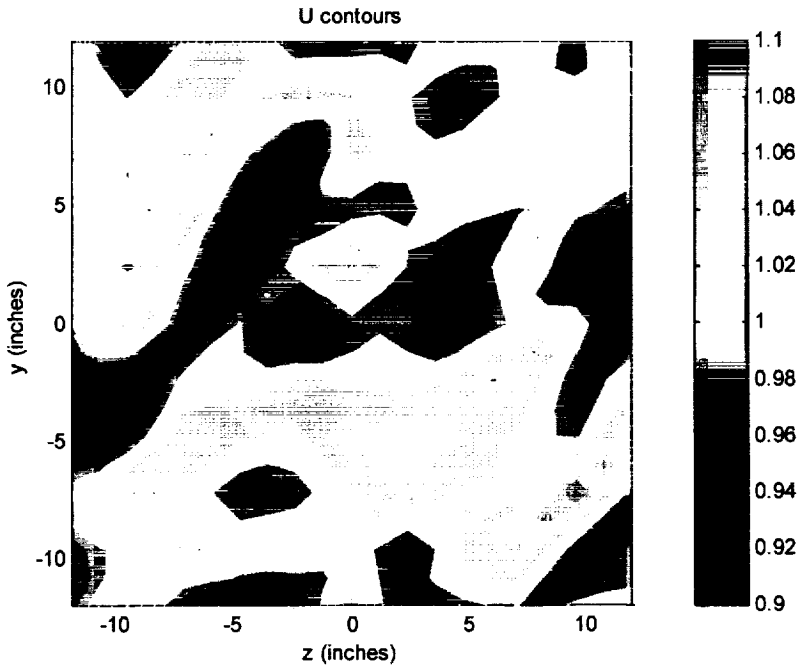

(b) Mean crossflow velocity vectors.

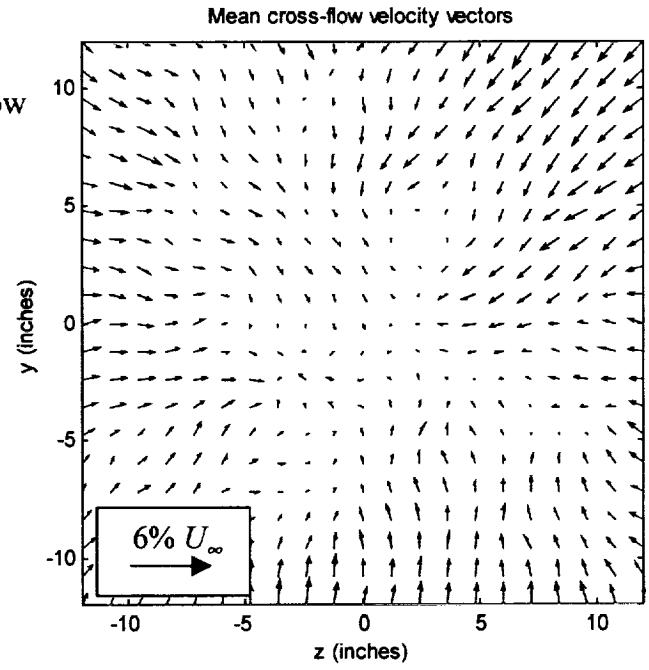

Figure 15. Flowfield downstream of the large grid at 20m/s.

(c) Contours of u-component turbulence normal stress normalized on U_∞^2

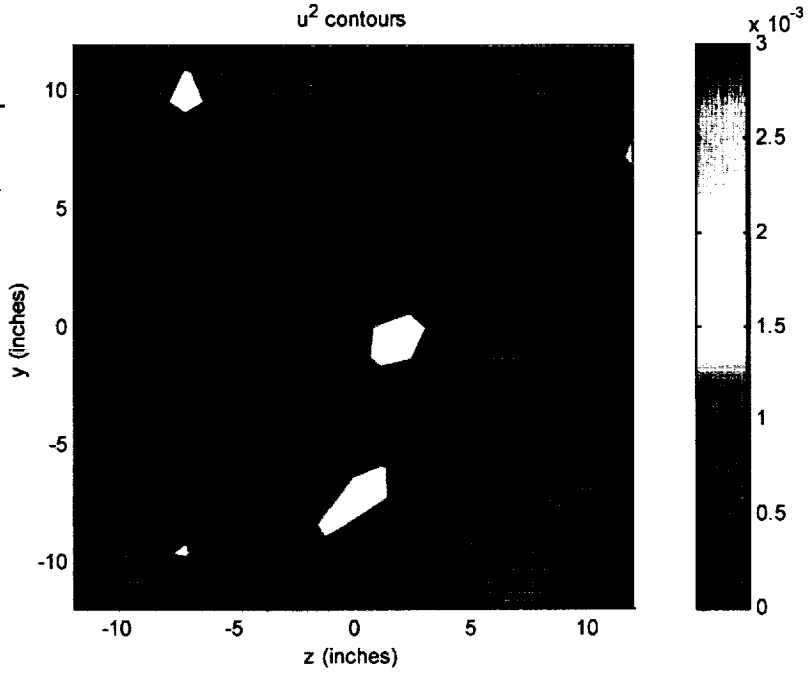

(d) Contours of v-component turbulence normal stress normalized on U_∞^2

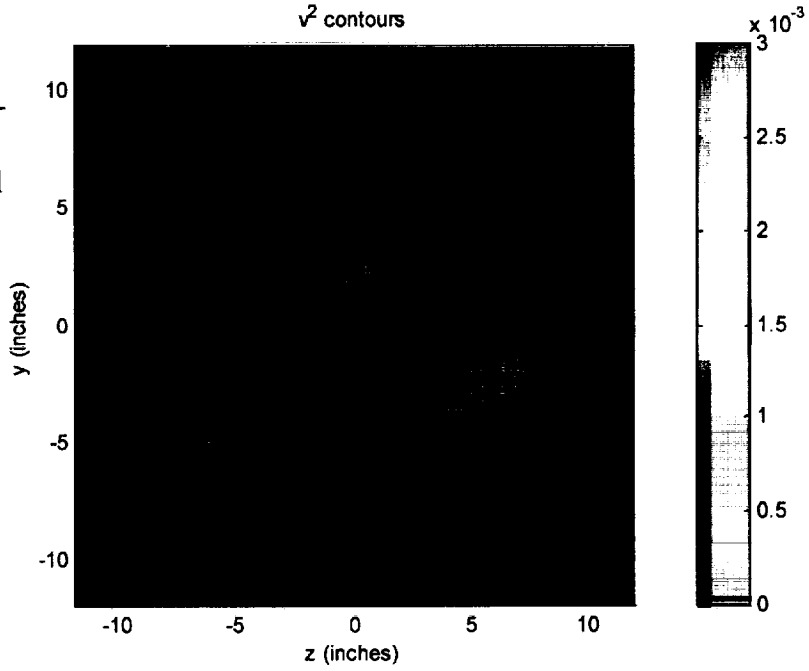

Figure 15. Flowfield downstream of the large grid at 20m/s.

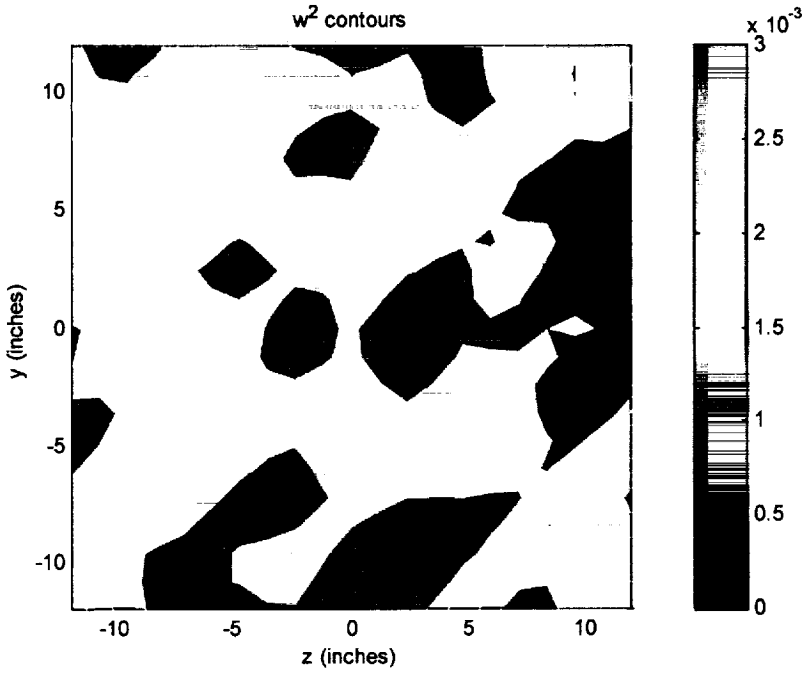

(e) Contours of w-component turbulence normal stress normalized on U_∞^2

Figure 15. Flowfield downstream of the large grid at 20m/s.

(a) U/U_∞

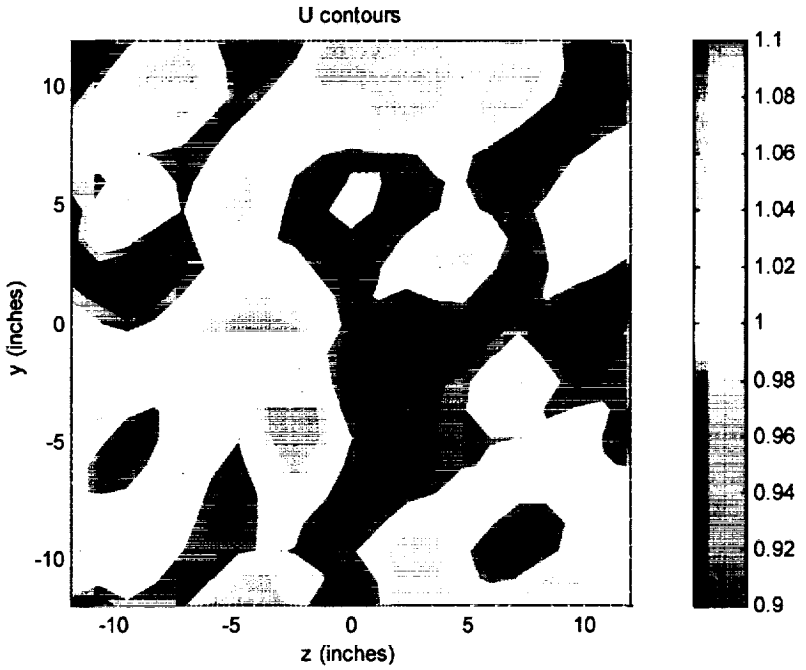

(b) Mean crossflow velocity vectors.

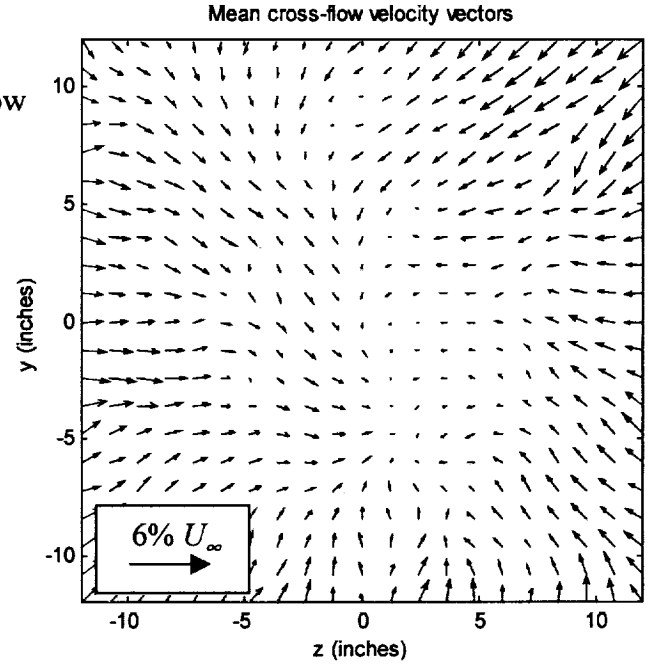

Figure 16. Flowfield downstream of the large grid at 30m/s.

(c) Contours of *u*-component turbulence normal stress normalized on U_∞^2

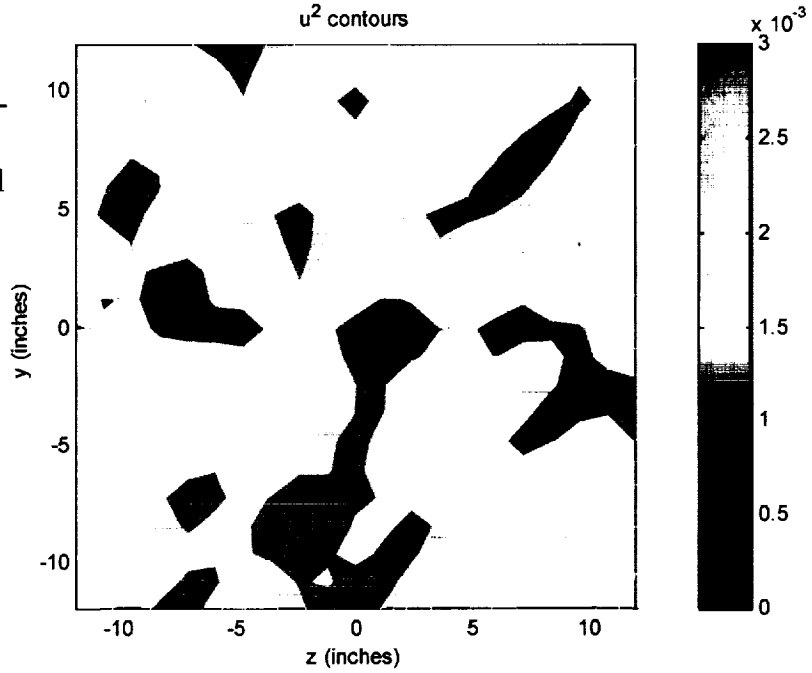

(d) Contours of *v*-component turbulence normal stress normalized on U_∞^2

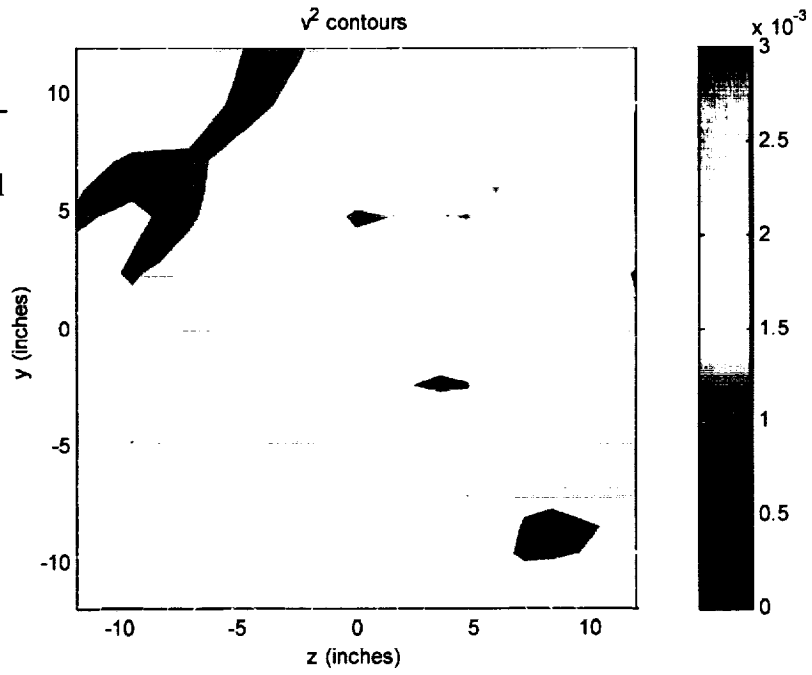

Figure 16. Flowfield downstream of the large grid at 30m/s.

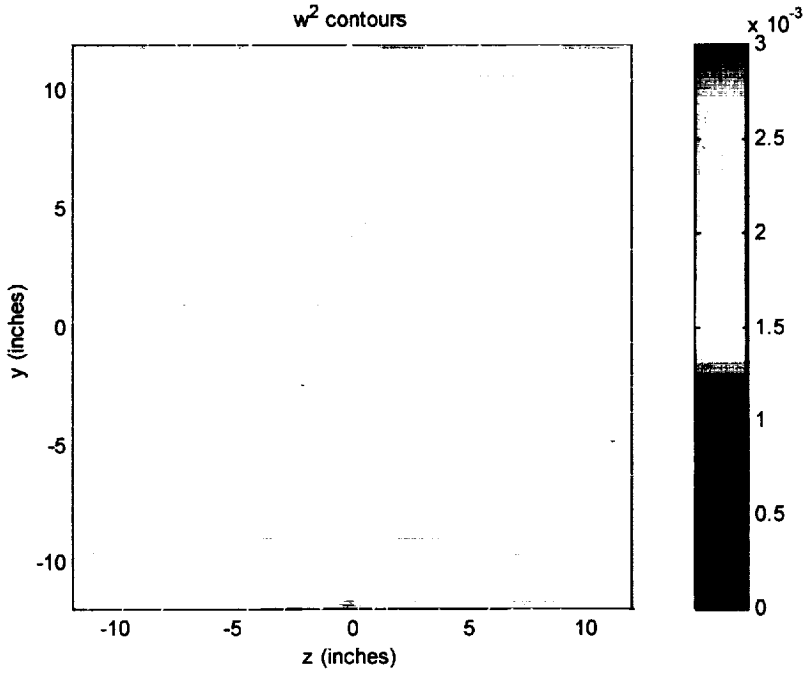

(e) Contours of w-component turbulence normal stress normalized on U_∞^2

Figure 16. Flowfield downstream of the large grid at 30m/s.

(a) U/U_∞

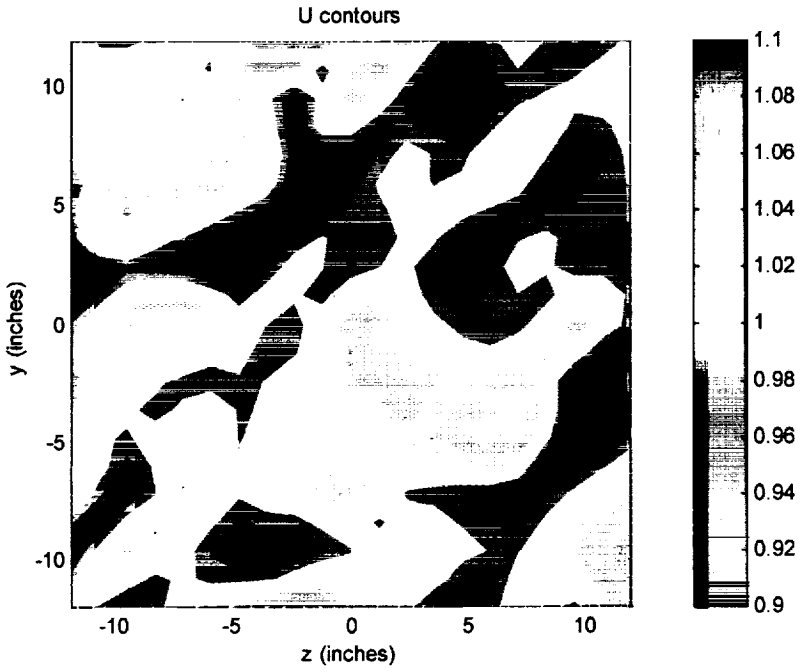

(b) Mean crossflow velocity vectors.

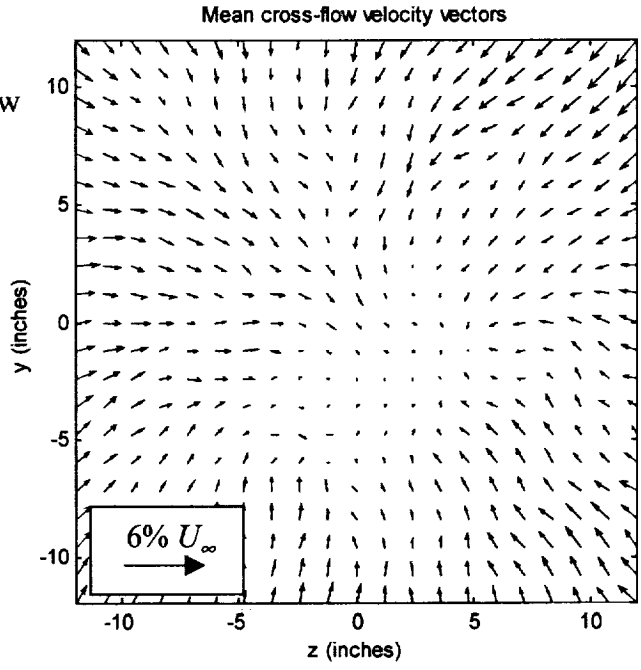

Figure 17. Flowfield downstream of the large grid at 40m/s.

(c) Contours of u-component turbulence normal stress normalized on U_∞^2

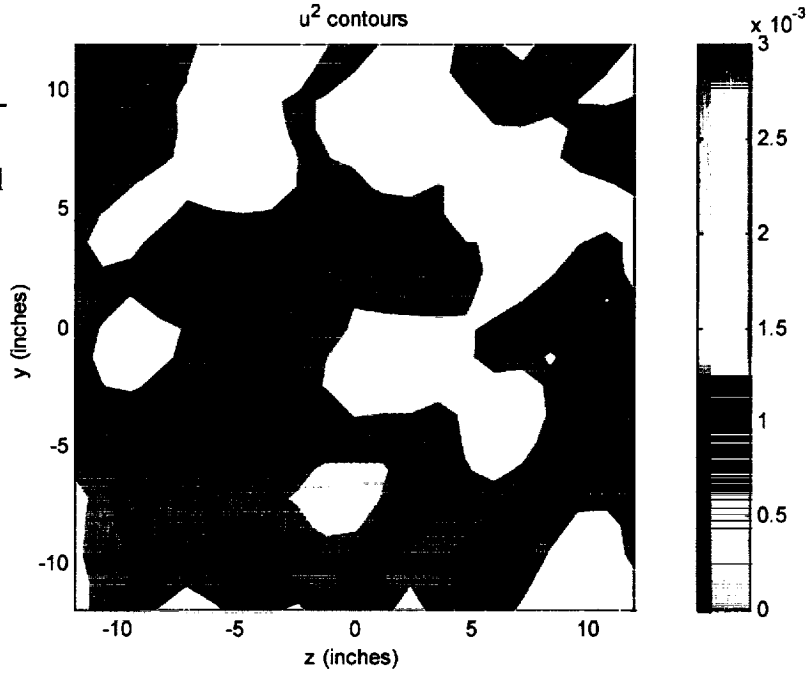

(d) Contours of v-component turbulence normal stress normalized on U_∞^2

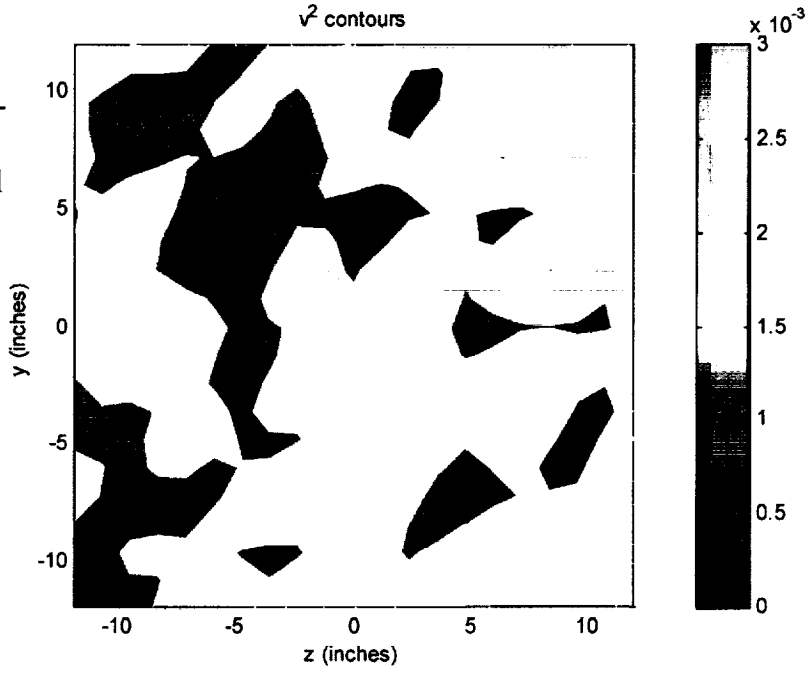

Figure 17. Flowfield downstream of the large grid at 40m/s.

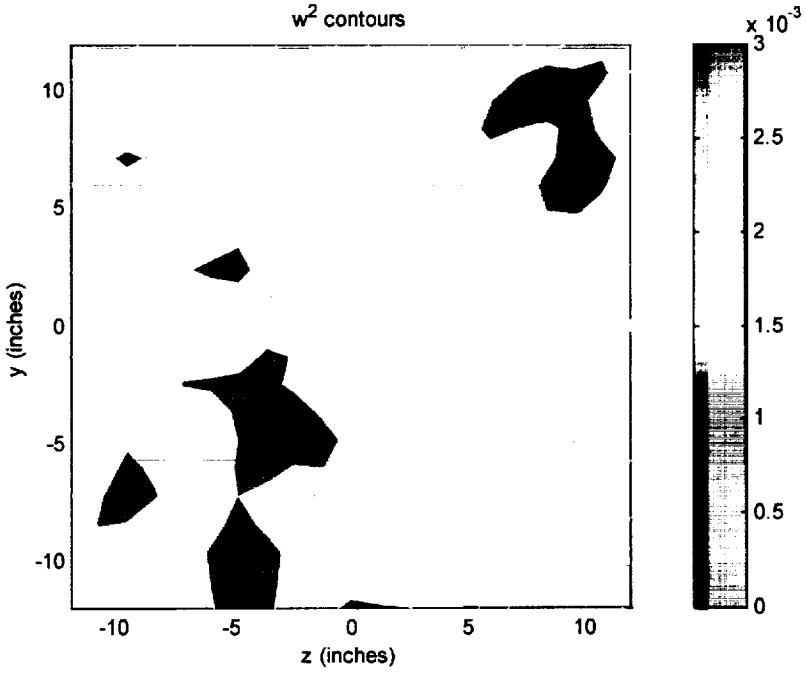

(e) Contours of w-component turbulence normal stress normalized on U_∞^2

Figure 17. Flowfield downstream of the large grid at 40m/s.

(a) U/U_∞

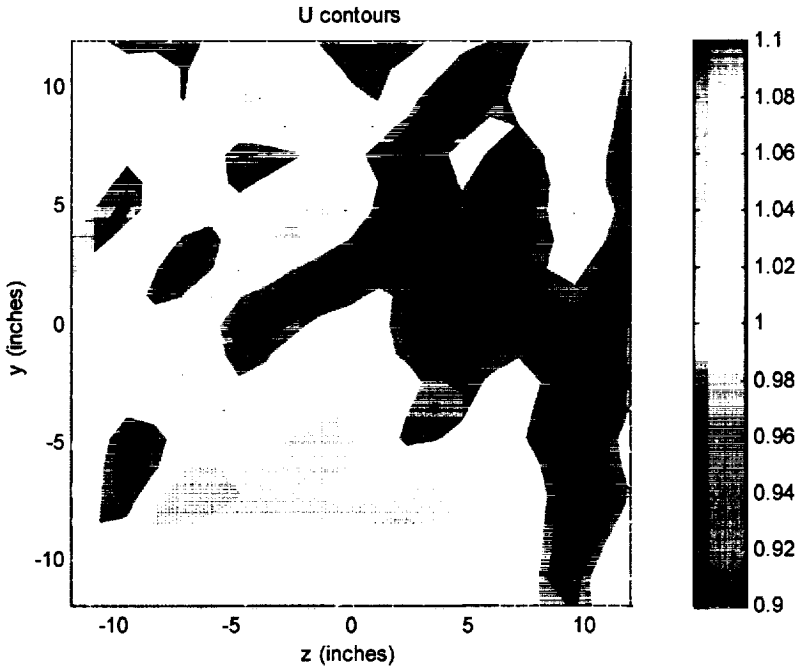

(b) Mean crossflow velocity vectors.

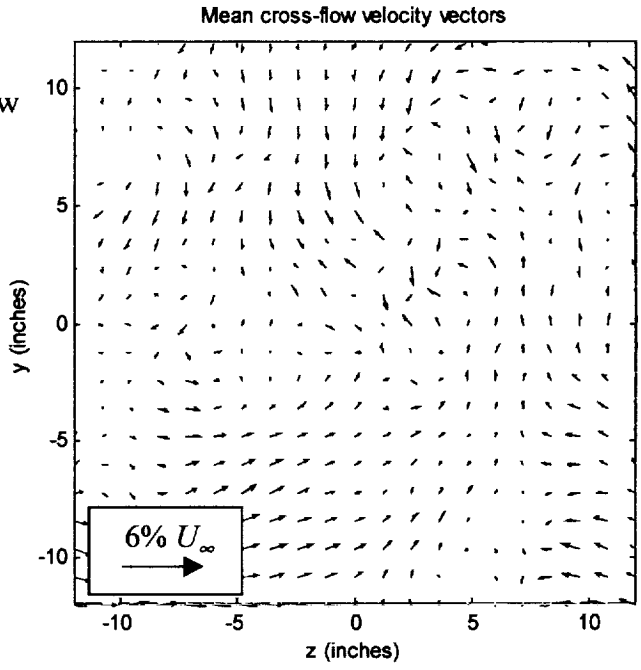

Figure 18. Flowfield downstream of the small grid at 10m/s.

(c) Contours of u-component turbulence normal stress normalized on U_∞^2

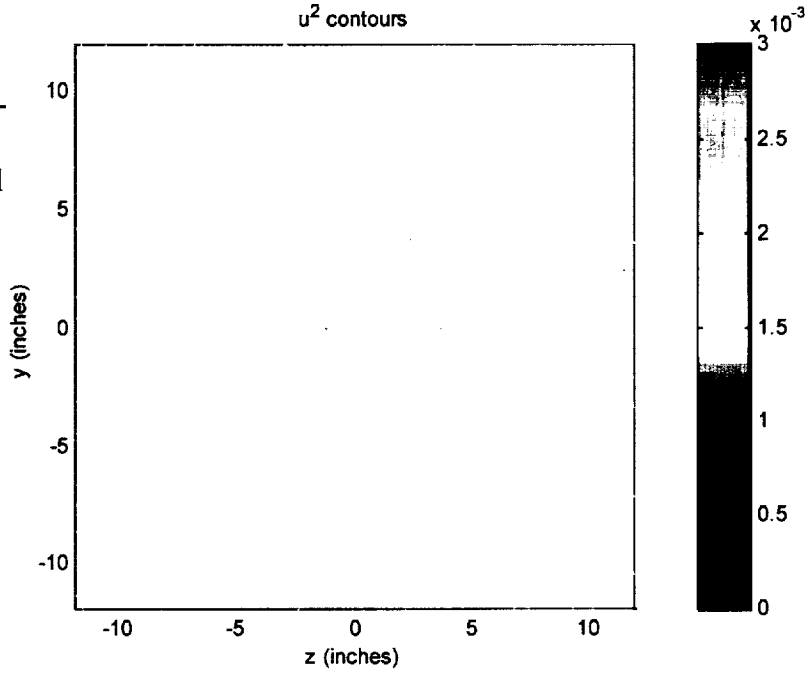

(d) Contours of v-component turbulence normal stress normalized on U_∞^2

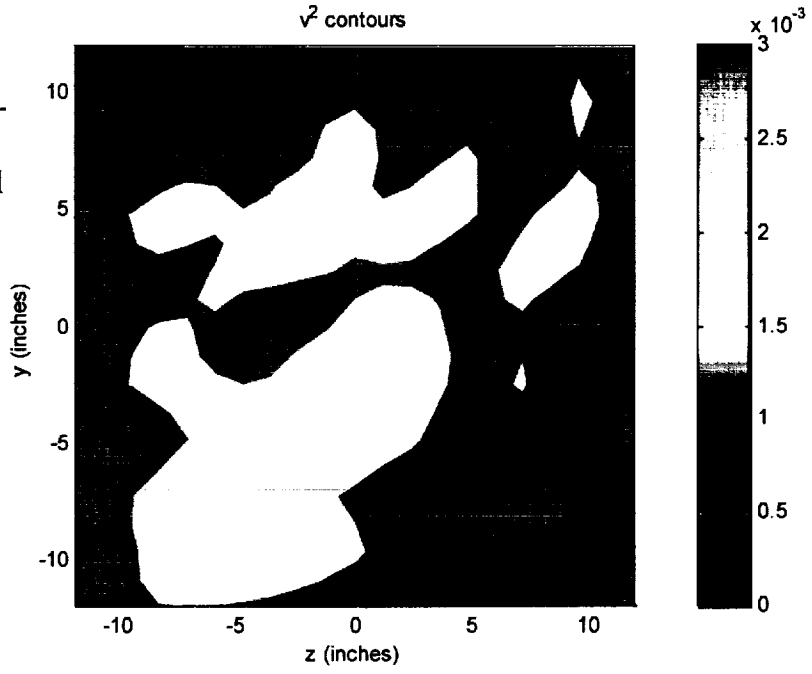

Figure 18. Flowfield downstream of the small grid at 10m/s.

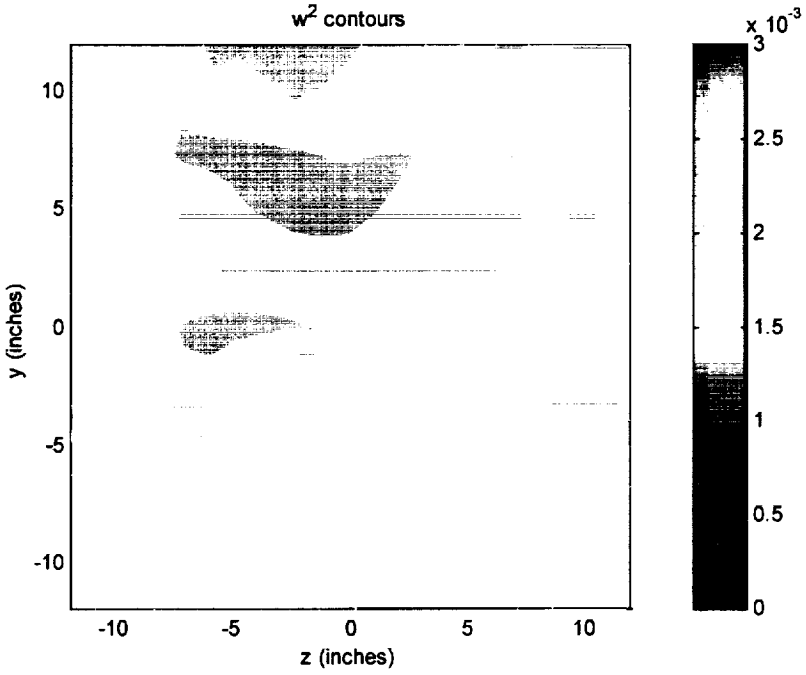

(e) Contours of w-component turbulence normal stress normalized on U_∞^2

Figure 18. Flowfield downstream of the small grid at 10m/s.

(a) U/U_∞

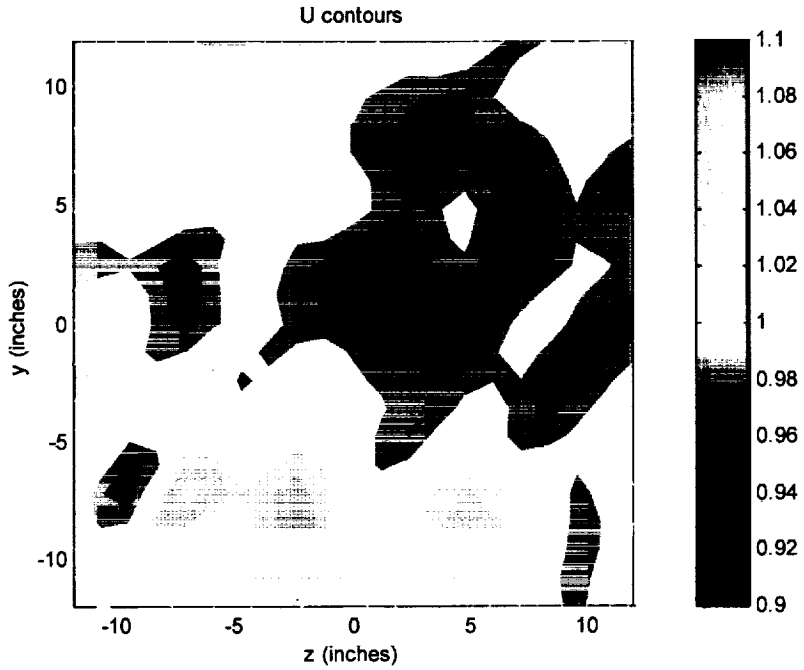

(b) Mean crossflow velocity vectors.

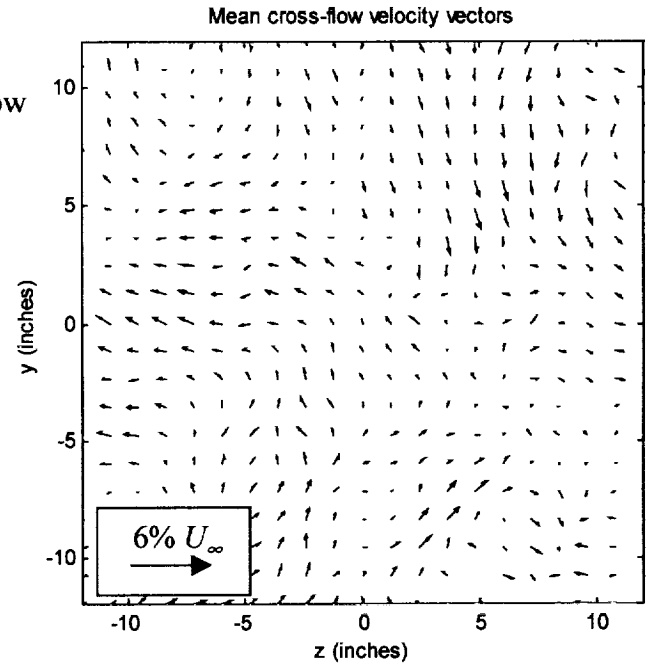

Figure 19. Flowfield downstream of the small grid at 20m/s.

(c) Contours of u-component turbulence normal stress normalized on U_∞^2

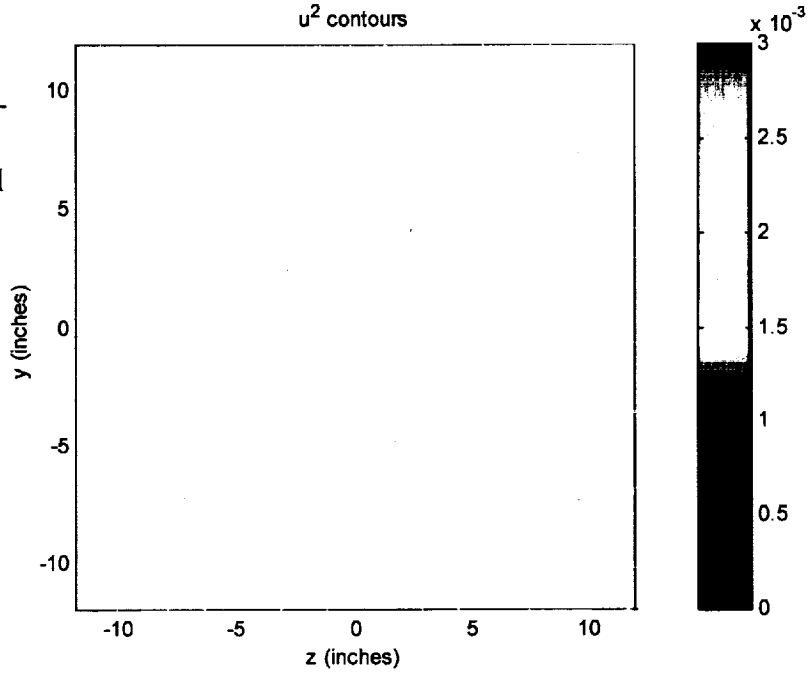

(d) Contours of v-component turbulence normal stress normalized on U_∞^2

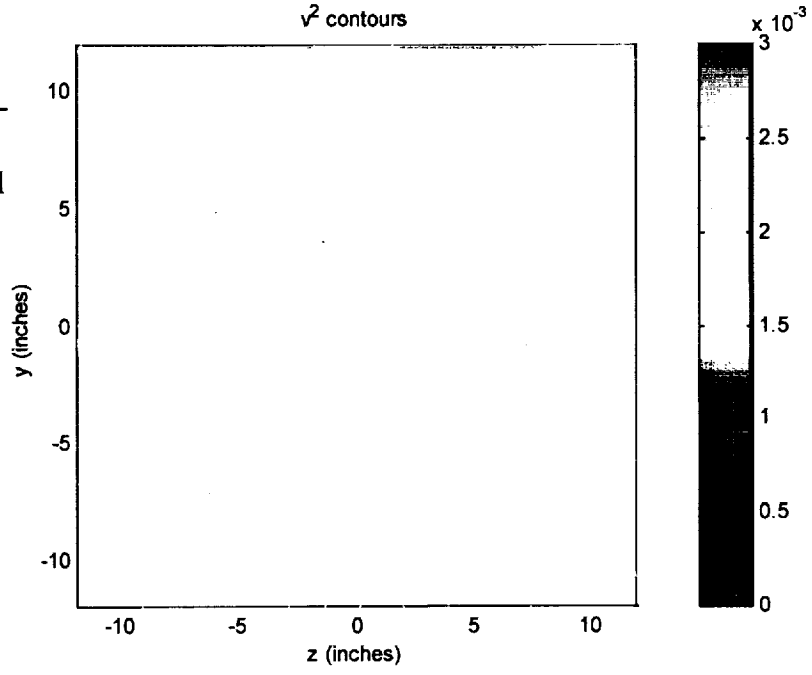

Figure 19. Flowfield downstream of the small grid at 20m/s.

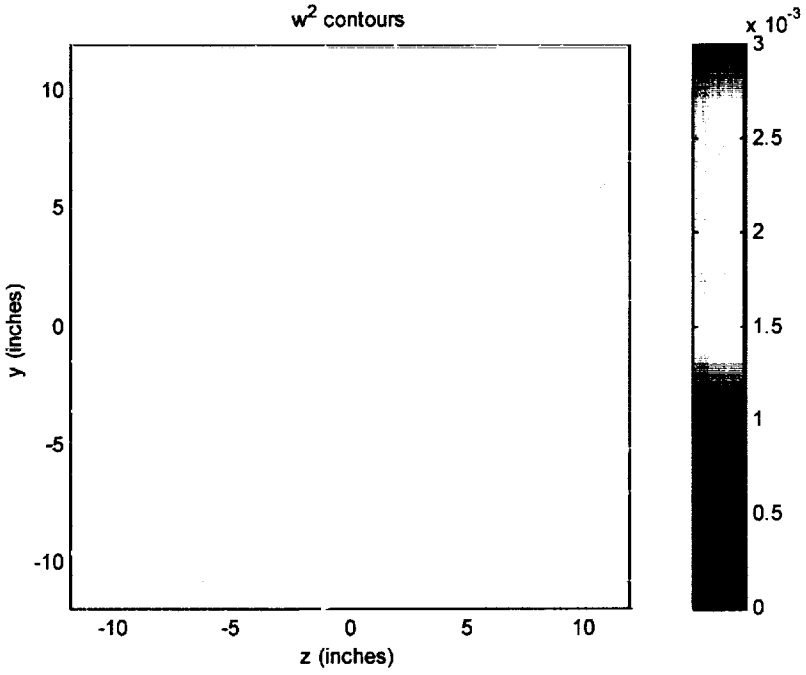

(e) Contours of *w*-component turbulence normal stress normalized on U_∞^2

Figure 19. Flowfield downstream of the small grid at 20m/s.

(a) U/U_∞

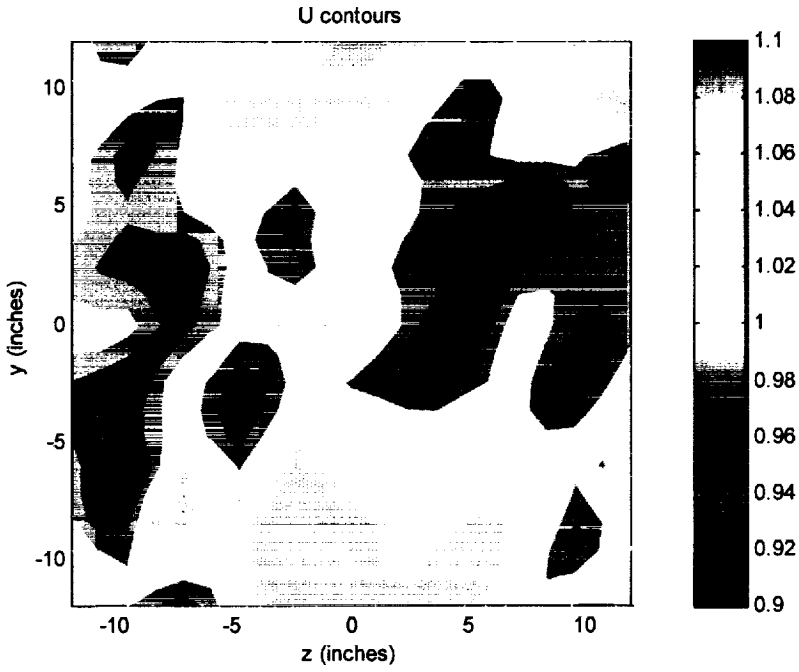

(b) Mean crossflow velocity vectors.

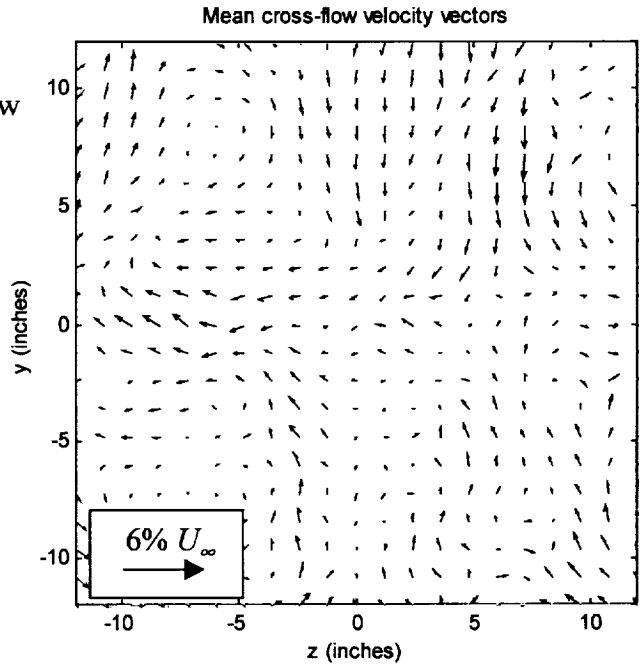

Figure 20. Flowfield downstream of the small grid at 30m/s.

(c) Contours of u-component turbulence normal stress normalized on U_∞^2

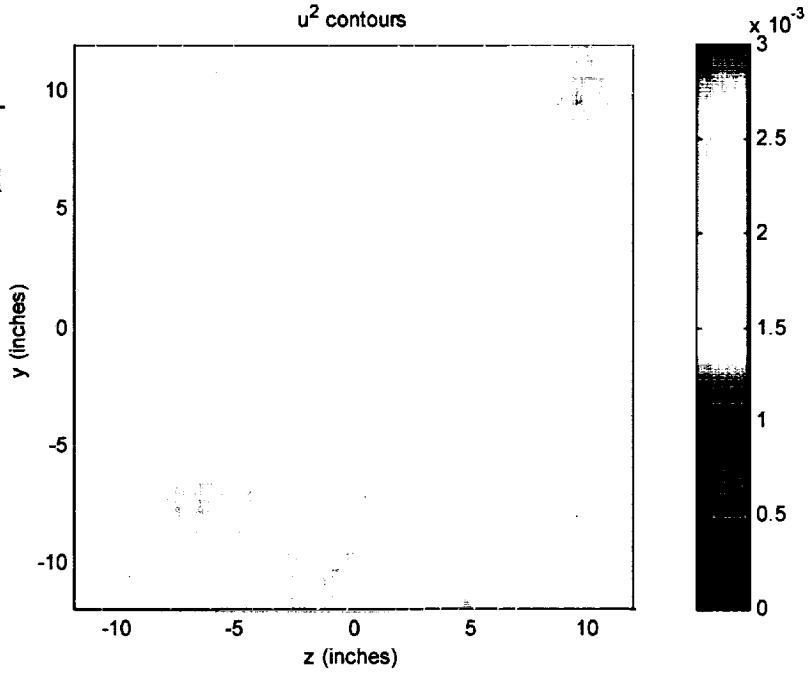

(d) Contours of v-component turbulence normal stress normalized on U_∞^2

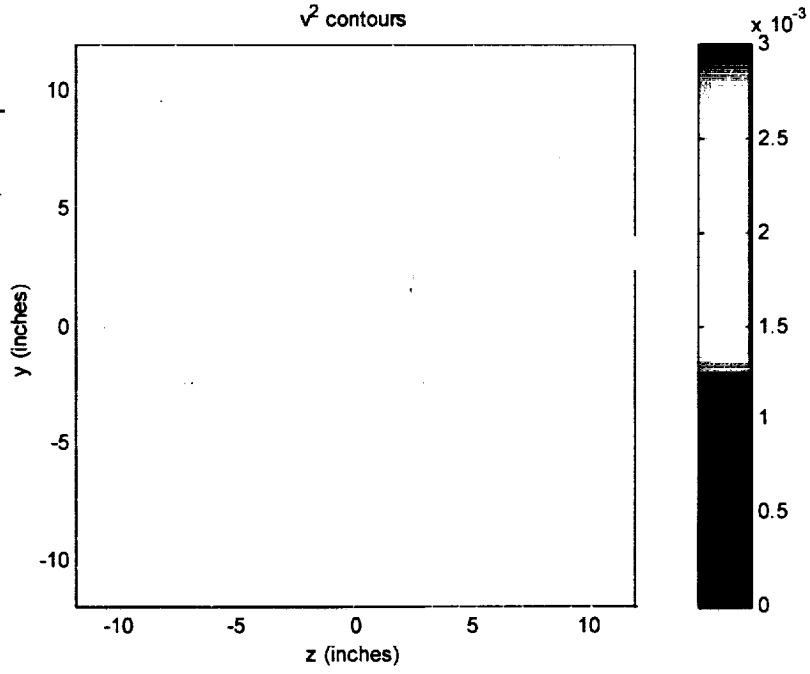

Figure 20. Flowfield downstream of the small grid at 30m/s.

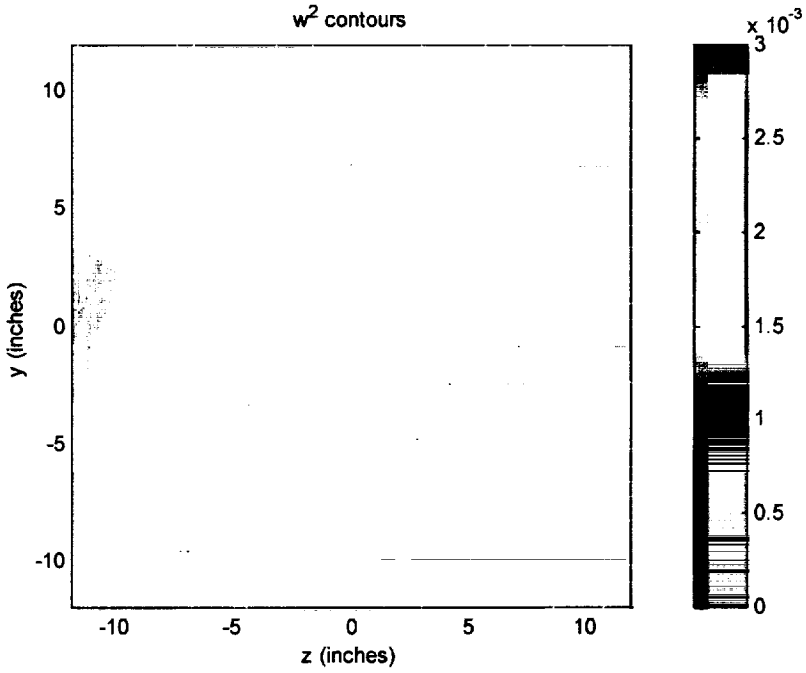

(e) Contours of w-component turbulence normal stress normalized on U_∞^2

Figure 20. Flowfield downstream of the large grid at 30m/s.

(a) U/U_∞

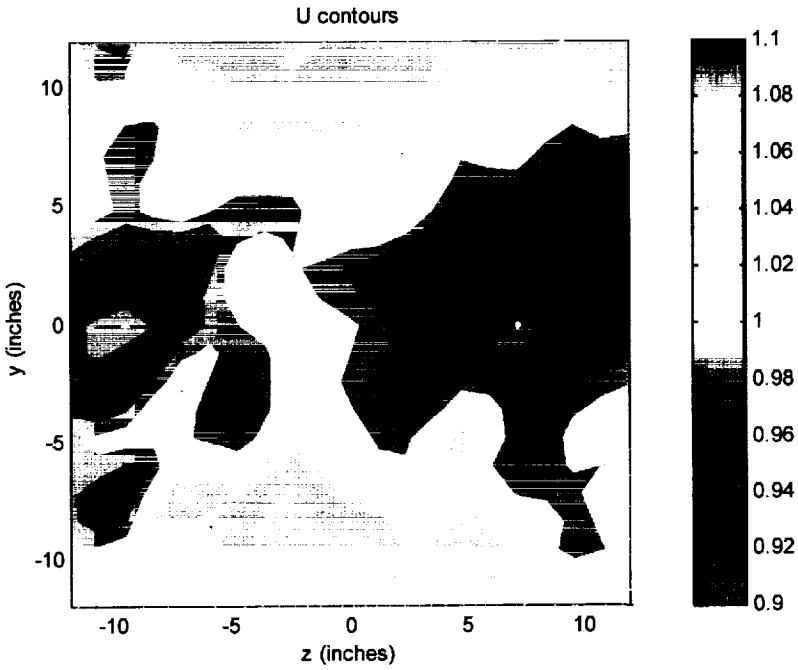

(b) Mean crossflow velocity vectors.

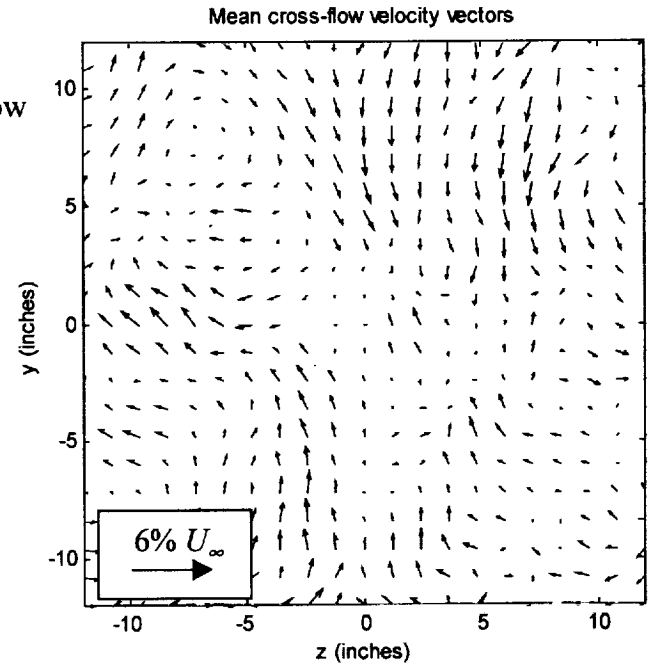

Figure 21. Flowfield downstream of the small grid at 40m/s.

(c) Contours of u-component turbulence normal stress normalized on U_∞^2

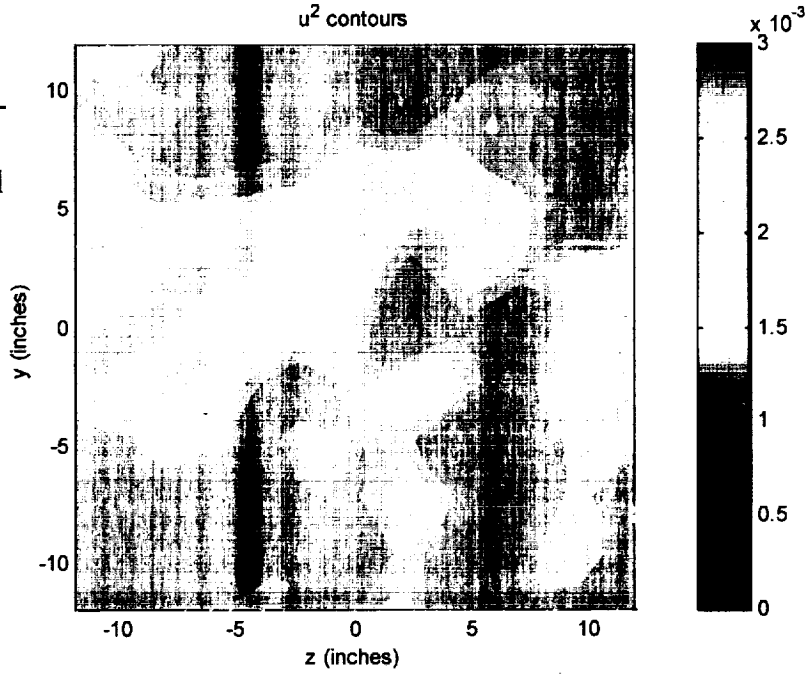

(d) Contours of v-component turbulence normal stress normalized on U_∞^2

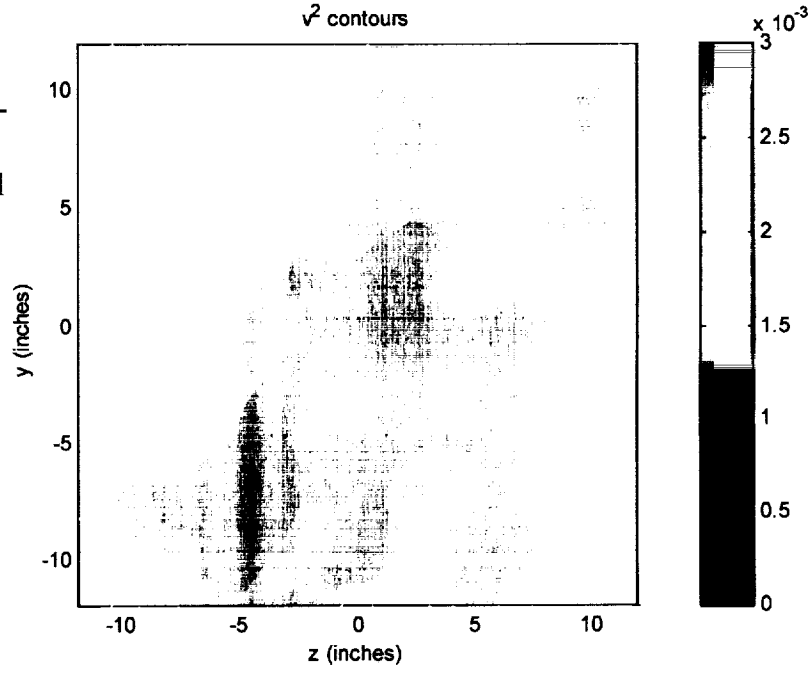

Figure 21. Flowfield downstream of the small grid at 40m/s.

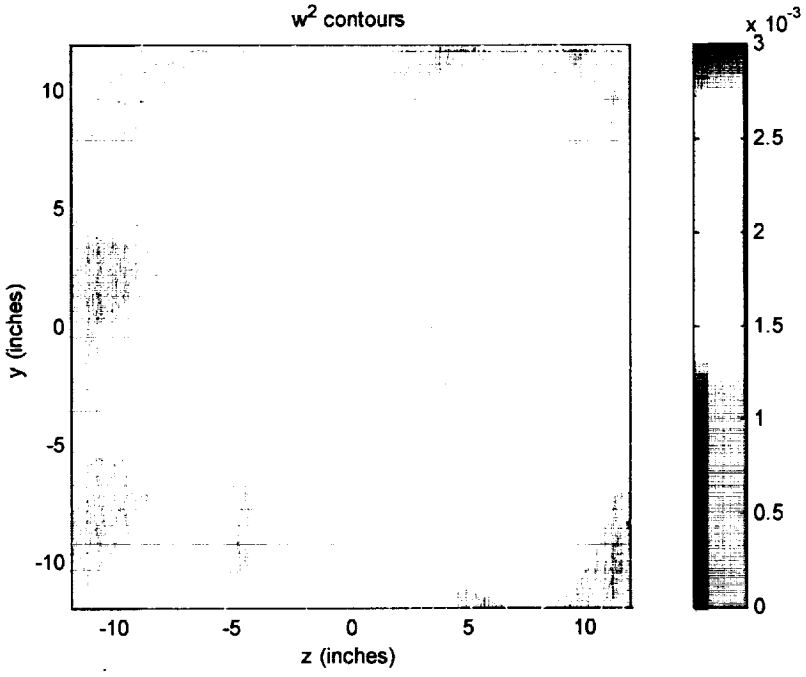

(e) Contours of w-component turbulence normal stress normalized on U_∞^2

Figure 21. Flowfield downstream of the small grid at 40m/s.

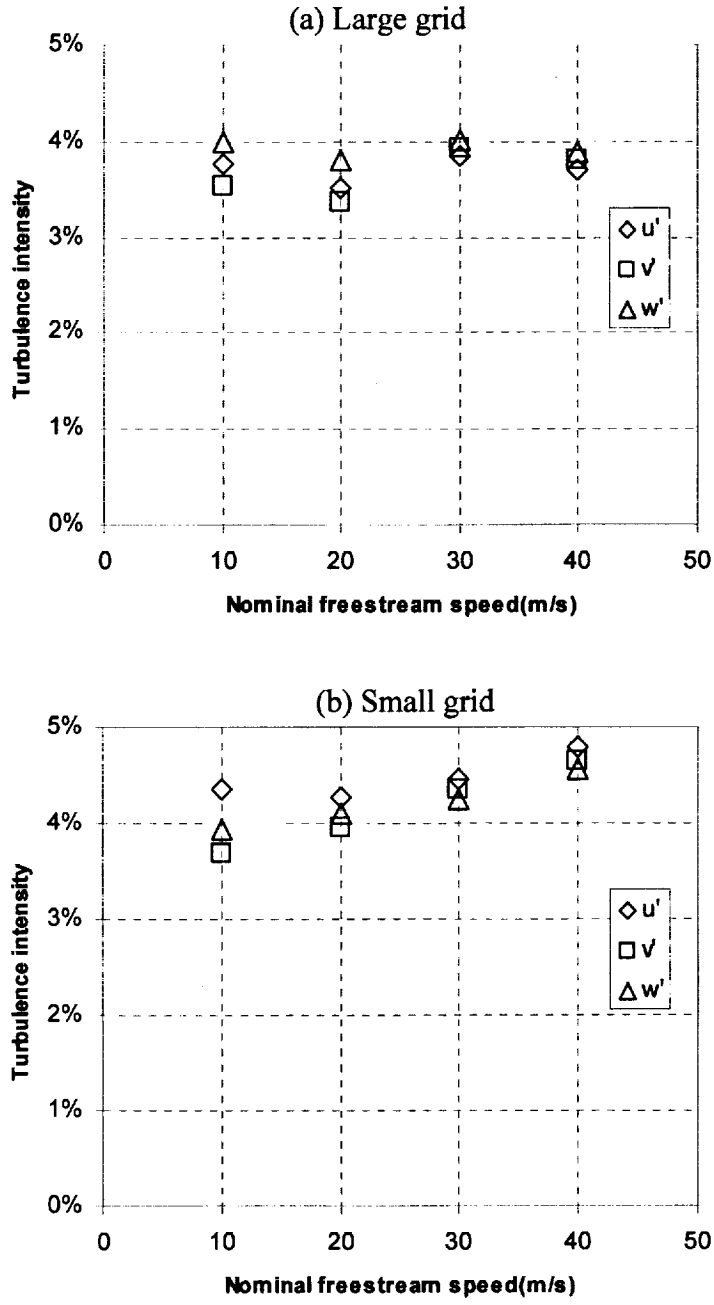

Figure 22. Cross-sectional average turbulence intensities..

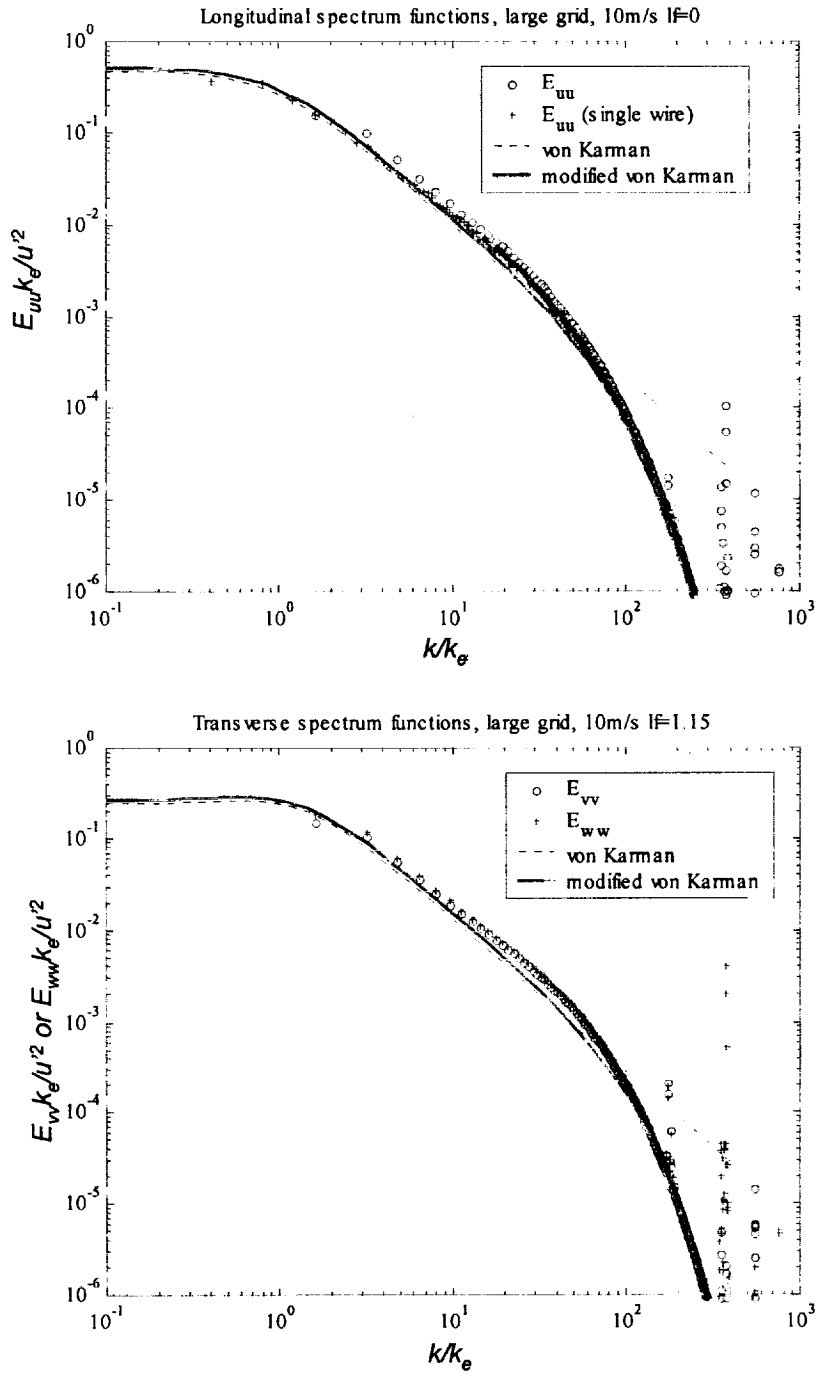

Figure 23. Wavenumber spectra measured with the large grid at 10m/s.

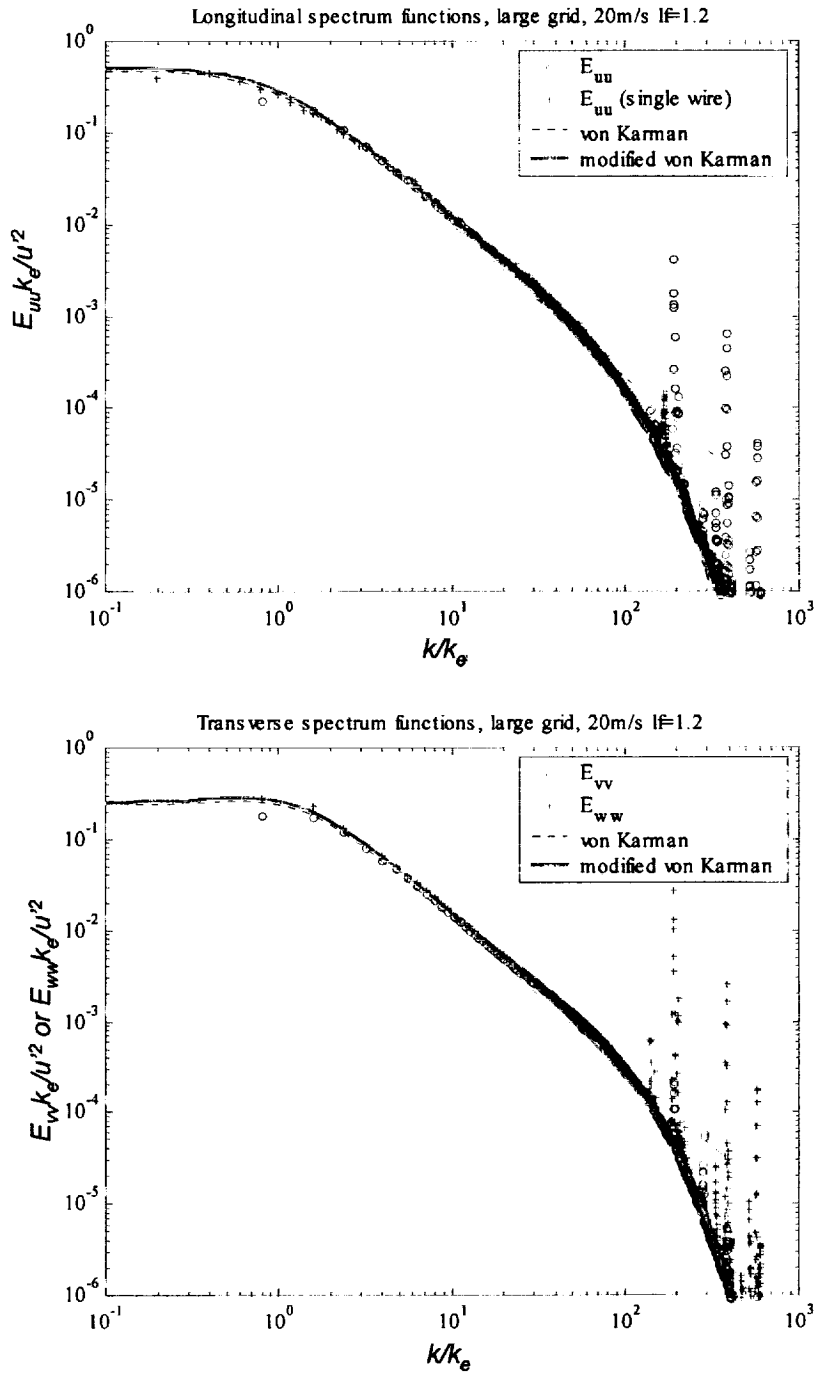

Figure 24. Wavenumber spectra measured with the large grid at 20m/s.

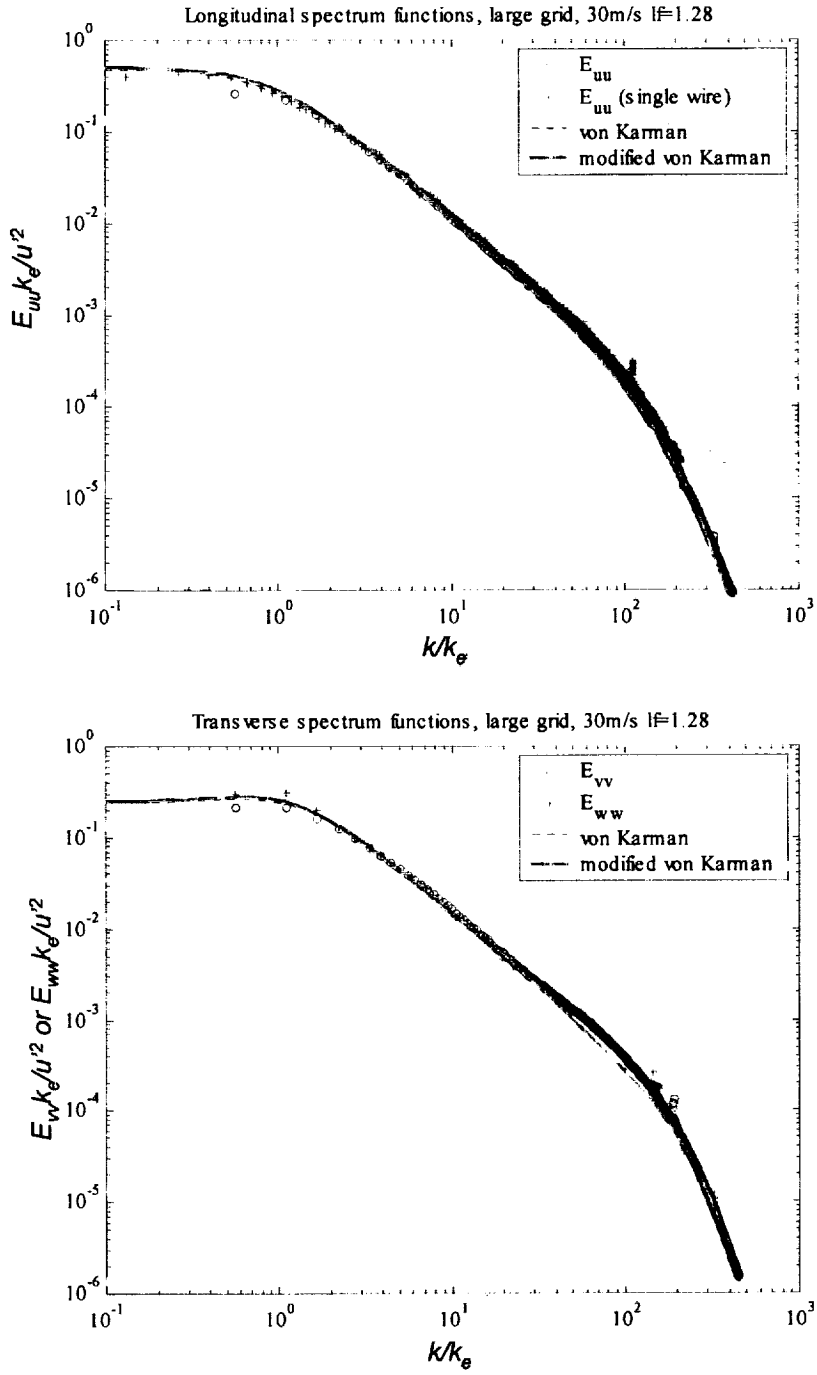

Figure 25. Wavenumber spectra measured with the large grid at 30m/s.

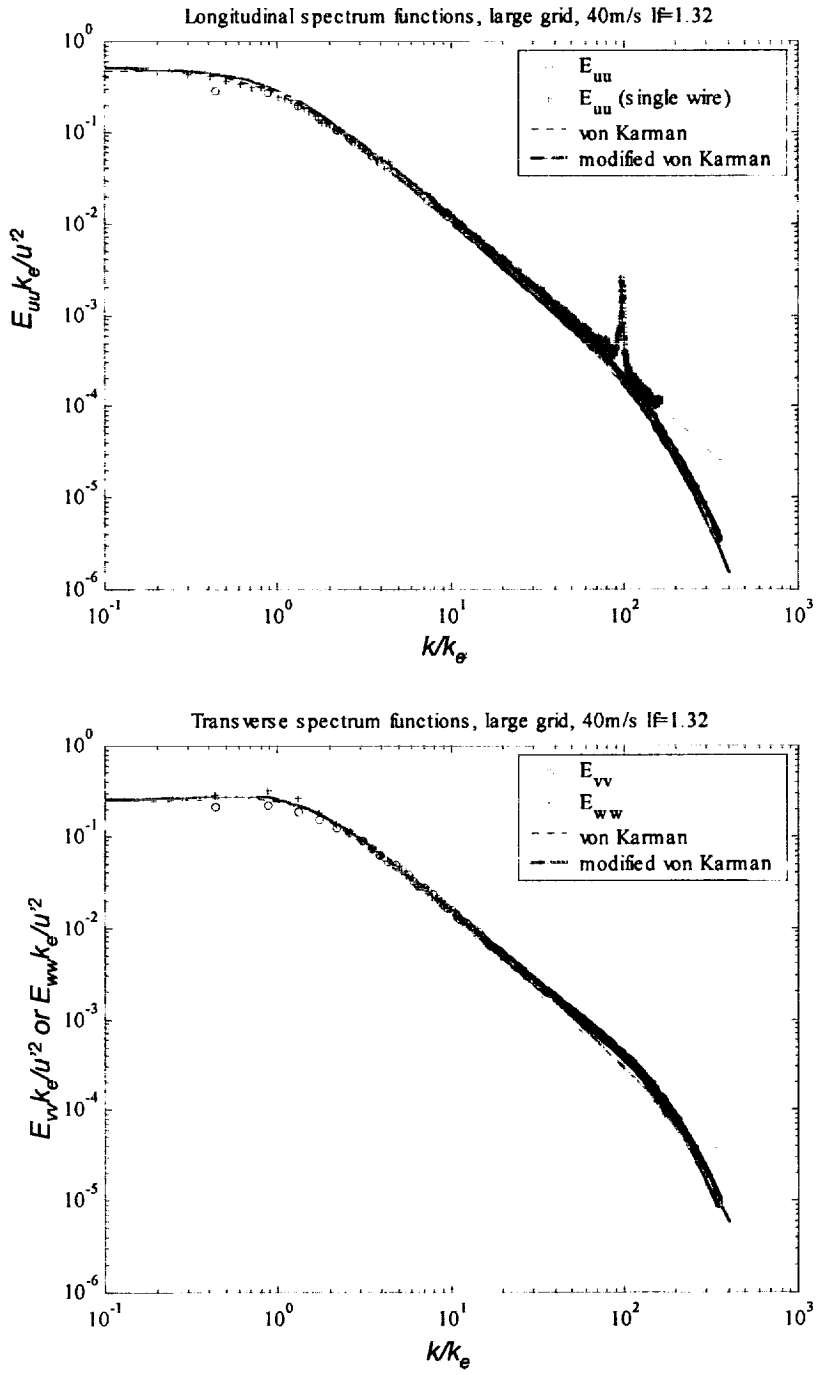

Figure 26. Wavenumber spectra measured with the large grid at 40m/s.

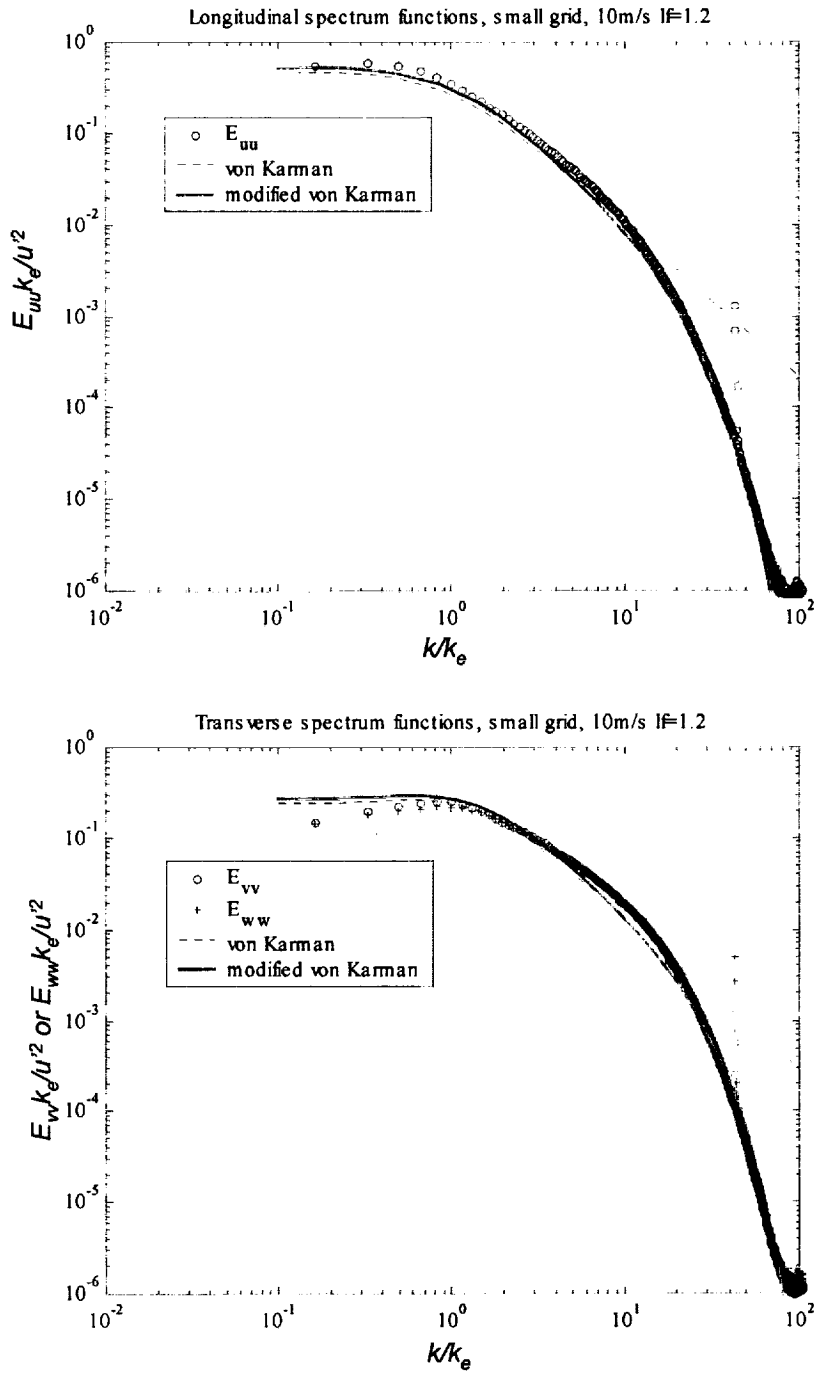

Figure 27. Wavenumber spectra measured with the small grid at 10m/s.

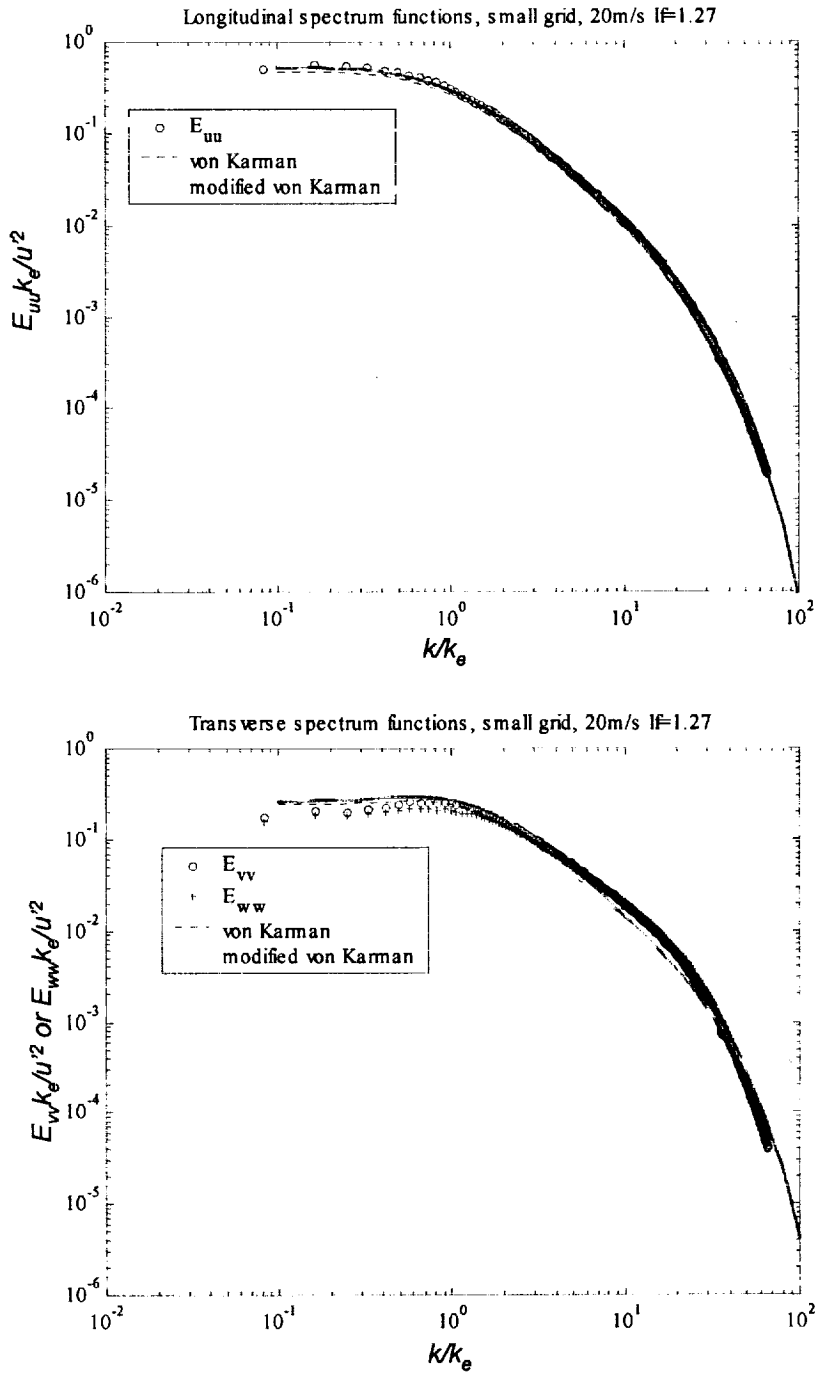

Figure 28. Wavenumber spectra measured with the small grid at 20m/s.

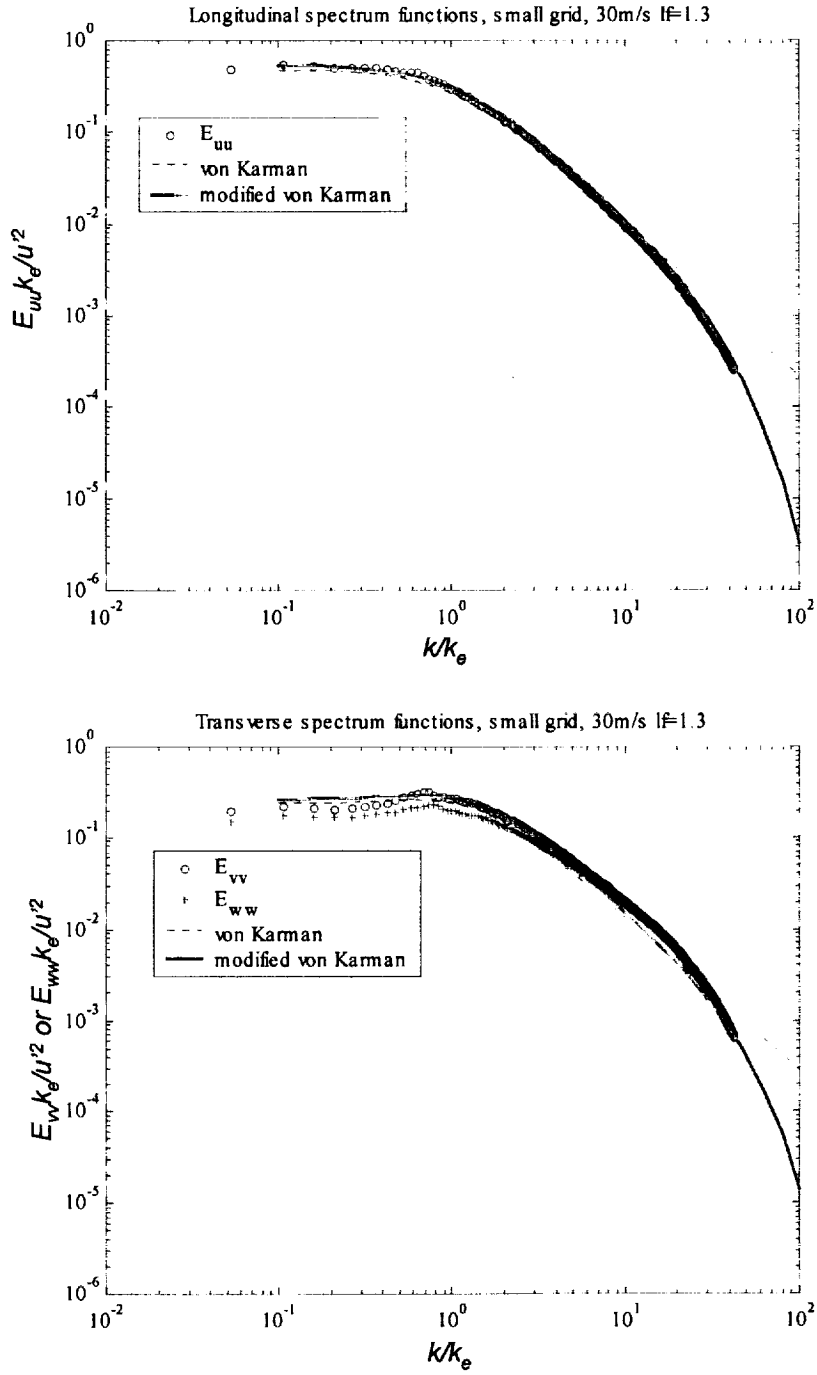

Figure 29. Wavenumber spectra measured with the small grid at 30m/s.

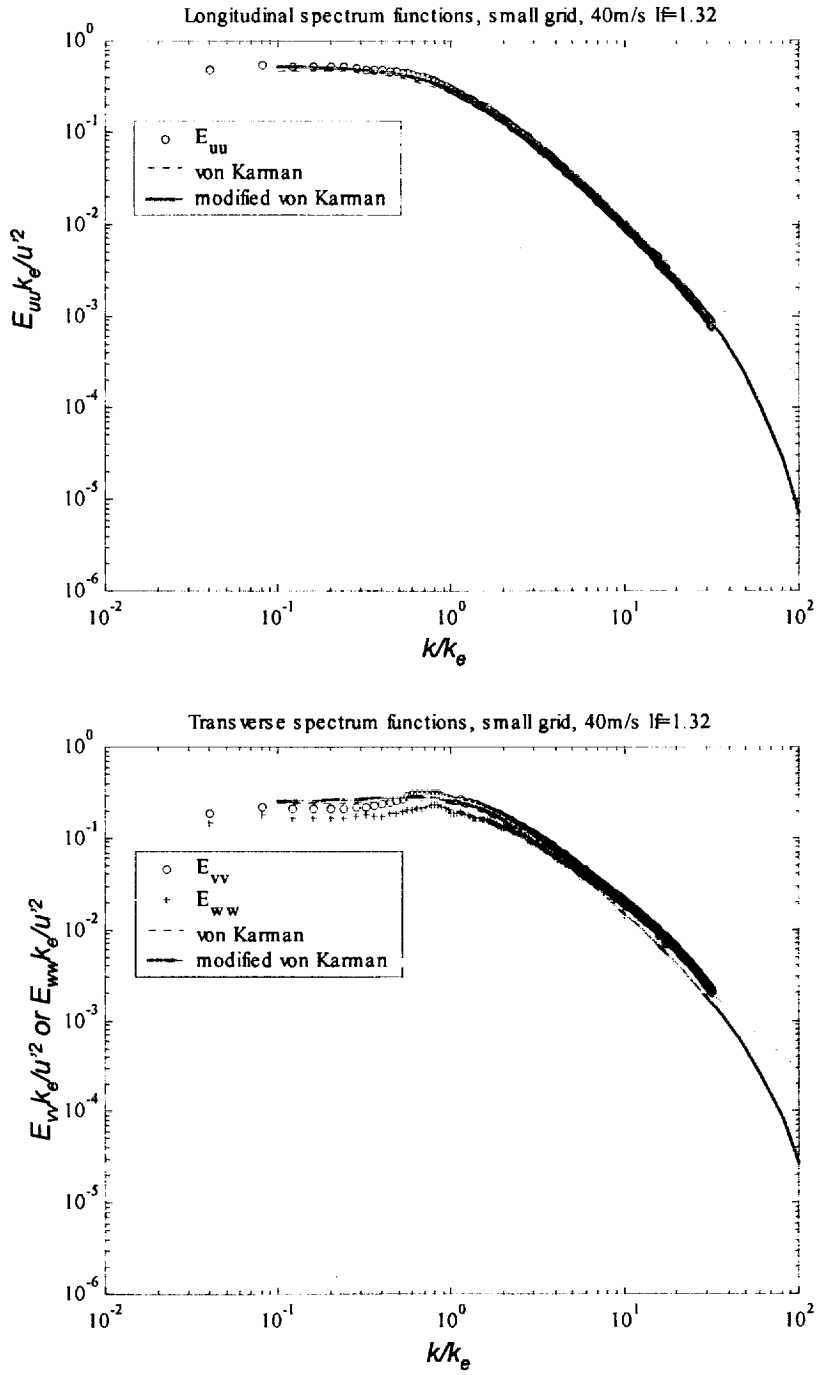

Figure 30. Wavenumber spectra measured with the small grid at 40m/s.

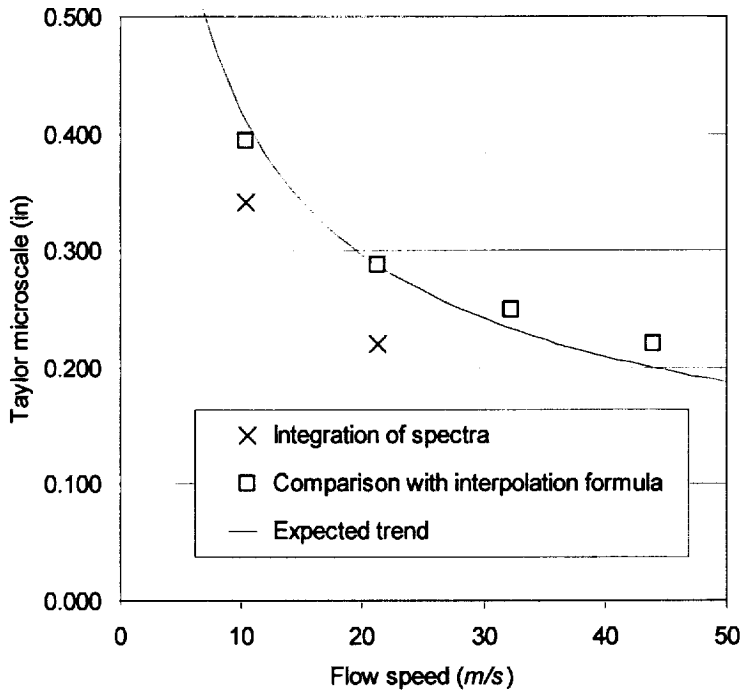

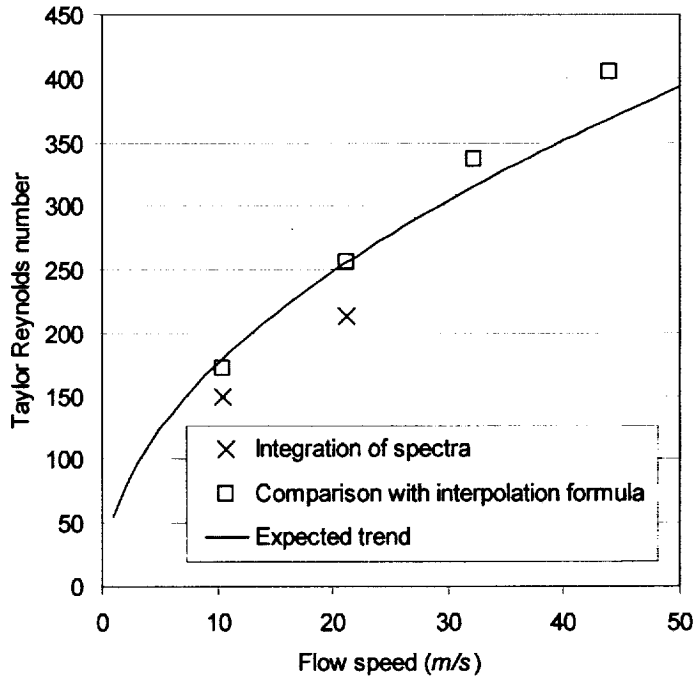

Figure 31. Taylor microscales and Reynolds numbers for the large grid.

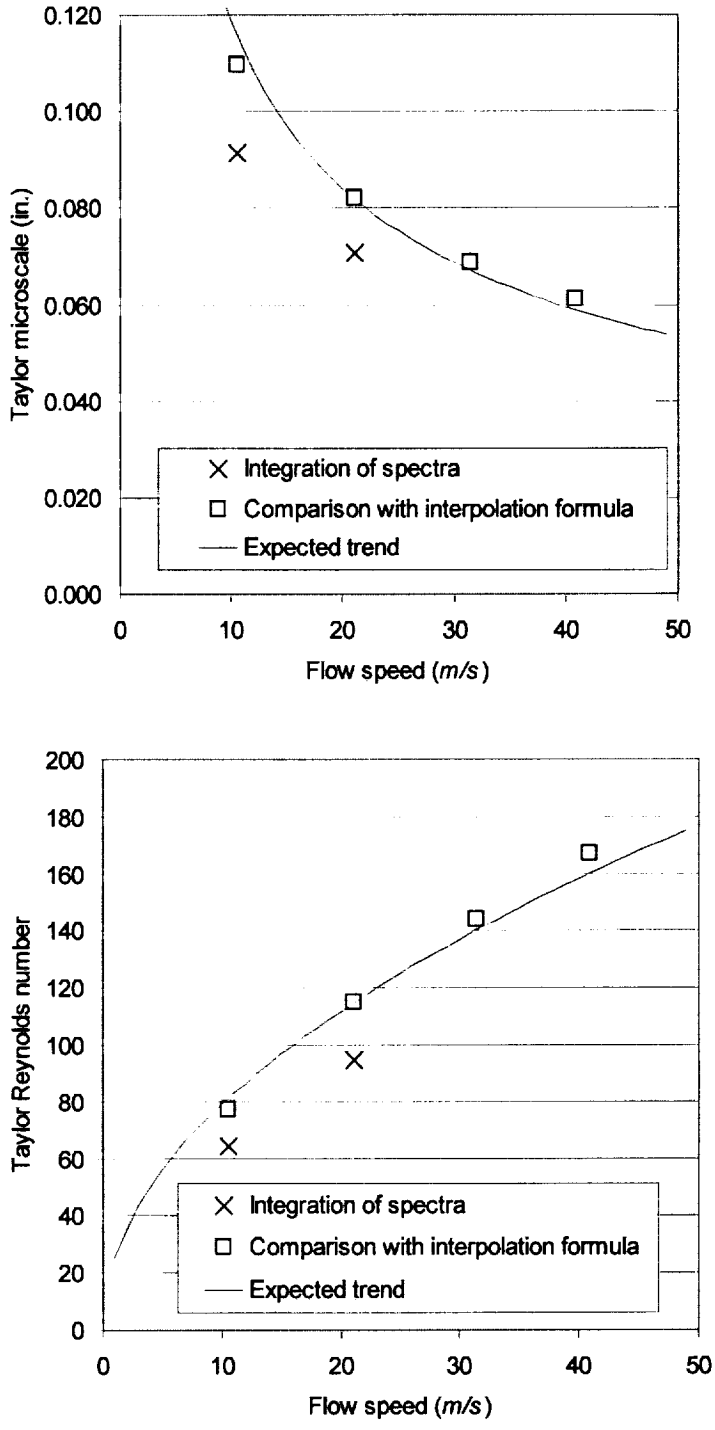

Figure 32. Taylor microscales and Reynolds numbers for the small grid.

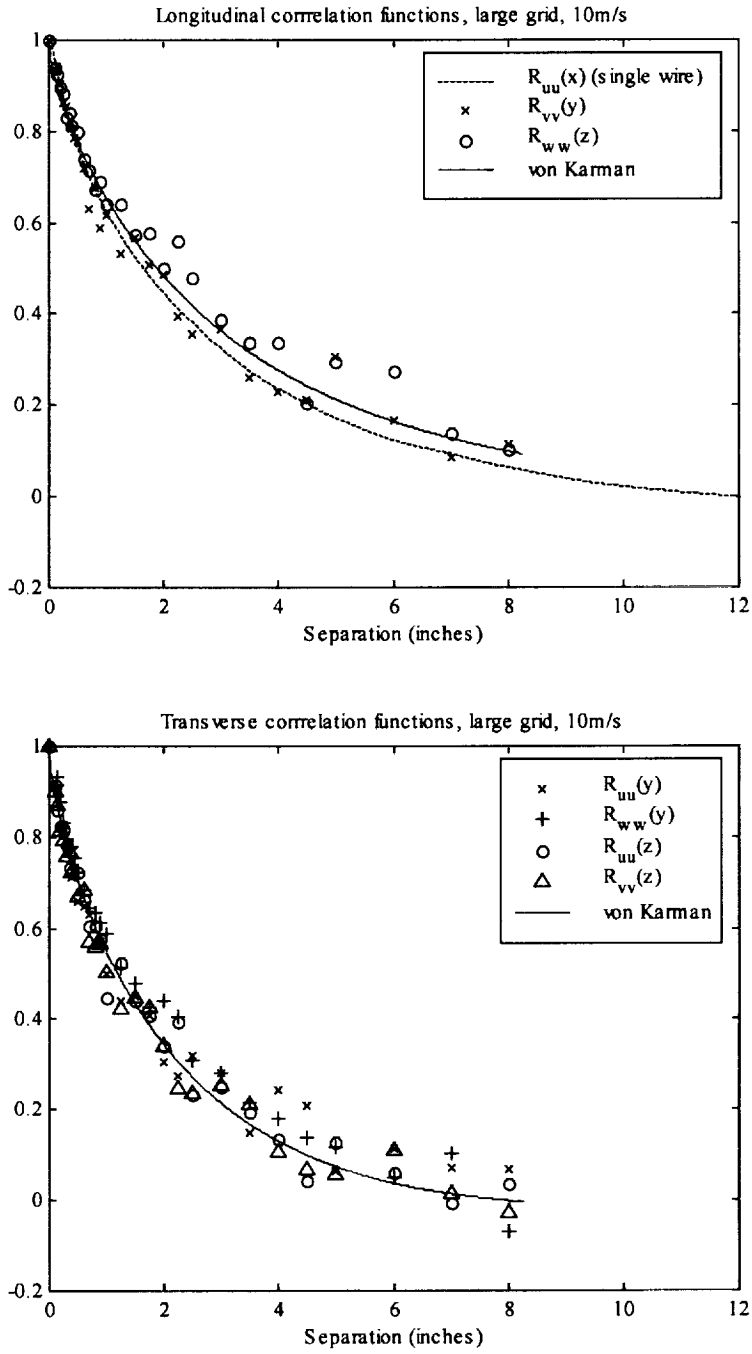

Figure 33. Correlation coefficient functions measured with the large grid at 10m/s, compared with von Karman forms generated using the integral scales in table 4.

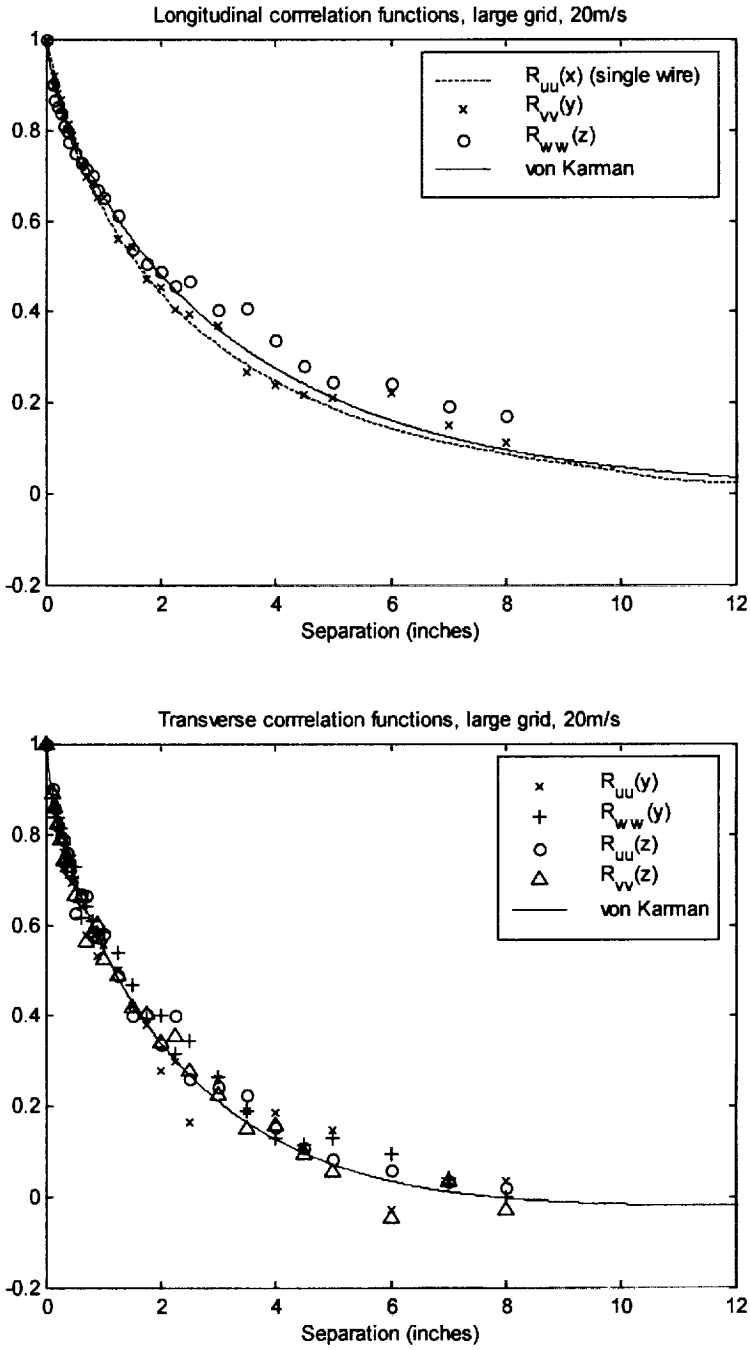

Figure 34. Correlation coefficient functions measured with the large grid at 20m/s, compared with von Karman forms generated using the integral scales in table 4.

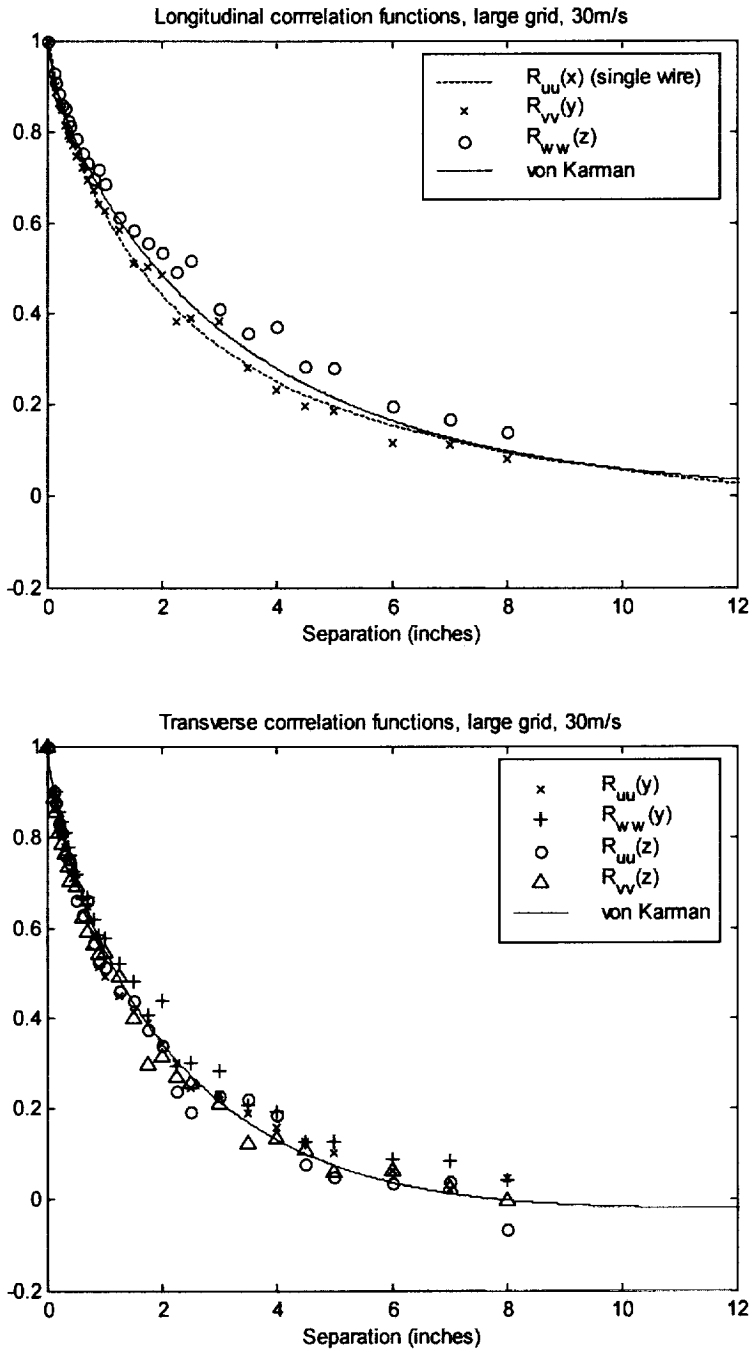

Figure 35. Correlation coefficient functions measured with the large grid at 30m/s, compared with von Karman forms generated using the integral scales in table 4.

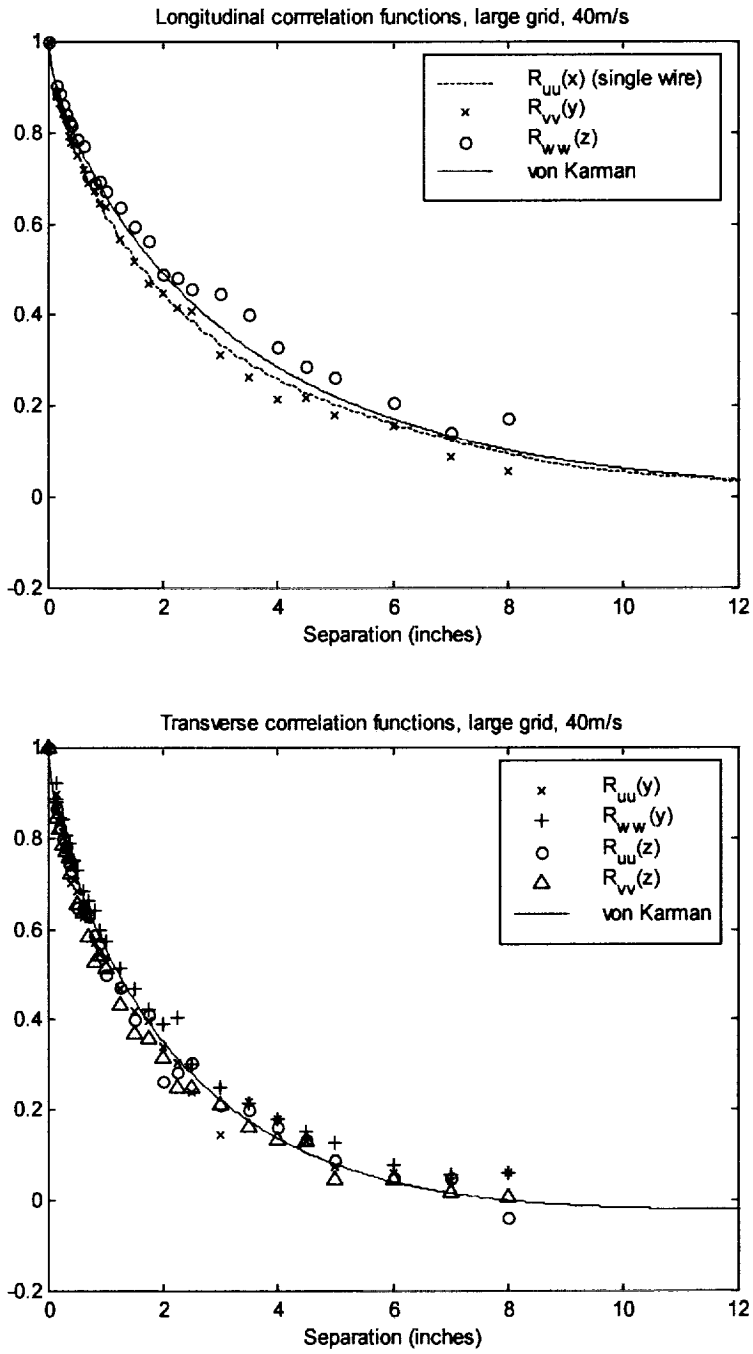

Figure 36. Correlation coefficient functions measured with the large grid at 40m/s, compared with von Karman forms generated using the integral scales in table 4.

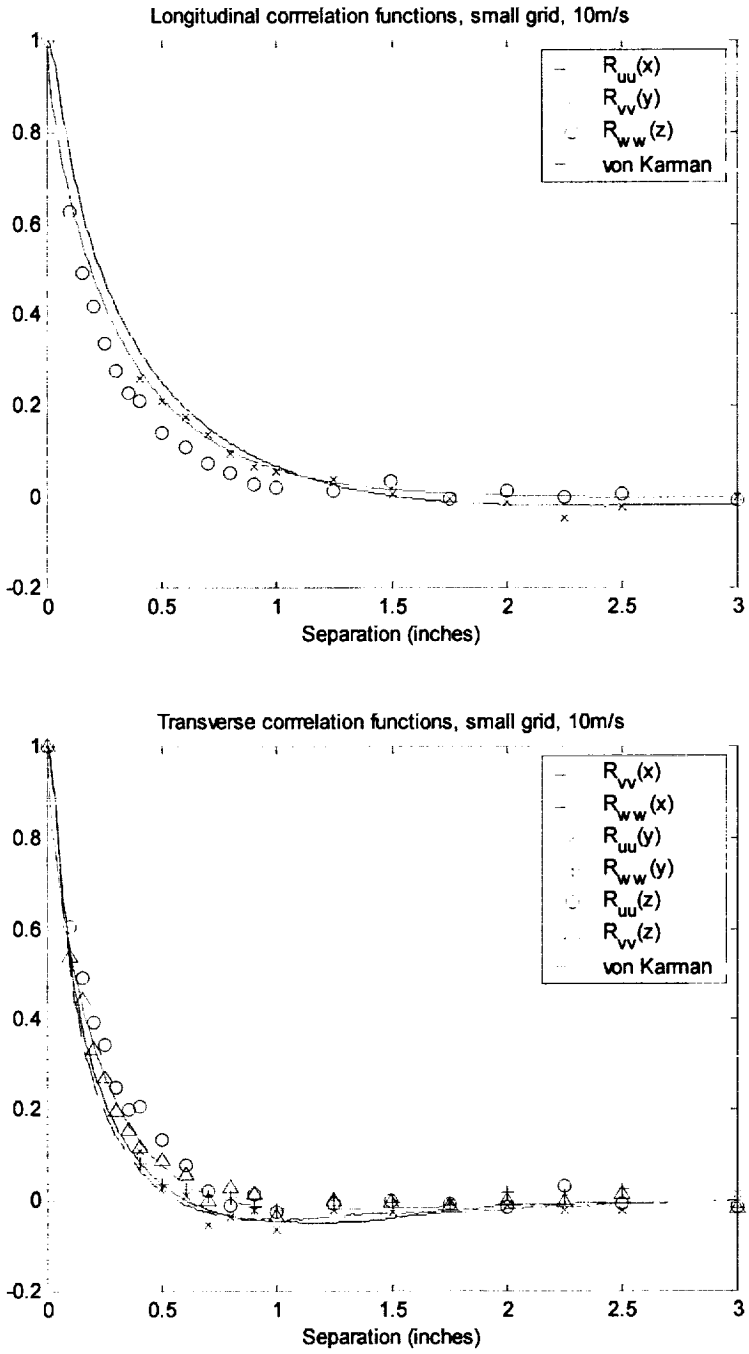

Figure 37. Correlation coefficient functions measured with the small grid at 10m/s, compared with von Karman forms generated using the integral scales in table 4.

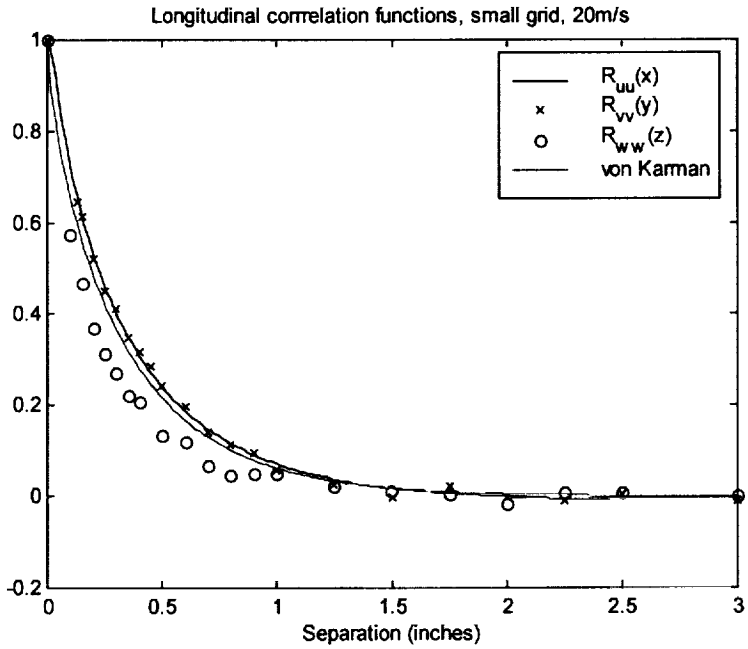

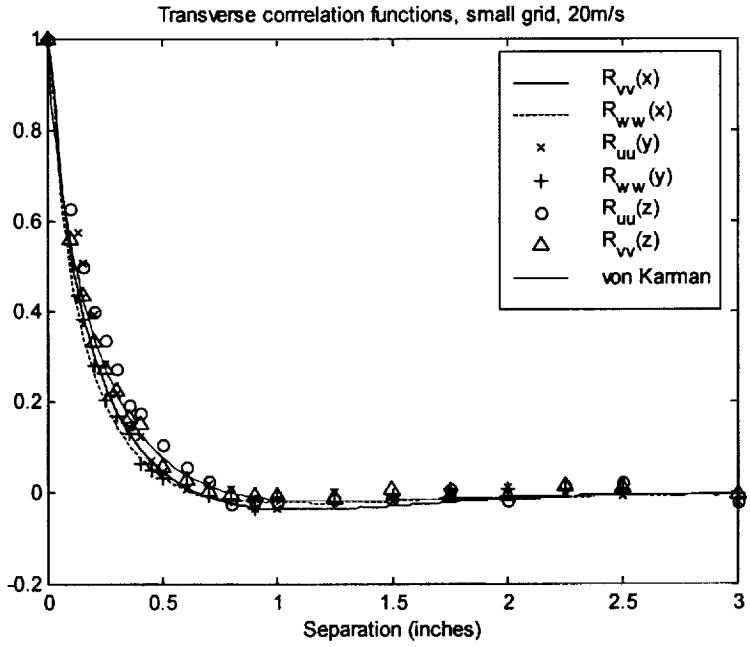

Figure 38. Correlation coefficient functions measured with the small grid at 20m/s, compared with von Karman forms generated using the integral scales in table 4.

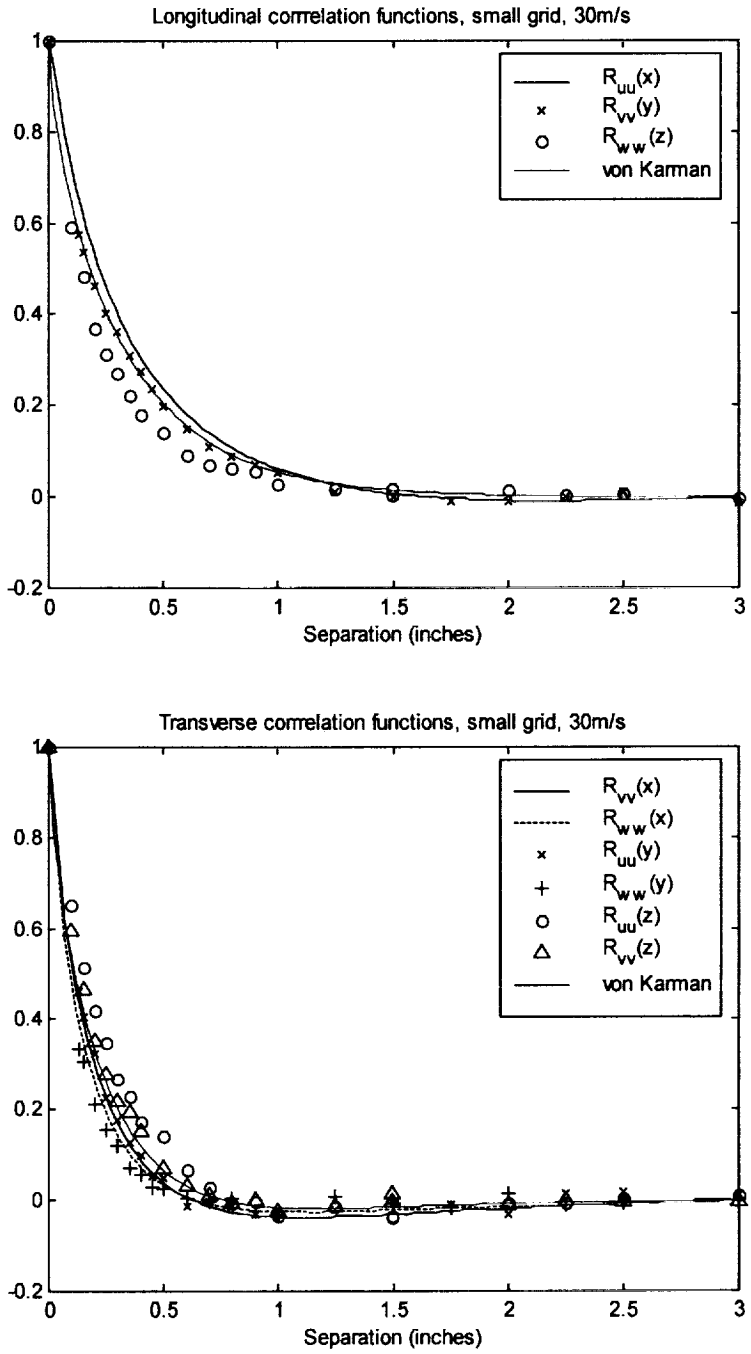

Figure 39. Correlation coefficient functions measured with the small grid at 30m/s, compared with von Karman forms generated using the integral scales in table 4.

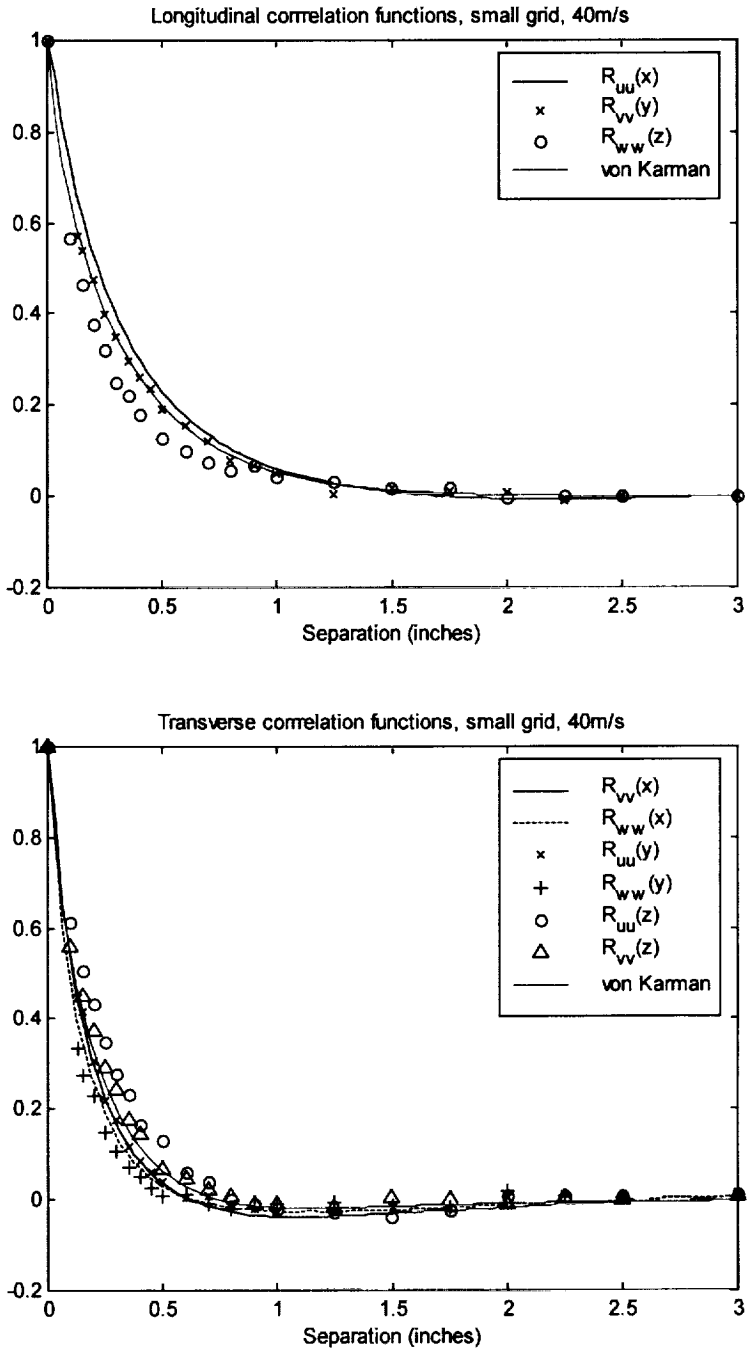

Figure 40. Correlation coefficient functions measured with the small grid at 40m/s, compared with von Karman forms generated using the integral scales in table 4.

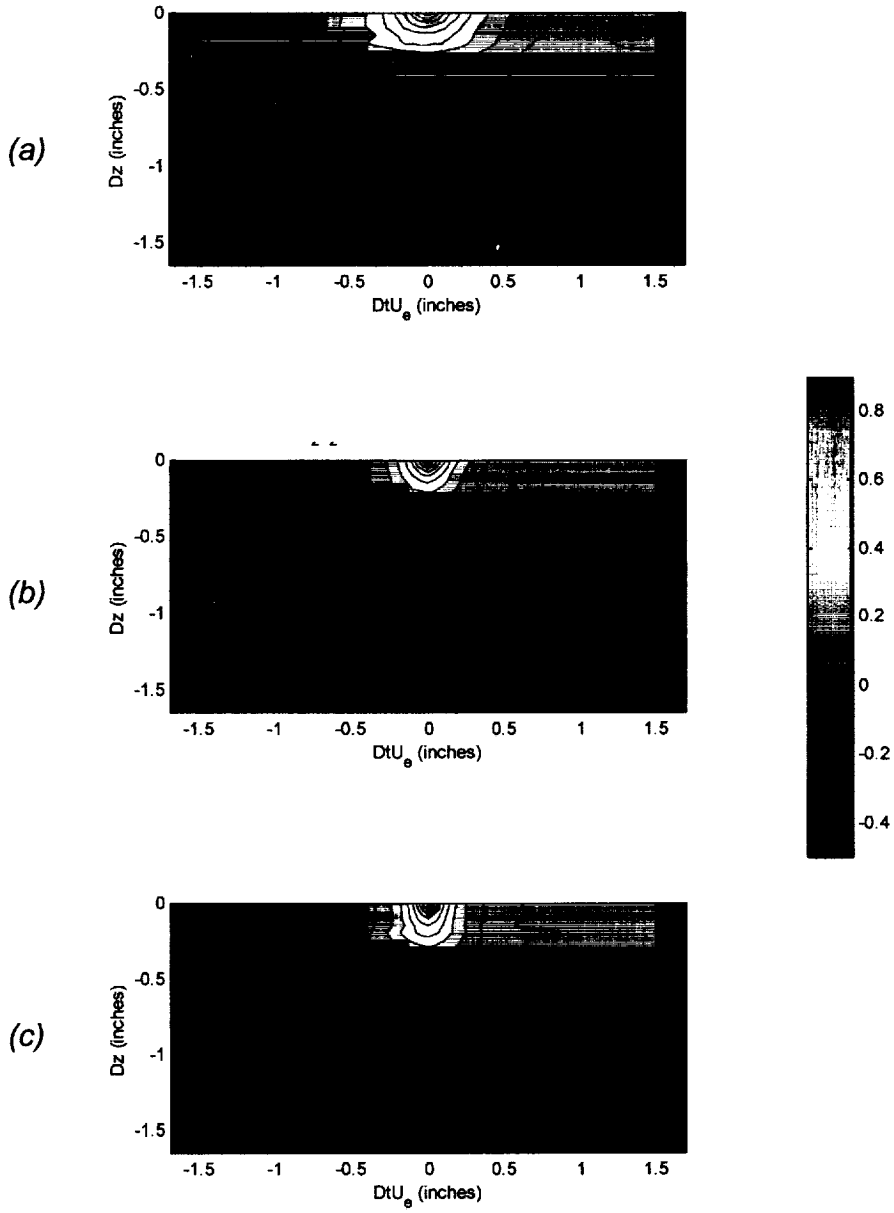

Figure 41. Space-time correlation maps measured with the small grid at 10m/s for spatial separations in the z direction. (a) R_{uu}, (b) R_{vv}, (c) R_{ww}.

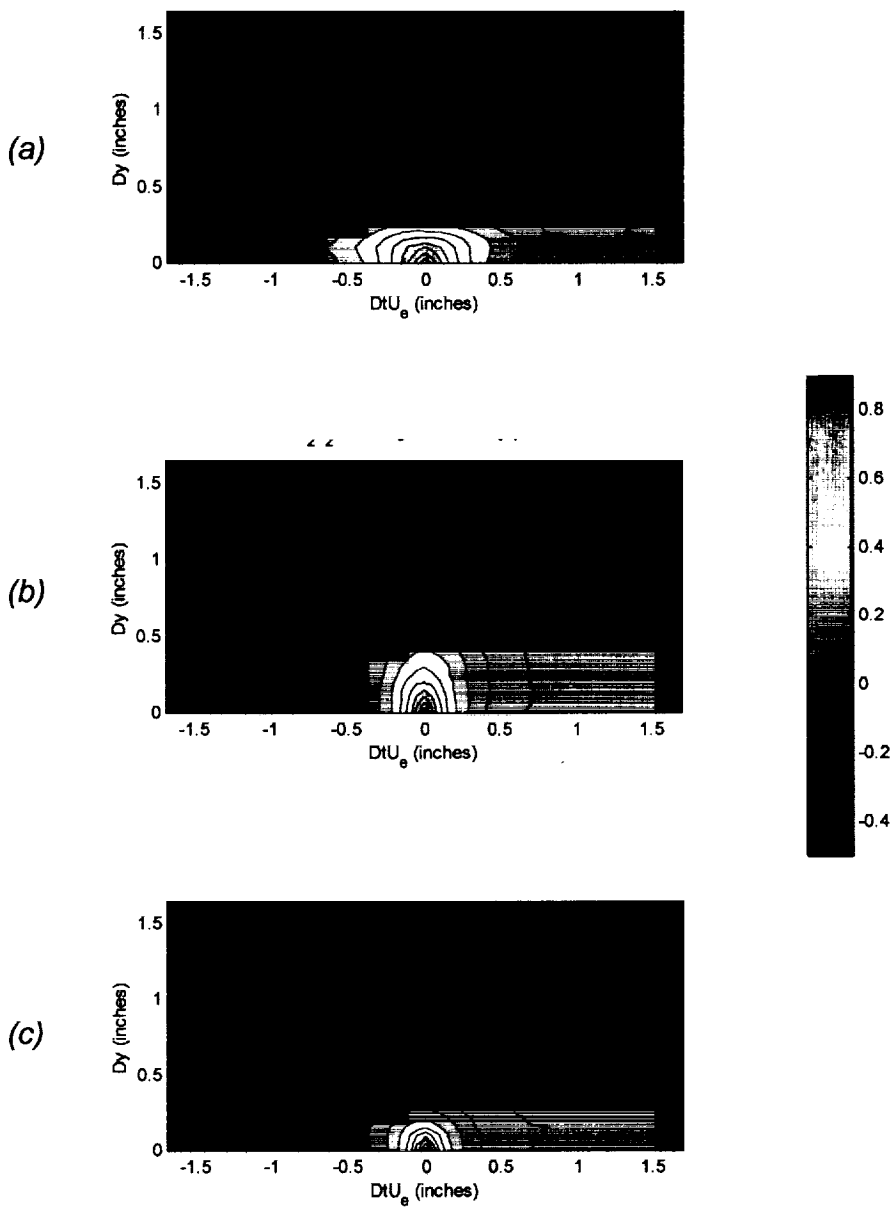

Figure 42. Space-time correlation maps measured with the small grid at 20m/s for spatial separations in the y direction. (a) R_{uu}, (b) R_{vv}, (c) R_{ww}.

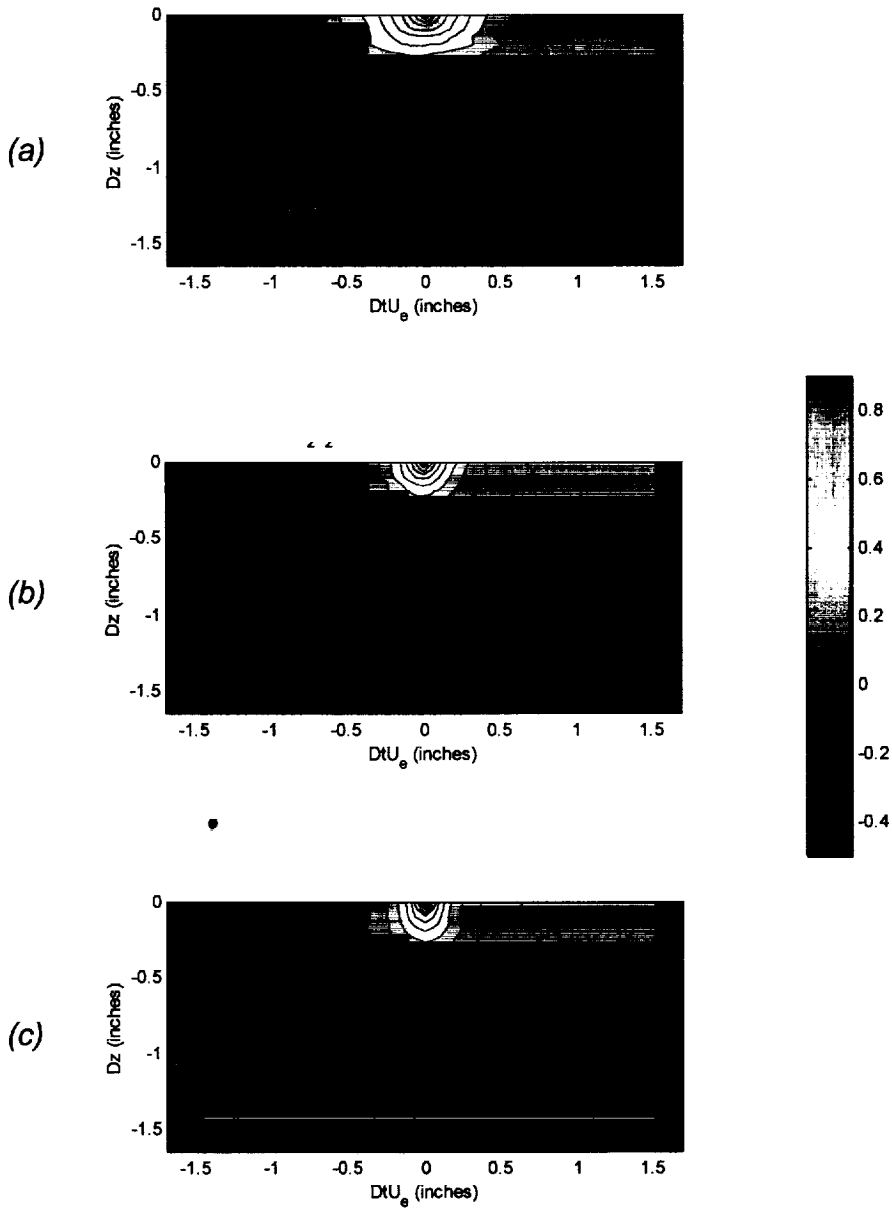

Figure 43. Space-time correlation maps measured with the small grid at 20m/s for spatial separations in the z direction. (a) R_{uu}, (b) R_{vv}, (c) R_{ww}.

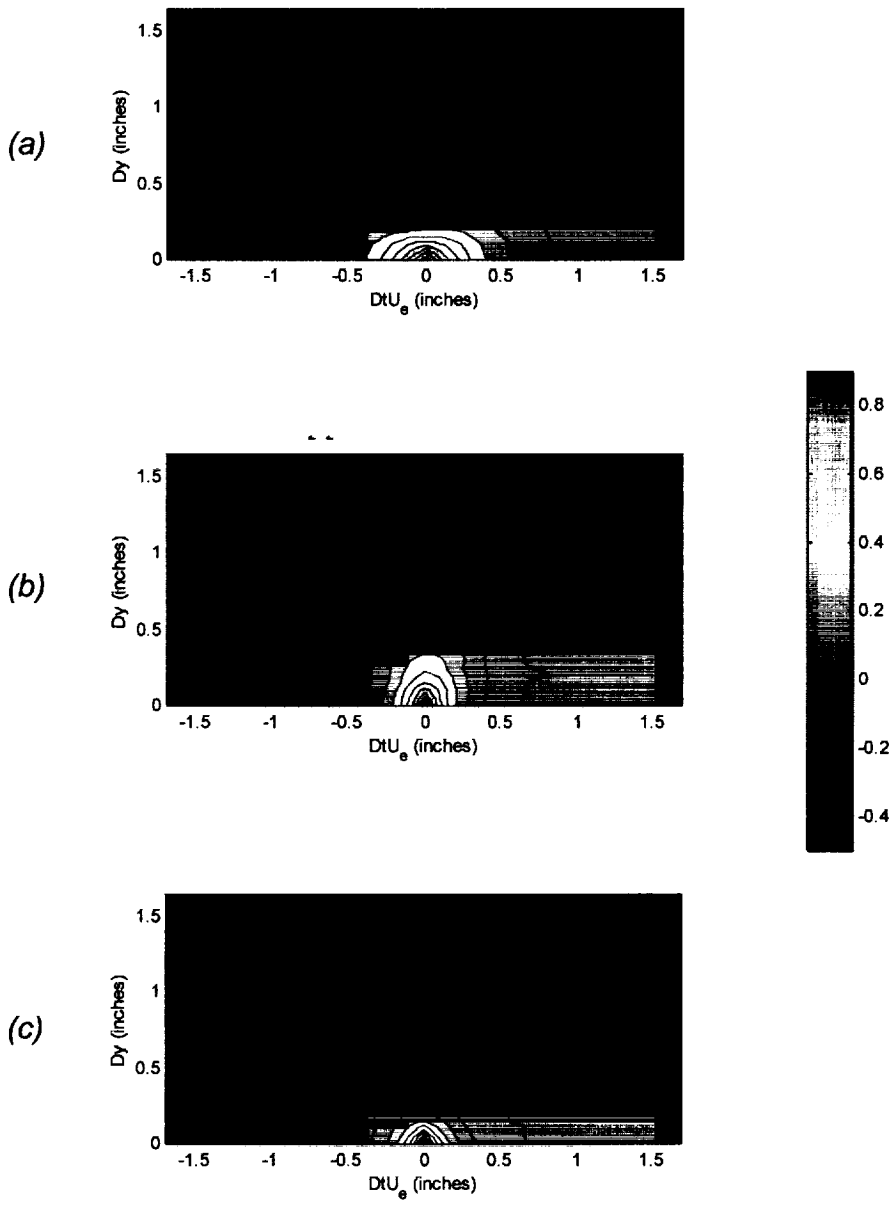

Figure 44. Space-time correlation maps measured with the small grid at 30m/s for spatial separations in the y direction. (a) R_{uu}, (b) R_{vv}, (c) R_{ww}.

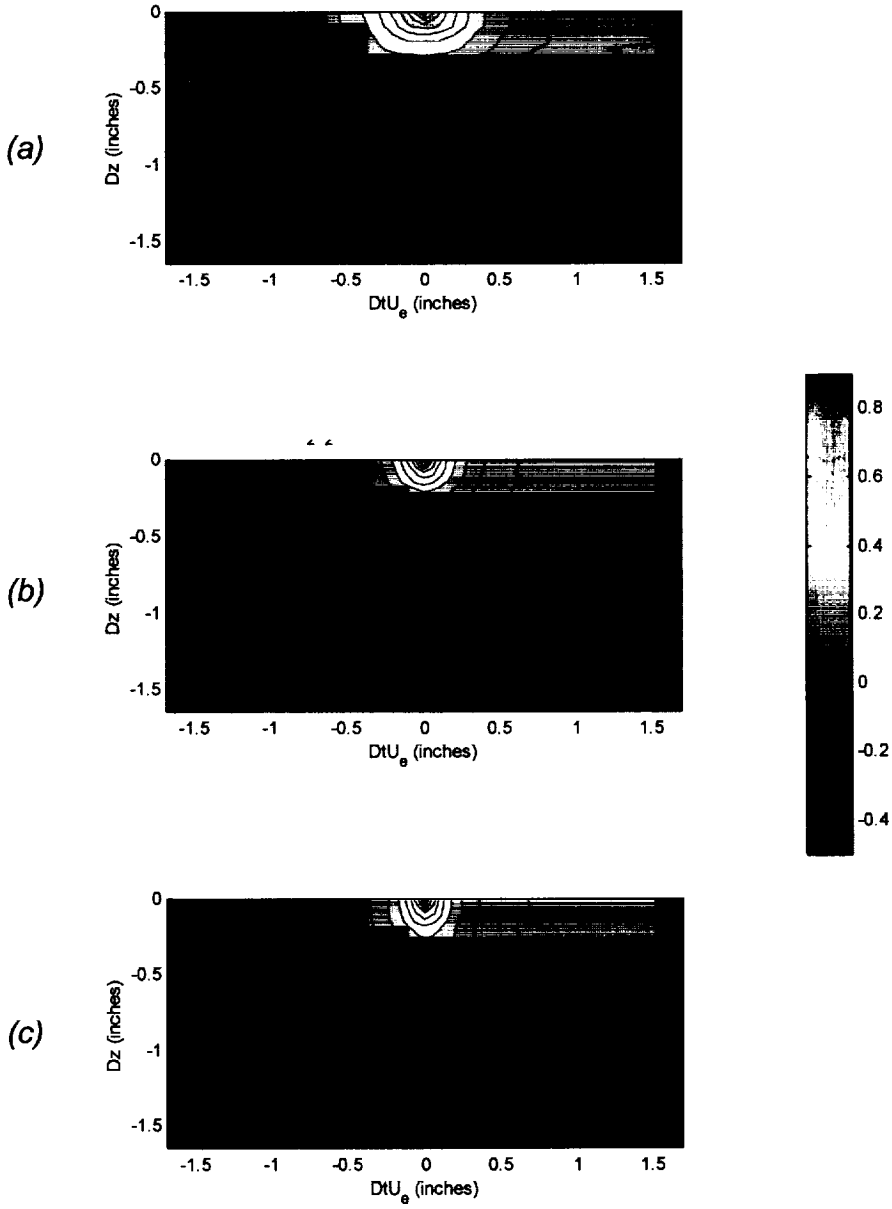

Figure 45. Space-time correlation maps measured with the small grid at 30m/s for spatial separations in the z direction. (a) R_{uu}, (b) R_{vv}, (c) R_{ww}.

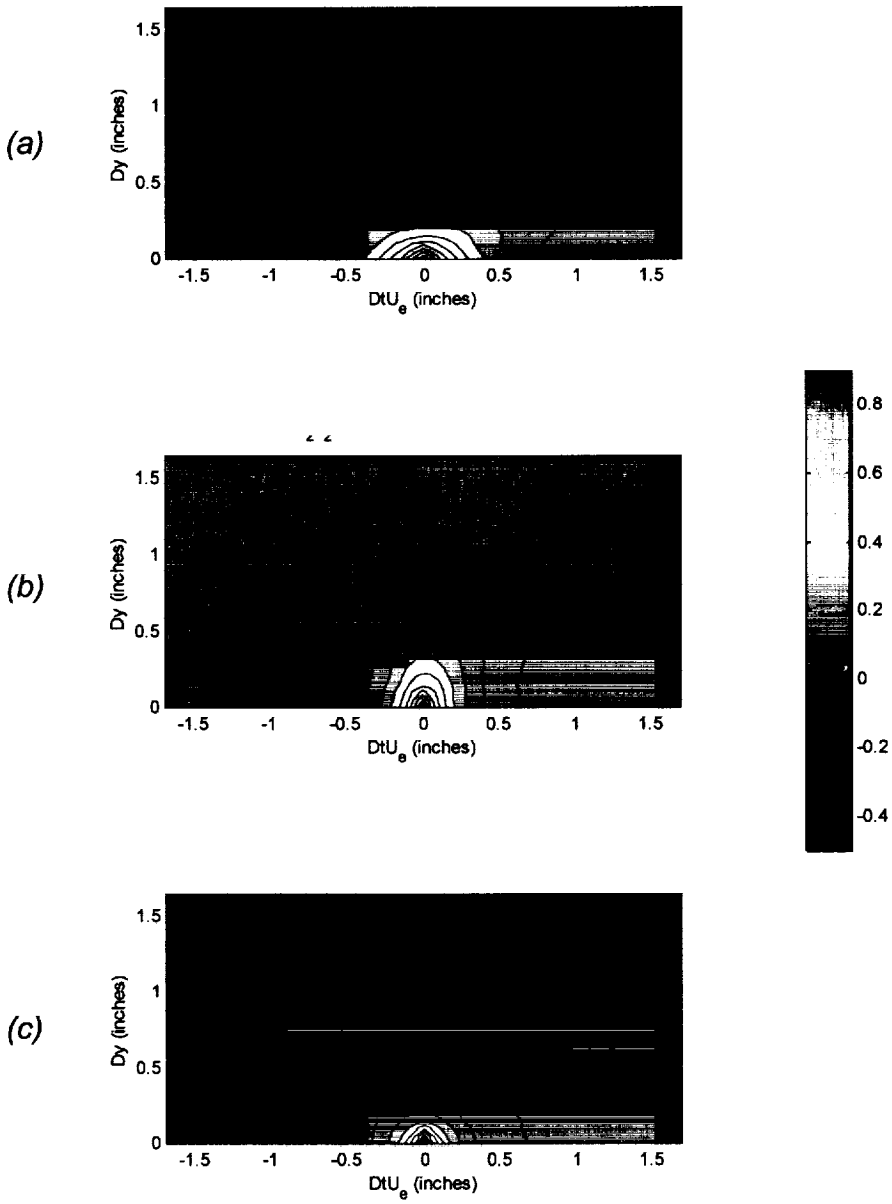

Figure 46. Space-time correlation maps measured with the small grid at 40m/s for spatial separations in the y direction. (a) R_{uu}, (b) R_{vv}, (c) R_{ww}.

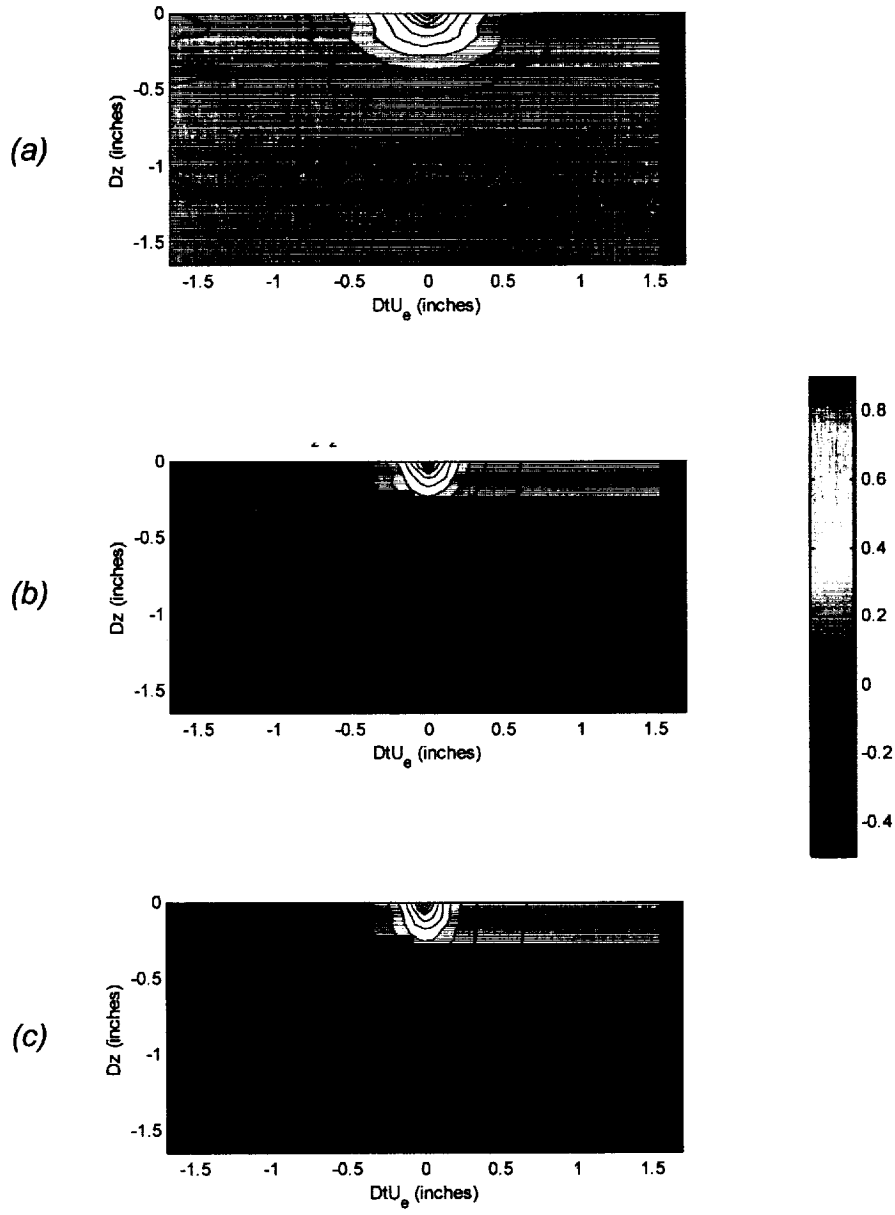

Figure 47. Space-time correlation maps measured with the small grid at 40m/s for spatial separations in the z direction. (a) R_{uu}, (b) R_{vv}, (c) R_{ww}.